2016

Development of Advanced, Clinically Feasible Neuroimaging Methodology with Diffusional Kurtosis Imaging

G. Russell Glenn
Medical University of South Carolina

Development of Advanced, Clinically Feasible Neuroimaging Methodology with Diffusional Kurtosis Imaging

by

G. Russell Glenn

A dissertation submitted to the faculty of the Medical University of South Carolina in partial fulfillment of the requirements for the degree of Doctor of Philosophy in the College of Graduate Studies.

Department of Neuroscience

2016

Approved by:

Chairman, Advisory Committee
Jens H. Jensen, PhD

Co-chairman, Advisory Committee
Leonardo Bonilha, MD, PhD

Joseph A. Helpern, PhD

Mark A. Eckert, PhD

Maria V. Spampinato, MD

TABLE OF CONTENTS

ACKNOWLEDGEMENTS

I sincerely thank my mentors, Jens Jensen, Leonardo Bonilha, and Joseph Helpern for their unparalleled guidance and support through the arduous and tortuous path of grad school. This project would not have been possible without their combined strengths and the immense foundational work that they have accomplished. I am also indebted for the guidance of Ali Tabesh, whose meticulous training in signal and image processing imparted a fundamental skill set required for this thesis. I thank my collaborators for their patience with me and their overarching enthusiasm for this work. In particular, I thank Li-Wei Kuo for his technical assistance and knowledge of advanced MRI techniques and Simon Keller for his openness to collaboration and his mentorship in neuroimaging research in epilepsy. I thank my committee members for their feedback and insight into this project and their interest in my development as a student. I am grateful for all of the members of the Helpern Lab who have been great friends and colleagues throughout this portion of my training, and the outstanding educational environment created by the College of Graduate Studies at MUSC, including the Department of Neuroscience and the Medical Scientist Training Program (MSTP). In particular, I would like to thank Perry Halushka and Amy Connolly in the MSTP for their support and guidance throughout the program. Finally, I thank my family, who have been my key source of strength and inspiration, and have encouraged me at every step along the way.

1

Introduction: Diffusional Kurtosis Imaging and the Application of Neuroimaging Biomarkers in Epilepsy

Diffusion MRI (dMRI) is a powerful, non-invasive tool for probing the structural organization of the human brain. Quantitative dMRI analyses provide unique capabilities for the characterization of tissue microstructure as well as imaging contrast that is not available to other modalities. White matter tractography relies on dMRI and is currently the only non-invasive technique for mapping structural connections in the human brain. In this chapter, we will describe diffusional kurtosis imaging, an effective and versatile dMRI technique, and discuss a clinical problem in temporal lobe epilepsy (TLE) which is insurmountable with current diagnostic approaches. Subsequent chapters will further develop the capabilities of DKI and demonstrate how it may be particularly well suited to overcome current barriers to care in the clinical management of TLE.

Introduction

Quantitative neuroimaging techniques are revolutionizing our understanding of the human brain by providing non-invasive tools for investigation of the structure, function, and physiology of *in vivo* neural tissue. These tools are rapidly generating new and exciting insights into normal and

pathological processes that affect the brain and hold unique promise for improving our ability to detect, diagnose, and predict the clinical course of disease.

One key problem that has yet to be solved is the development of diagnostic tools for temporal lobe epilepsy (TLE). TLE is a relatively common and disabling neurological condition with a largely variable clinical course. TLE is frequently refractory to pharmacotherapy and effective surgical treatment is often delayed (1,2). This may, in part, be due to our inability to accurately predict drug response and surgical outcomes in TLE with current diagnostic approaches. Thus, the development of neuroimaging biomarkers in TLE is a high-priority area in epilepsy research.

Diffusion MRI (dMRI) is a quantitative neuroimaging tool that is sensitive to the random, molecular motion, or diffusion, of water on a microscopic scale (3,4). The diffusion signal is shaped by the cytoarchitectural organization of biological tissue and is affected by disease processes including stroke, cancer, and numerous neurological and psychiatric disorders (5). Because TLE is a focal epilepsy disorder associated with both circumscribed and diffuse structural brain abnormalities, we hypothesize that dMRI will be sensitive to abnormalities in TLE which are not apparent by other modalities; in particular, by developing advanced dMRI tools, we will improve the ability to characterize clinicopathological features of TLE.

Temporal Lobe Epilepsy

Temporal lobe epilepsy (TLE) is the most common form of medically refractory focal epilepsy. Despite recent advances in anti-epileptic drug (AED) therapy (6-8), many patients with TLE cannot be treated with AEDs and are consequently at risk for developing irreversible cognitive

deficits (9,10), psychosocial disability (11-13), and premature death (14,15) from damage caused by recurrent seizures. Surgery can cure TLE by removing epileptogenic foci and has been shown to improve treatment and quality of life over continued AED therapy with comparable or improved risks (16). However, surgical success is not universally achieved, as approximately 50% of patients with TLE continue to experience seizures after a technically successful operation (17-21). Patients who become seizure free are clinically indistinguishable from those who continue to experience seizures after surgery (22). As a result, surgery is often viewed as having unpredictable outcomes and patients with difficult to treat TLE are not referred to surgery until well after the recommended guidelines (1,2). Thus, our inability to accurately predict surgical outcomes prevents optimal medical care as delayed surgical referral reduces the life span and quality of life for individual patients with difficult to treat TLE and increases the burden of epilepsy on the overall population.

The mechanisms underlying surgical responsiveness are not well understood. One hypothesis suggests that brain damage leads to biochemical and structural changes that result in the reorganization of neural tissue leading to abnormal neuronal synchronization and eventually, spontaneous epileptiform discharges (23-27). Thus, seizure freedom is achieved when patients exhibit epileptogenic changes that are restricted to the structures removed during surgery, whereas patients who continue to experience seizures have broader epileptogenic abnormalities (2,23,27,28). A diagnostic tool that could detect these abnormalities and accurately predict surgical outcomes would have a tremendous impact in the treatment of TLE by fostering early surgical referral for patients with optimal chances of success, permitting

timely access to cure and preventing the negative effects of recurrent seizures for most patients with refractory TLE.

Diffusional Kurtosis Imaging

Diffusional kurtosis imaging (DKI) is a clinically feasible diffusion dMRI technique which measures the diffusion and kurtosis tensors to characterize the three-dimensional diffusion dynamics occurring *in vivo*. To accomplish this, DKI assumes that the diffusion-weighted signal can be well described by its fourth-order cumulant expansion, provided the b-value (the strength of diffusion weighting) is not too large. The natural logarithm of the diffusion signal is thus given by (29,30):

$$\ln S(b,\boldsymbol{n}) = \ln S_0 - b\sum_{ij} n_i n_j D_{ij} + \frac{b^2\bar{D}^2}{6}\sum_{ijkl} n_i n_j n_k n_l W_{ijkl}, \qquad [1]$$

where b is the b-value, $\boldsymbol{n}$ is a normalized direction vector, S_0 is the signal with no diffusion weighting, $\boldsymbol{D}$ is the diffusion tensor, $\bar{D}$ is the mean diffusivity, $\boldsymbol{W}$ is the kurtosis tensor, the subscripts label Cartesian components, and sums on the indices are carried out from 1 to 3.

The second order diffusion tensor and fourth order kurtosis tensor are defined by:

$$D_{ij} \equiv \frac{1}{2t}\langle s_i s_j \rangle, \qquad [2]$$

and

$$W_{ijkl} \equiv \frac{9}{\langle \boldsymbol{s}\cdot\boldsymbol{s}\rangle^2}\left(\langle s_i s_j s_k s_l\rangle - \langle s_i s_j\rangle\langle s_k s_l\rangle - \langle s_i s_k\rangle\langle s_j s_l\rangle - \langle s_i s_l\rangle\langle s_j s_k\rangle\right), \quad [3]$$

respectively, for a diffusion displacement $\boldsymbol{s}$ over time t, with the angle brackets indicating the expected value of a random variable, which in this case is the average displacement over the ensemble of diffusing spins. From Eqs. [2] and [3] it is clear that the diffusion and kurtosis tensors are invariant to permutations of the vector, $\boldsymbol{s}$, and are thus fully symmetric.

A motivation for estimating the diffusion and kurtosis tensors is to describe the directional dependence of diffusion dynamics in anisotropic biological tissues, which can then yield unique information on microstructural tissue organization. Directional diffusivity and diffusional kurtosis estimates for an arbitrary direction are thus given by:

$$D(\boldsymbol{n}) = \sum_{ij} n_i n_j D_{ij}, \quad [4]$$

and

$$K(\boldsymbol{n}) = \frac{\bar{D}^2}{D(\boldsymbol{n})^2}\sum_{ijkl} n_i n_j n_k n_l W_{ijkl}. \quad [5]$$

Mean diffusivity and diffusional kurtosis are calculated as the mean directional diffusivity and kurtosis over all directions:

$$\bar{D} = \frac{1}{4\pi} \int d\boldsymbol{n}\, D(\boldsymbol{n}), \qquad [6]$$

and

$$\bar{K} = \frac{1}{4\pi} \int d\boldsymbol{n}\, K(\boldsymbol{n}). \qquad [7]$$

Note that the calculation of $\bar{K}$ requires knowledge of both the diffusion and kurtosis tensors. However, it is possible to calculate the mean of the kurtosis tensor by letting:

$$W(\boldsymbol{n}) = \sum_{ijkl} n_i n_j n_k n_l W_{ijkl}. \qquad [8]$$

Then,

$$\bar{W} = \frac{1}{4\pi} \int d\boldsymbol{n}\, W(\boldsymbol{n}). \qquad [9]$$

Both $\bar{D}$ and $\bar{W}$ can be computed readily from $\boldsymbol{D}$ and $\boldsymbol{W}$ by:

$$\bar{D} = Tr(\boldsymbol{D})/3 = (\lambda_1 + \lambda_2 + \lambda_3)/3, \qquad [10]$$

where $Tr(\cdots)$ is the trace operator and λ_1, λ_2, and λ_3 are the three eigenvalues of the diffusion tensor, and (31):

$$\bar{W} = (W_{1111} + W_{2222} + W_{3333} + 2W_{1122} + 2W_{1133} + 2W_{2233})/5. \quad [11]$$

It should be noted that $\bar{W}$ approximates $\bar{K}$, but they are only strictly equal in the isotropic case as:

$$\bar{K} = \frac{1}{4\pi} \int d\boldsymbol{n} \frac{\bar{D}^2}{D(\boldsymbol{n})^2} W(\boldsymbol{n}). \quad [12]$$

The Kurtosis Diffusion Orientation Distribution Function

A novel feature of DKI in comparison to conventional diffusion tensor imaging (DTI) is its ability to directly resolve multiple fiber bundle orientations in voxels with a non-uniform fiber bundle distribution. To accomplish this, DKI evaluates the diffusion orientation distribution function (dODF) (32,33), which is a commonly used function to extract directional information from dMRI data (32-39).

The dODF evaluates the radial projection of the diffusion displacement probability density function (dPDF) along a given direction in space to quantify the relative degree of diffusion mobility along that direction, without making any explicit assumptions about tissue microstructure. The equation for the dODF is given by:

$$\psi_\alpha(\boldsymbol{n}) = \frac{1}{Z} \int_0^\infty \boldsymbol{ds}\, \boldsymbol{s}^\alpha P(\boldsymbol{s}, t), \quad [13]$$

where $P(\boldsymbol{s}, t)$is the dPDF, the radial weighting power, α, increases the sensitivity to relatively long diffusion displacements and Z is the normalization constant.

By assuming the dPDF is fully characterized by the diffusion tensor, the Gaussian dODF is given by:

$$\psi_{\alpha,G}(\boldsymbol{n}) = \left(\frac{1}{\boldsymbol{n}^T\boldsymbol{U}\boldsymbol{n}}\right)^{(\alpha+1)/2}. \qquad [14]$$

where $\boldsymbol{U} = \bar{D}\boldsymbol{D}^{-1}$ for diffusion tensor $\boldsymbol{D}$ and mean diffusivity $\bar{D}$.

By including the leading non-Gaussian corrections provided by the kurtosis tensor, the kurtosis dODF may be evaluated explicitly as (32):

$$\psi_{\alpha,K}(\boldsymbol{n}) = \psi_{\alpha,G}(\boldsymbol{n})\left\{1 + \frac{1}{24}\sum_{i,j,k,l}\left[3U_{ij}W_{ijkl}U_{kl} - 6(\alpha+1)U_{ij}W_{ijkl}V_{kl} + (\alpha+1)(\alpha+3)V_{ij}W_{ijkl}V_{kl}\right]\right\}, \qquad [[15]$$

where $\boldsymbol{W}$ is the kurtosis tensor,

$$V_{ij} = \frac{(\boldsymbol{U}\boldsymbol{n})_i(\boldsymbol{U}\boldsymbol{n})_j}{\boldsymbol{n}^T\boldsymbol{U}\boldsymbol{n}}, \qquad [16]$$

and the sums on the indices (i, j, k, l) are carried out from 1 to 3.

Since the diffusion and kurtosis tensors are fully symmetric, the dODF is symmetric with respect to the origin. Thus, local maxima pair in the dODF indicate orientations with overall less restricted diffusion and are interpreted as distinct fiber bundle orientations. By accounting for the leading effects of non-Gaussian diffusion, the kurtosis dODF can resolve angular differences in the dPDF which are not apparent from analysis of the diffusion tensor alone. The DKI-derived

fiber bundle orientations may then be utilized to reconstruct distinct white matter fiber bundles via tractography. Examples of Gaussian and kurtosis dODFs for a single voxel, as well as distinct fiber bundles identified with DKI-based tractography, are illustrated in Figure 1.

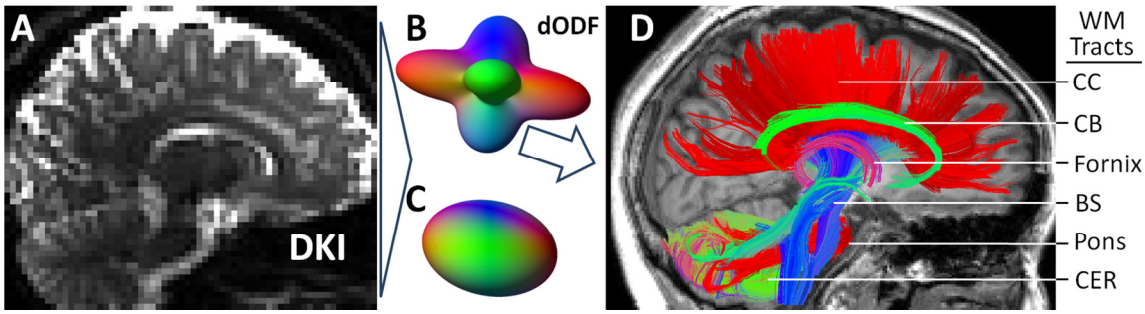

Figure 1. DKI-based tractography uses the kurtosis dODF. (A) Sagittal slice from a T2-weighted EPI image used by DKI to help estimate the diffusion and kurtosis tensors in each voxel. (B-C) Example kurtosis and Gaussian dODFs, respectively, from a single voxel, can be evaluated to estimate the orientation of preferential diffusion mobility in vivo. (B) The diffusion and kurtosis tensors are combined to calculate the kurtosis dODF, which is capable of resolving the orientation of multiple crossing fibers. (C) The Gaussian dODF can only directly resolve one fiber bundle orientation in each voxel, which averages effects from all fiber bundle orientations present. (D) A midline, sagittal view of fiber tracts estimated with whole-brain, DKI-based tractography reveals specific structures such as the corpus callosum (CC), cingulum bundle (CB), fornix, brain stem (BS), transverse pontine fiber (Pons), and cerebellar white matter (CER). The equations used to calculate (B) and (C) are given in Eqs. [14] and [[15].

Summary

The overarching aim of this work is to develop advanced, clinically feasible neuroimaging methodology for the application of neuroimaging biomarkers in TLE. We focus on DKI as DKI is a powerful and versatile dMRI technique with unique advantages compared to other dMRI methods. These advantages are further developed in this work and demonstrated to be advantageous for neuroimaging in TLE.

We begin our investigation, in Chapter 2, by studying anisotropic features of the diffusion signal, including distinct and complementary information provided by the kurtosis tensor. This can be advantageous as conventional DTI analyses of anisotropy may contain substantial errors in complex neural tissue. In Chapter 3, we deconstruct the kurtosis tensor using mathematical models to study how it may be affected by specific features of the underlying cytoarchitectonics. Improved understanding of the kurtosis tensor can lead to the development of more specific biomarkers for detecting pathology. In Chapter 4, we study properties of the kurtosis dODF, which can be used to detect crossing white matter fibers for tractography, and in Chapter 5, we contrast orientations estimated with the kurtosis dODF to other dMRI techniques to evaluate the potential of DKI for tractography. DKI is an attractive method for tractography, because it combines sensitive quantitative analyses from the diffusion and kurtosis tensor with the ability to directly resolve crossing white matter fiber bundles with the kurtosis dODF. In Chapter 6, we test the potential for combining quantitative dMRI analyses with tractography via along-the-tract analyses for surgical outcomes prediction in epilepsy using a fully automated image analysis procedure. In Chapter 7 we adapt the along-the-tract measures to DKI using DKI-derived quantitative parameters and DKI-tractography and demonstrate improved sensitivity for detecting pathology in TLE. Improved diagnostic capabilities are of paramount importance in TLE as current limitations can significantly affect the quality of care for individual patients. In Chapter 8, we provide a brief conclusion for this work.

2

Development of Novel Kurtosis-Based Image Analysis Methods

Diffusion anisotropy is an important property of tissue microstructure. In this chapter we will begin exploring novel features of diffusion dynamics based on the directional dependence of the kurtosis tensor which relate to the anisotropic nature of diffusion in complex biological tissue. This chapter is based on the following peer-reviewed publication:

1. **Glenn GR**, Helpern JA, Tabesh A, Jensen JH. Quantitative assessment of diffusional kurtosis anisotropy. *NMR Biomed.* 2015;28:448-59.

Abstract

DKI measures the diffusion and kurtosis tensors to quantify restricted, non-Gaussian diffusion that occurs in biological tissue. By estimating the kurtosis tensor, DKI accounts for higher order diffusion dynamics, when compared to DTI, and consequently, it can describe more complex diffusion profiles. Here, we compare several measures of diffusional anisotropy which incorporate information from the kurtosis tensor, including kurtosis fractional anisotropy (KFA) and generalized fractional anisotropy (GFA) to the diffusion-tensor derived fractional anisotropy

(FA). KFA and GFA demonstrate a net enhancement relative to FA when multiple white matter fiber bundle orientations are present in both simulated and human data. In addition, KFA shows net enhancement in deep brain structures, such as the thalamus and the lenticular nucleus where FA indicates low anisotropy. Thus, KFA and GFA provide additional information relative to FA regarding diffusional anisotropy and may be particularly advantageous for assessing diffusion in complex tissue environments.

Introduction

Diffusion anisotropy measures are common for quantifying properties of tissue microstructure from diffusion MRI data. Among them, fractional anisotropy (FA) is the most widely used (40,41). However, FA has the shortcoming that it may take on small values, or in principle even vanish, despite the diffusion dynamics having significant angular dependence, for example, in white matter regions with multiple fiber bundle orientations (41-43). In addition, FA has been shown to be sensitive to partial volume effects (44-48) and the orientation dispersion of neurites and neurite density (49). For these reasons, it may be of interest to consider additional measures of diffusional anisotropy.

Since the introduction of the kurtosis tensor (29,30), investigators have proposed several anisotropy measures based on this quantity (31,50,51). Some of these measures incorporate information from the diffusion tensor and are therefore not directly analogous to FA for measuring anisotropy (50,51). However, a novel measure of anisotropy was recently proposed, which is purely a property of the kurtosis tensor and can be regarded as a natural extension of the FA concept to the kurtosis tensor (31). Here, we have termed this measure of anisotropy kurtosis

fractional anisotropy (KFA) and demonstrate that it provides distinct and complementary information about diffusional anisotropy when compared to FA.

In addition, generalized fractional anisotropy (GFA) (37) can be calculated from the diffusion and kurtosis tensors. In contrast to other measures of anisotropy, GFA has the advantage of describing anisotropy in the dODF which can be interpreted as the degree of preferential directional diffusion mobility, like FA, with the benefit of being able to accommodate more complex diffusion profiles.

The main purpose of this chapter is to describe and motivate the application of KFA and GFA, which can both be calculated directly from DKI datasets. In addition, we illustrate distinct features of KFA by comparing it with FA and alternative kurtosis-based measures of anisotropy for both numerical simulations and for in vivo human data.

Fractional Anisotropy

Fractional anisotropy (FA) is the most commonly used measure of diffusion anisotropy taken from the diffusion tensor. The original concept behind FA is to decompose the diffusion tensor into isotropic and anisotropic tensors, $\boldsymbol{D} = \bar{D}\boldsymbol{I}^{(2)} + \left(\boldsymbol{D} - \bar{D}\boldsymbol{I}^{(2)}\right)$, where $\boldsymbol{I}^{(2)}$ is the fully symmetric, second order isotropic tensor defined by its components, $I_{ij}^{(2)} = \delta_{ij}$, where δ_{ij} is the Kronecker delta. Then, FA is the ratio of the magnitudes of the anisotropic component and the diffusion tensor (40):

$$FA \equiv \sqrt{\frac{3}{2}} \cdot \frac{\left\|\boldsymbol{D} - \bar{D}\boldsymbol{I}^{(2)}\right\|_F}{\|\boldsymbol{D}\|_F}, \qquad [17]$$

where the normalization constant $\sqrt{3/2}$ is included so that FA values range from 0 to 1, and $\|\cdots\|_F$ indicates the Frobenius norm for a tensor $\boldsymbol{A}$ of rank N:

$$\|\boldsymbol{A}\|_F \equiv \sqrt{\sum_{i_1,i_2,\ldots,i_N}\left(A_{i_1,i_2,\ldots,i_N}\right)^2}. \qquad [18]$$

Note that the special case of $N = 1$ simply corresponds to the standard Euclidian vector norm, and the Frobenius norm is manifestly invariant under rotations.

This definition of FA can be rewritten into the conventional form by incorporating the relationships between the eigenvalues and the Frobenius norm of the diffusion tensor (40):

$$FA = \sqrt{\frac{3}{2}} \cdot \frac{\sqrt{(\lambda_1-\bar{D})^2+(\lambda_2-\bar{D})^2+(\lambda_3-\bar{D})^2}}{\sqrt{\lambda_1^2+\lambda_2^2+\lambda_3^2}}. \qquad [19]$$

Kurtosis Anisotropy

One method for examining anisotropy in the kurtosis tensor proposed by Hui et al. (50) is to sample directional kurtosis along the diffusion tensor eigenvectors $\boldsymbol{v_i}$ corresponding to each eigenvalue λ_i, such that $K_i = K(\boldsymbol{v_i})$, and then define kurtosis anisotropy (KA) with an analogous equation (50):

$$KA_\lambda = \sqrt{\frac{3}{2}} \cdot \frac{\sqrt{(K_1-K)^2+(K_2-K)^2+(K_3-K)^2}}{\sqrt{K_1^2+K_2^2+K_3^2}}, \qquad [20]$$

where $K = (K_1 + K_2 + K_3)/3$. One motivation for this definition is that in white matter regions, the eigenvectors of the diffusion tensor estimate orientations which are parallel and perpendicular to the orientation of a white matter fiber bundle, where diffusion displacement is expected to be minimally and maximally restricted. However, this definition is not analogous to the original definition of FA, and by applying a rank 2 diffusion tensor property to the rank 4 kurtosis tensor, it cannot reliably capture the full anisotropy in the kurtosis tensor. This observation prompted Poot et al. to propose an additional measure of KA (51):

$$KA_\sigma = \sqrt{\frac{1}{4\pi}\int d\boldsymbol{n}\,(K(\boldsymbol{n}) - \bar{K})^2}, \qquad [21]$$

which measures the standard deviation of the directional kurtosis. Although KA_σ evaluates variability of directional kurtosis measures, it is not normalized to a range of 0 to 1, as it scales with the magnitude of diffusional kurtosis, and it does not directly parallel the original definition of FA.

As noted by Eq. [12], $\bar{W}$ approximates $\bar{K}$ with the correspondence becoming exact for isotropic diffusion. So another possible measure of anisotropy taken from the diffusion and kurtosis tensors is given by:

$$KA_\mu = \left|1 - \frac{\bar{W}}{\bar{K}}\right|, \qquad [22]$$

where $|\cdots|$ is the absolute value. Although not directly analogous to FA, KA_μ does provide a measure of the degree to which the mean diffusional kurtosis differs from the mean of the kurtosis tensor as a consequence of diffusional anisotropy. It is of interest to investigate differences in $\overline{W}$ and $\overline{K}$ as $\overline{W}$ can be estimated from as few as 13 diffusion encoding directions, thereby significantly reducing the data acquisition time (31).

KA_λ, KA_σ, and KA_μ integrate information from both the diffusion and kurtosis tensors and are thus not pure measures of kurtosis tensor anisotropy. However, generalizing the original definition of FA to the kurtosis tensor is straightforward, and one finds (31):

$$KFA = \frac{\|\boldsymbol{W} - \overline{W}\boldsymbol{I}^{(4)}\|_F}{\|\boldsymbol{W}\|_F}, \qquad [23]$$

where $\boldsymbol{I}^{(4)}$ is the fully symmetric, rank 4 isotropic tensor defined by its components:

$$I_{ijkl}^{(4)} = \frac{1}{3}\left(\delta_{ij}\delta_{kl} + \delta_{ik}\delta_{jl} + \delta_{il}\delta_{jk}\right). \qquad [24]$$

Note that Eq. [24] gives the unique rank 4 tensor that is both symmetric and isotropic. The normalization is chosen so that KFA values range from 0 to 1. When $\|W\|_F = 0$, then Eq. [23] is indeterminate, but one can define this case to have KFA = 0.

The kurtosis and diffusion tensors are distinct physical quantities that encode different aspects of the diffusion dynamics (30). As a consequence, they can vary independently and in principle have no definite relationship to each other. FA and KFA are thus also distinct quantities,

either of which may vanish when the other is nonzero. Hence, they should be regarded as complementary rather than redundant metrics of diffusion anisotropy.

Generalized Fractional Anisotropy

A more comprehensive measure of diffusion anisotropy calculates anisotropy over the dODF as opposed to measures obtained directly from the diffusion or kurtosis tensors.

Eq. [19] can be extended to the dODF to define the generalized fractional anisotropy (GFA) by (37):

$$GFA = \frac{std(\psi_\alpha)}{rms(\psi_\alpha)}, \qquad [25]$$

where ψ_α is the dODF for radial weighting power α, $std(\psi_\alpha)$ is the standard deviation of ψ_α, and $rms(\psi_\alpha)$ is the root mean square of ψ_α. Since $std(\psi_\alpha)$ is zero for isotropic diffusion, and $rms(\psi_\alpha)$ is always greater or equal to than $std(\psi_\alpha)$, with the ratio increasing as the standard deviation, increases, i.e. as the difference between $\langle\psi_\alpha^2\rangle$ and $\langle\psi_\alpha\rangle^2$ increases, GFA values range from 0 to 1 indicating zero to maximal anisotropy in the dODF. Thus, GFA makes heuristic sense as a measure of anisotropy by normalizing the angular variability in the dODF by its magnitude, similar in spirit to both FA and KFA, in order to quantify the angular dependence of diffusion mobility.

The closed form solution to the kurtosis dODF given by Eq. [[15] depends only on the diffusion and kurtosis tensors. Thus GFA can be readily calculated from DKI data to indicate the anisotropy in the dODF by:

$$GFA = \sqrt{1 - \frac{\langle \psi_{\alpha,K} \rangle^2}{\langle \psi_{\alpha,K}^2 \rangle}}, \qquad [26]$$

which follows directly from Eq. [25], where $\psi_{\alpha,K}$ is the kurtosis dODF approximation. It should be noted that the GFA depends both on the approximation used for the dODF (e.g., kurtosis or q-ball) and on the choice of the radial weighting power, α. In this study, we used the kurtosis dODF with $\alpha = 4$ (32).

Multiple Gaussian Compartment Model

To illustrate differences in the anisotropy metrics, we consider some simple examples for a multiple, Gaussian compartment model having M, non-exchanging compartments, with each compartment having the water fraction f_m and a compartmental diffusion tensor, $\mathbf{D}^{(m)}$. The diffusion and kurtosis tensors can then be obtained as combinations of the diffusion tensors from each compartment by (33):

$$\mathbf{D} = \sum_{m=1}^{N} f_m \mathbf{D}^{(m)}, \qquad [27]$$

and,

$$W_{ijkl} = \frac{1}{\bar{D}^2}\left\{\left[\sum_{m=1}^{N} f_m \left(D_{ij}^{(m)} D_{kl}^{(m)} + D_{ik}^{(m)} D_{jl}^{(m)} + D_{il}^{(m)} D_{jk}^{(m)}\right)\right] - D_{ij}D_{kl} - D_{ik}D_{jl} - D_{il}D_{jk}\right\}. \quad [28]$$

For this model (29,30):

$$W(\boldsymbol{n}) = 3\,\frac{\delta^2 D(\boldsymbol{n})}{\bar{D}^2}, \quad [29]$$

where,

$$\delta^2 D(\boldsymbol{n}) \equiv \sum_{m=1}^{N} f_m \left\{\left[D^{(m)}(\boldsymbol{n}) - D(\boldsymbol{n})\right]^2\right\}, \quad [30]$$

is the variance of the diffusion coefficient, illustrating that the kurtosis tensor reflects overall heterogeneity in the diffusion environment.

Because we are interested in measuring differences in isotropic and anisotropic diffusion, we consider combinations of cylindrically symmetric, anisotropic tensors, defined with eigenvalues of $\lambda = [\lambda_{\parallel}, \lambda_{\perp}, \lambda_{\perp}]$, where $\lambda_{\parallel}$ is the parallel or principal eigenvalue and $\lambda_{\perp}$ are the perpendicular eigenvalues, which represent idealized Gaussian diffusion in white matter fiber bundles, and the rank 2 isotropic tensor, $I^{(2)}$, $(FA = 0)$, which may, for example, represent unrestricted diffusion in cerebrospinal fluid.

To evaluate the effects of changing the ratio of $\lambda_{\parallel}$ and $\lambda_{\perp}$ on each of the parameter estimates, we varied $\lambda_{\perp}$ while keeping $\lambda_{\parallel}$ set at 1.7 μm^2/ms for a single diffusion compartment, $\boldsymbol{D_1}$. Because

this represents idealized Gaussian diffusion with zero kurtosis, we then increased diffusional heterogeneity by adding a second, equivalently oriented compartment, $\boldsymbol{D_2} = 2\boldsymbol{D_1}$, resulting in a non-zero kurtosis tensor. To evaluate the effects of crossing fibers on anisotropy measures, we consider examples with 2 or 3 crossing fiber bundles with $\lambda = [1.7, 0.3, 0.3]$ μm^2/ms and separation angles between the principal eigenvectors ranging between 1 and 90 degrees. For simplicity, we considered compartments with equal water fractions.

For a given separation angle, θ, the orientation for the principle eigenvectors, $\boldsymbol{v_m}$, of each tensor can be readily calculated. For example, for the case with three anisotropic fiber bundles, the first orientation was given by $\boldsymbol{v_1} = [\cos(\theta/2), \sin(\theta/2), 0]^T$, the second orientation was given by $\boldsymbol{v_2} = [\cos(\theta/2), -\sin(\theta/2), 0]^T$, and the third orientation was chosen to be separated from both $\boldsymbol{v_1}$ and $\boldsymbol{v_2}$ by θ, by $\boldsymbol{v_3} = [\cos(\phi), 0, \sin(\phi)]^T$, where $\phi = \cos^{-1}[(1 - 2\sin^2(\theta/2))/\cos(\theta/2)]$. The corresponding diffusion tensor for each individual compartment was then defined as $\boldsymbol{D_m} = \boldsymbol{R_m} * diag([1.7, 0.3, 0.3]) * \boldsymbol{R_m}$, where $\boldsymbol{R_m} = \left[(\boldsymbol{v_m} + \boldsymbol{x})(\boldsymbol{v_m} + \boldsymbol{x})^T / \left(\boldsymbol{v_m^T v} + 1\right) - \boldsymbol{I}\right]$, and $\boldsymbol{x} = [1, 0, 0]^T$.

To avoid numerical artifacts, directional kurtosis estimates used to calculate KA_λ were regularized by setting $K(\boldsymbol{n}) = 1 \times 10^{-9}$ when $K(\boldsymbol{n}) < 1 \times 10^{-9}$. In addition, in the case where the crossing angle between multiple fiber bundles was 90°, the eigenvectors used to evaluate KA_λ were fixed by interpolation to avoid random variation in KA_λ.

Data Acquisition

DKI datasets were acquired for 5 healthy, adult volunteers ranging in age from 27 to 53, with a 3T TIM Trio MRI scanner (Siemens Medical, Erlangen, Germany) using a vendor-supplied diffusion sequence, 3 b-values of 0, 1000, and 2000 s/mm^2, and 60 isotropically distributed gradient directions to estimate the diffusion and kurtosis tensors. Acquisition parameters used were TR = 7200 ms, TE = 103 ms, voxel dimensions = 2.5 × 2.5 × 2.5 mm^3, matrix size × number of slices = 88 × 88 × 52, parallel imaging factor of 2, bandwidth = 1352 Hz/Px, and a 32 channel head coil with adaptive combine mode. To estimate inter- and intra-subject variability, 3 independent DKI datasets and a total of 25 images with no diffusion weighting (b0 images) were acquired for each subject. Each independent DKI acquisition took 16 min, and the full DKI acquisition with a total of 25 b0 images took 51 min. An additional MPRAGE sequence was also acquired for each subject for anatomical reference.

Image Analysis

To correct for subject motion, all b0 images for each subject were co-registered to the subject's first b0 image using SPM8 (Wellcome Trust Center for Neuroimaging, London, UK) with an affine, rigid body transformation with the normalized mutual information cost function and trilinear interpolation. In the case where the co-registered b0 image came from an independent DKI acquisition, the rigid-body transformation was also applied to all DWIs of that dataset. An average DKI dataset was then created by averaging all 25 independent b0 images and all 3 independent images for each applied diffusion encoding gradient.

DKI processing was performed by a previously described method using Gaussian smoothing with a full-width at half maximum of 1.25 times the voxel dimensions to minimize the effects of noise and misregistration, and tensor fitting was then performed using a constrained linear least

squares algorithm (52). Since our analyses included independent DKI datasets with only one b0 image, $\ln(S_0)$ was included as an unknown parameter to be estimated resulting in a total of 22 unknown parameters to be determined. The kurtosis ODF was evaluated using in-house software. GFA was calculated in each voxel by evaluating the kurtosis ODF for 1281 points spread evenly over one half of a spherical shell resulting in a separation angle of approximately 4.3 degrees between each point and its nearest neighbors. The orientation of each local maxima pair was estimated by an exhaustive grid search over these 1281 points followed by the non-linear quasi-Newton method for iterative optimization.

To analyze anisotropy measures in different regions of interest (ROIs) across the 5 healthy volunteers, the FA maps from the average DKI datasets were normalized to the ICBM-DTI-81 FA white matter atlas (53) using SPM8 with non-linear transformation and trilinear interpolation. The transformation for the average DKI dataset was also applied to all DKI-derived parameter maps from each of the independent DKI datasets. White matter ROIs analyzed (and the number of voxels they contain, n) include the full white matter ROI (n = 170,006) corpus callosum (CC) (n = 35,291), cingulum bundle (CB) (n = 5,093), superior longitudinal fasciculus (SLF) (n = 13,212), and corona radiata (CR) (n = 36,151). Gray matter ROIs were also created for the lenticular nucleus (LN) (n = 6,815), which consists of the globus pallidus and the putamen of the basal ganglia, and the thalamus (Thal) (n = 4,293). The LN was defined bilaterally as the area between the internal capsule (IC) and the external capsule (EC) in the white matter template. The Thal was manually segmented using the white matter template overlaid on the T2-weighted template image, to be at or above the level of the splenium of the CC, lateral to the lateral ventricles, and medial to the IC.

To highlight differences between the anisotropy parameters, parameter difference maps were calculated as the difference between selected parameters of interest. To emphasize the average group difference in the anisotropy parameters, these maps were generated from the mean of the normalized parameter maps across all subjects.

Results

To illustrate differences in quantitative measures of diffusion anisotropy, all anisotropy measures are evaluated from simulated data with the multiple Gaussian compartment model in Figure 2 for a single diffusion orientation with non-zero kurtosis and in Figures. 3 and 4 for 2 and 3 crossing white matter fiber bundles, respectively.

In Figure 2, increasing $\lambda_\perp$ relative to $\lambda_\parallel$ decreases FA, GFA, and KFA. In the case with only anisotropic diffusion, this has no effect on KA_λ or KA_σ since the directional kurtosis is constant, $K(\boldsymbol{n}) = 1/3$, resulting in $KA_\lambda = 0$ and $KA_\sigma = 0$. KA_μ decreases as diffusional anisotropy decreases. Adding an isotropic compartment decreases both FA and KFA, but causes a slight increase in KFA by increasing variability in the directional diffusional heterogeneity. The addition of isotropic diffusion has variable effects on the other kurtosis anisotropy parameters.

In Figures. 3 and 4, FA is reduced for fiber bundle orientations at high crossing angles and vanishes for the 3 fiber bundle example with a 90° crossing angle. KFA, on the other hand, is less sensitive to the crossing angle in cases where there is no isotropic diffusion, but shows a dip at a particular crossing angle as the relative magnitude of the contributions from the isotropic and anisotropic compartments to the diffusional heterogeneity are reversed. For the case with 2 anisotropic white matter fiber bundles and no isotropic diffusion, KFA is constant, and it can be

evaluated explicitly as $KFA = \sqrt{13/15}$. A mathematical derivation of this result is included in the appendix to further explore the effects of the adjustable parameters on the kurtosis tensor and to highlight differences between KFA and FA. The overall shape of the dODF most accurately depicts the simulated fiber bundle orientation across all crossing angles, thus for this model, GFA may be the most accurate measure quantifying preferential diffusion mobility in regions with crossing fibers. In Figure 3A, KA_λ is zero, resulting from regularization, as the eigenvalues of the diffusion tensor point to directions with approximately zero diffusional kurtosis. KA_σ scales with the magnitude of the mean diffusional kurtosis, so in Figures 3A and 4A, KA_σ vanishes at small crossing angles, as the overall diffusion dynamics with this model become increasingly Gaussian. The magnitude of KA_μ is typically small, particularly in cases with no isotropic diffusion, but for this particular model, when there at low crossing angles and isotropic diffusion, KA_μ can be appreciatively large.

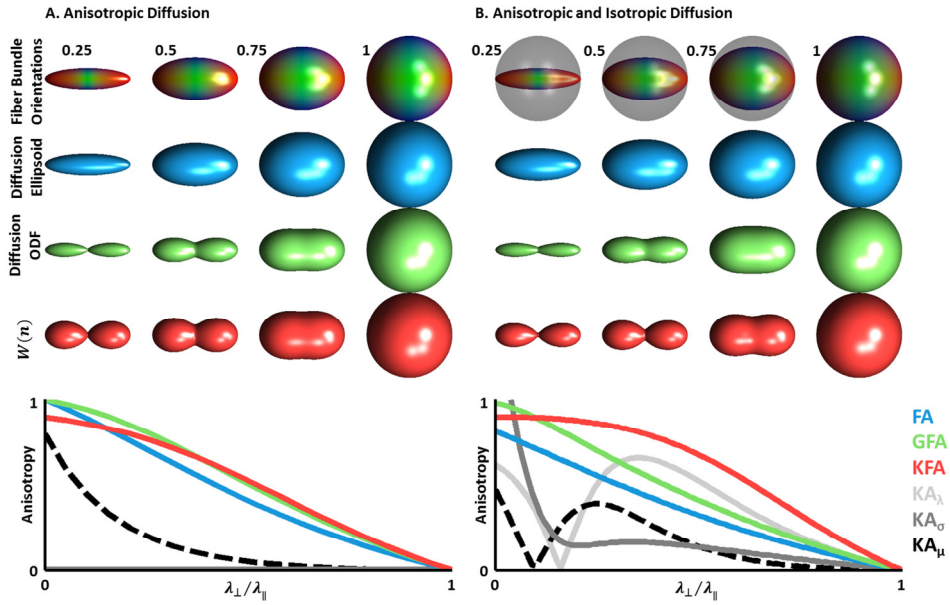

Figure 2. Multiple Gaussian compartment model for one white matter fiber bundle orientation with only anisotropic diffusion (A) and an additional isotropic compartment (B). The principal eigenvector was set at $\lambda_\parallel = 1.7\ \mu m^2/ms$, and the 2 perpendicular eigenvectors, $\lambda_\perp$ were varied so that the ratio $\lambda_\perp/\lambda_\parallel$ varied from 0 to 1. Diffusional heterogeneity was increased to cause a nonzero kurtosis tensor by adding a second, identically oriented diffusion tensor which was 2 times the magnitude of the first, $\boldsymbol{D_2} = 2\boldsymbol{D_1}$. Numbers at the top of each column represent the ratio $\lambda_\perp/\lambda_\parallel$ for that column. The fiber bundle orientation depicts the orientation the diffusion ellipsoid for each of the separate compartments, where the colored ellipsoid represents simulated white matter fiber bundles and the gray spheres represent simulated isotropic diffusion. The blue diffusion ellipsoid is taken from the net diffusion tensor and is a way of visualizing FA. The dODF is used to calculate GFA and is taken from Eq. [13], using the kurtosis diffusion displacement PDF representation (29). $W(\boldsymbol{n})$ illustrates the directional dependence of the kurtosis tensor and is calculated by Eq. [8]. The plots at the bottom of each column represent the anisotropy parameter values for $\lambda_\perp/\lambda_\parallel$ ratios between 0 and 1. Renderings of the diffusion ellipsoid, dODF, and $W(\boldsymbol{n})$ are not shown to scale to emphasize anisotropic features, as FA, KFA, or GFA are not affected by the overall scaling. In panel (A), KA_λ and KA_σ are always zero, as discussed in the text.

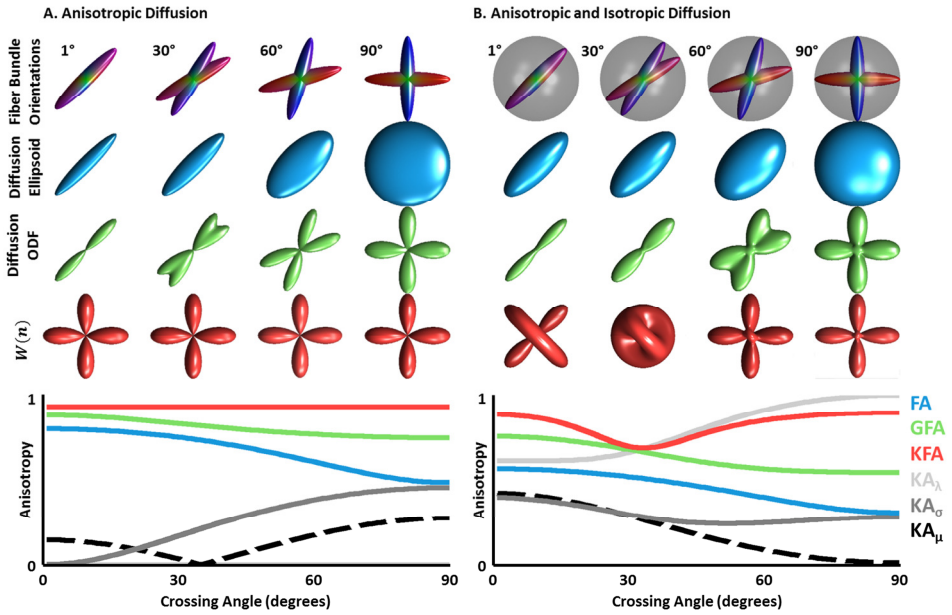

Figure 3. Multiple Gaussian compartment model for 2 crossing fibers with only anisotropic diffusion (A) and an additional isotropic compartment (B). Numbers at the top of each column represent the separation for that column, and the three-dimensional renderings depicted are calculated from the same equations as those in Figure 2. The plots at the bottom of each column represent the anisotropy parameter values for simulated crossing angles for each integer value between 1 and 90 degrees.

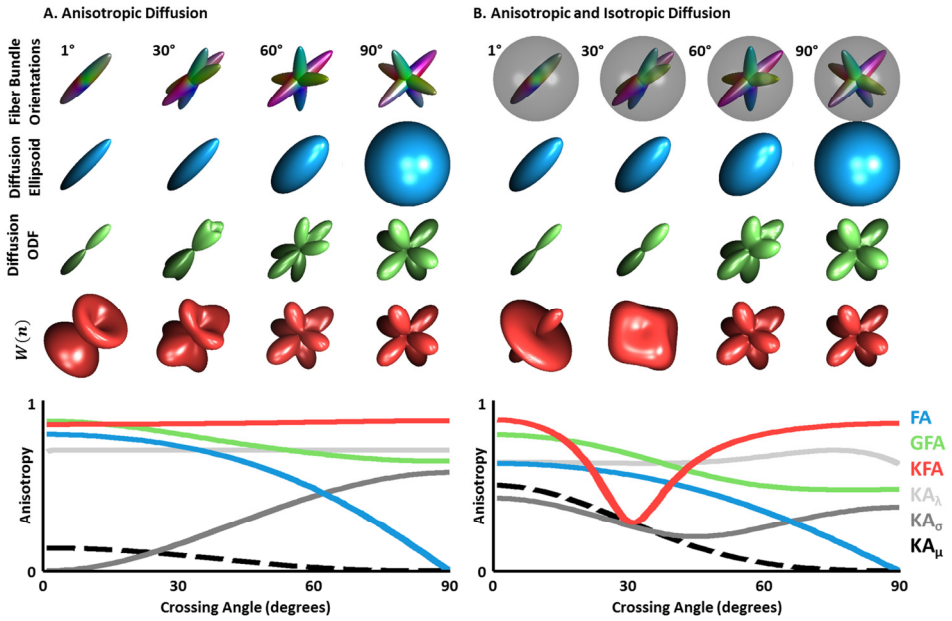

Figure 4. Multiple Gaussian compartment model for 3 crossing fibers with only anisotropic diffusion (A) and an additional isotropic compartment (B). Numbers at the top of each column represent the separation for that column, and the three-dimensional renderings depicted are calculated from the same equations as those in Figure 2. The plots at the bottom of each column represent the anisotropy parameter values for simulated crossing angles for each integer value between 1 and 90 degrees. For this example, both FA and KA_μ drop to zero at 90 degrees, while all other measures are non-zero.

Representative parameter maps for the 6 different anisotropy measures from a single healthy volunteer are given in Figure 5. In general, GFA is greater than FA, but the two values are closely correlated. KFA shows similar enhancement as FA in white matter regions that are expected to show diffusional anisotropy. However, KFA also shows enhancement in gray matter regions such as the Thal and LN where FA values are relatively low. In addition, KFA shows enhancement in regions between the CC and CB, which could demonstrate complex diffusion profiles due to separate contributions from these two large, well-defined fiber bundles. KA_λ and KA_σ show enhancement in regions with expected diffusional anisotropy, but the anisotropic regions are

typically narrower, particularly when compared to GFA. KA_{μ} demonstrates anisotropy in expected regions, but the values are much less than other measures of anisotropy.

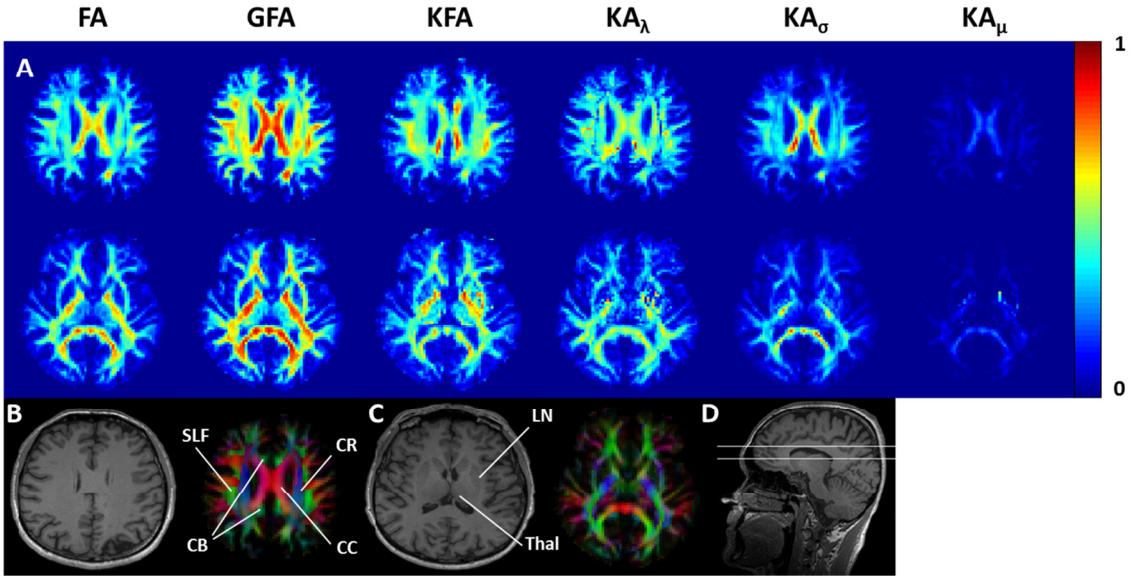

Figure 5. Representative anisotropy maps from a healthy volunteer. (A) Anisotropy maps for two slices taken from a healthy volunteer. MPRAGE and GFA color map for the first slice (B) and second slice (C) point out a few regions of interest. (D) Sagittal MPRAGE image with white bars indicates the slice location for the parameter maps.

The specific ROIs analyzed as well as differential anisotropy maps are shown in Figure 6. GFA is typically greater than FA so the difference between GFA and FA is positive throughout the white matter. However, this difference can be enhanced in regions where there is complex tissue architecture, as may occur in voxels with crossing white matter fibers from the SLF, CR, and CC; the CC and CB; or in the pons. The difference between KFA and FA is also enhanced in these regions, particularly in the boundary regions between white matter ROIs, where contributions to the overall diffusion dynamics from crossing fibers with high crossing angles can cause FA to be anomalously low. The difference between KFA and FA is also increased in deep

brain structures such as the LN and Thal, where FA typically indicates low diffusional anisotropy. Crossing fiber regions detected from the kurtosis dODF are illustrated by the maps in the orientations column of Figure 6, which gives the total number of local-maxima pair detected in each voxel. The difference between KFA and FA is generally enhanced in regions where there are multiple fiber bundle orientations. GFA is increased relative to KFA in white matter regions with high diffusional anisotropy, such as the CC. This trend is similar with FA relative to KFA, but the difference is significantly less.

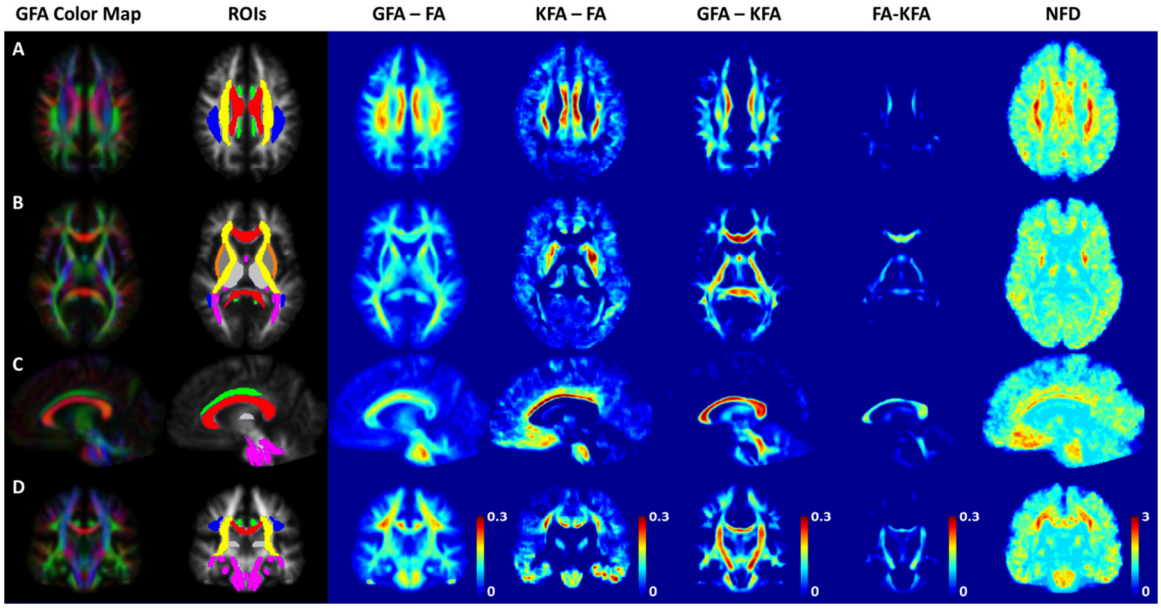

Figure 6. Differential anisotropy maps. Representative transverse (A) and (B), sagittal (C), and coronal (D) slices from the differential maps highlight differences in the anisotropy parameters. The first column illustrates the average of the normalized GFA colormaps (37) illustrating white matter structures in the normalized data. The second column overlays the template ROIs on the mean GFA map. The ROIs shown are CC (red), CB (green), SLF (blue), CR and IC (yellow), EC (orange), other white matter structures (magenta), Thal (light grey), and LN (dark grey). The differential anisotropy maps shown are indicated at the top of each column, and the orientations column shows the number of fiber bundle orientations estimated from each voxel from the kurtosis dODF (32) averaged across all subjects. There is a strong correlation between regions enhanced in the KFA-FA differential map and regions with multiple fiber bundle orientations detected, depicted in the orientations maps.

Figure 7 shows representative slices from the ICBM white matter template as well as the group average for the normalized FA, GFA, and KFA images. The template and the average of the normalized FA images are highly similar, validating the normalization procedure. The GFA map is enhanced relative to the FA map and the white matter regions identified with GFA are slightly broader.

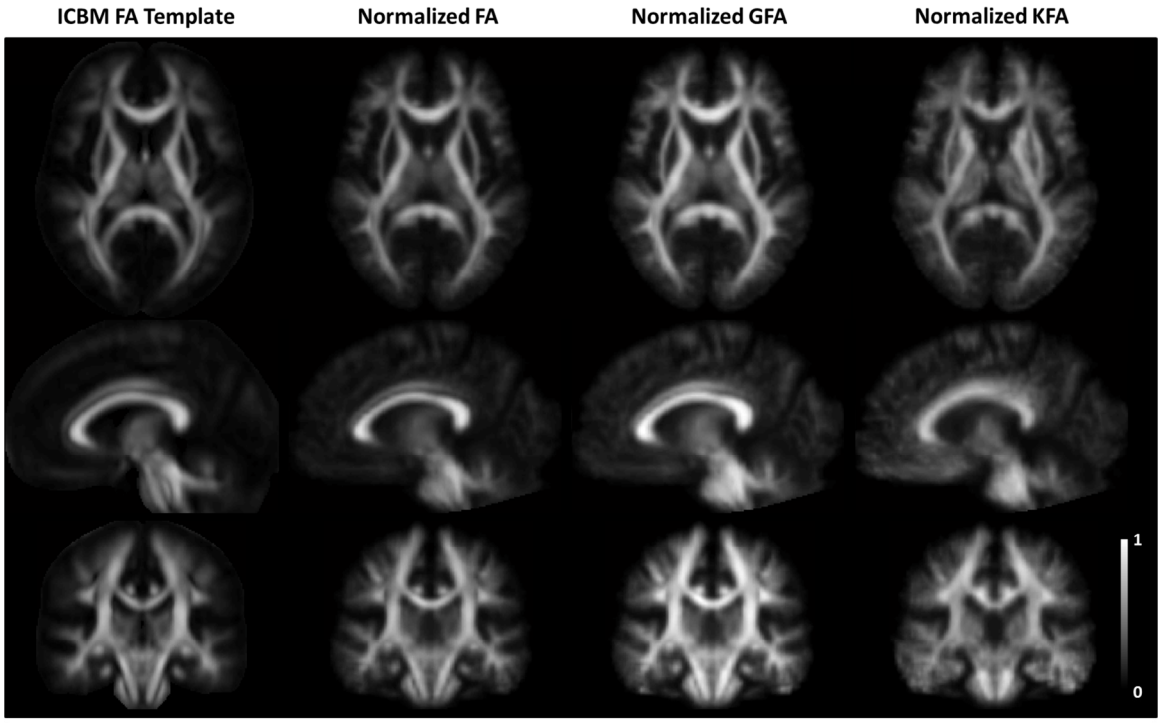

Figure 7. Representative transverse, sagittal, and coronal slices from the ICBM white matter template as well as the normalized FA, GFA, and KFA parameter maps.

Discussion

KFA measures anisotropy in the fourth order kurtosis tensor, is mathematically analogous to FA, and provides complementary information about anisotropy in diffusion dynamics. Other measures of anisotropy, such as KA_{λ}, KA_{σ}, and KA_{μ} measure anisotropy in diffusional kurtosis but they are

not specific to the kurtosis tensor, as they also incorporate information from the diffusion tensor. It should be noted that KFA is purely a function of the kurtosis tensor and does not correspond precisely to the angular variability in the diffusional kurtosis (which depends on both the kurtosis and diffusion tensors).

GFA measures anisotropy in the dODF as a way of quantifying preferential diffusion mobility. When there is only one fiber bundle orientation, GFA and FA are strongly correlated suggesting they provide similar information. However, by incorporating higher-order information from the kurtosis tensor, GFA can account for anisotropy from more complex diffusion profiles compared to FA. As a result, GFA may sometimes be a more appropriate measure of diffusional anisotropy, particularly in regions with crossing white matter fiber bundles, where FA may underestimate the degree of diffusional anisotropy.

We have used multiple, non-exchanging, Gaussian compartment models as simple illustrations of the intricate relationships between the underlying diffusion dynamics and quantitative measures of diffusion anisotropy. These are particularly apparent when there are multiple anisotropic diffusion compartments with preferential diffusion occurring along different orientations, as occurs in vivo when white matter fiber bundles cross. Since a single quantitative anisotropy measure cannot characterize all features of the underlying diffusion dynamics, it may be of interest to combine anisotropy measures in analysis of complex tissue architecture. We note in particular that the FA may vanish even when the diffusion is not isotropic (see, for example, Figure 4), in which case the kurtosis anisotropies may be especially useful. In Figures 3B and 4B there is a dip in KFA at a specific crossing angle. This occurs in this model as the crossing angle affects the overall degree of non-Gaussian diffusion in the anisotropic compartments, and at a

specific crossing angle, the relative magnitude of the effects of the isotropic and anisotropic compartments to the overall diffusional heterogeneity inverts, as can be seen in the change in morphology of $W(\boldsymbol{n})$.

It is of interest that KA_{μ} is typically very small in simulations (Figures 2-4) and for *in vivo* experiments (Figure 5), which is consistent with the results of Hansen et al. (31). This supports the use of $\overline{W}$ as an alternative to $\overline{K}$ for characterizing the overall kurtosis. This is of practical importance, since an efficient image acquisition protocol for $\overline{W}$ has recently been proposed, which may be particularly advantageous in the acute setting where scan time is of paramount concern (31).

Conclusion

Diffusion anisotropy is an important aspect of tissue microstructure. However, anisotropy measures from the diffusion tensor, such as FA, can potentially take on small values despite significant diffusion anisotropy, due to the presence of complex fiber bundle geometries. As a consequence, alternative measures of diffusion anisotropy, such as the KFA and GFA, may be of interest. KFA is based purely on the kurtosis tensor, and is distinct from the conventional FA measure, as the kurtosis and diffusion tensors describe different features of the diffusing environment and can vary independently. It differs from other kurtosis anisotropy measures in depending only on the kurtosis tensor and in being defined in a manner more conceptually analogous to the original definition of the FA. GFA, on the other hand, uses the dODF to quantify the degree of preferential diffusion mobility and thereby effectively integrates information from both the diffusion and kurtosis tensors. By measuring higher order diffusion anisotropy, KFA and

GFA can help to better characterize more complex diffusion profiles and may be particularly useful for regions where white matter fiber bundles cross.

Appendix: Kurtosis Fractional Anisotropy for Two Identical Crossing Fibers

In order to better understand the physical meaning of the kurtosis fractional anisotropy, consider two identical crossing fiber bundles intersecting at an angle of 2θ. As in the simulation experiments of Figure 3, assume that both fiber bundles are non-exchanging, cylindrically symmetric, Gaussian compartments, with the diffusion tensor eigenvalues$\lambda_{\parallel} \geq \lambda_{\perp}$. The fiber bundles both lie parallel to the *xy*-plane and are oriented at angles of $\pm\theta$ with respect to the *x*-axis. The diffusion tensor for the first fiber bundle (A) is

$$\boldsymbol{D}_A = \boldsymbol{R}\boldsymbol{D}_0\,\boldsymbol{R}^T \qquad [31]$$

and the diffusion tensor for second bundle is

$$\boldsymbol{D}_B = \boldsymbol{R}^T\boldsymbol{D}_0\boldsymbol{R}, \qquad [32]$$

where

$$\boldsymbol{D}_0 = \begin{bmatrix} \lambda_{\parallel} & 0 & 0 \\ 0 & \lambda_{\perp} & 0 \\ 0 & 0 & \lambda_{\perp} \end{bmatrix}, \qquad [33]$$

and

$$\boldsymbol{R} = \begin{bmatrix} R_{11} & R_{12} & 0 \\ R_{21} & R_{22} & 0 \\ 0 & 0 & 1 \end{bmatrix} = \begin{bmatrix} \cos\theta & -\sin\theta & 0 \\ \sin\theta & \cos\theta & 0 \\ 0 & 0 & 1 \end{bmatrix}. \quad [34]$$

The matrix $\boldsymbol{R}$ rotates a vector in the *xy*-plane by an angle θ. As for all rotation matrices, $\boldsymbol{R}^{-1} = \boldsymbol{R}^T$. If the water fraction is f for bundle A and $(1-f)$ for bundle B, then the total diffusion tensor is

$$\boldsymbol{D} = f\boldsymbol{D}_A + (1-f)\boldsymbol{D}_B. \quad [35]$$

The components of the corresponding kurtosis tensor, $\boldsymbol{W}$, are given by

$$W_{ijkl} = \frac{1}{\bar{D}^2}\left[f\left(D_{A,ij}D_{A,kl} + D_{A,ik}D_{A,jl} + D_{A,il}D_{A,jk}\right) + (1-f)\left(D_{B,ij}D_{B,kl} + D_{B,ik}D_{B,jl} + D_{B,il}D_{B,jk}\right) - D_{ij}D_{kl} - D_{ik}D_{jl} - D_{il}D_{jk}\right], \quad [36]$$

where $\bar{D} = Tr(\boldsymbol{D})/3$ is the mean diffusivity, $D_{A,ij}$ are the components of $\boldsymbol{D}_A$, and $D_{B,ij}$ are the components of $\boldsymbol{D}_B$. With the help of Eq. [35], Eq. [36] may be recast as

$$W_{ijkl} = \frac{f(1-f)}{\bar{D}}\left[\left(D_{A,ij} - D_{B,ij}\right)\left(D_{A,kl} - D_{B,kl}\right) + \left(D_{A,ik} - D_{B,ik}\right)\left(D_{A,jl} - D_{B,jl}\right) + \left(D_{A,il} - D_{B,il}\right)\left(D_{A,jk} - D_{B,jk}\right)\right]. \quad [37]$$

Now consider the difference matrix

$$\delta \boldsymbol{D} \equiv \boldsymbol{D}_A - \boldsymbol{D}_B = \boldsymbol{R}\boldsymbol{D}_0\boldsymbol{R}^T - \boldsymbol{R}^T\boldsymbol{D}_0\boldsymbol{R}. \qquad [38]$$

This may be rewritten as

$$\delta \boldsymbol{D} = \boldsymbol{R}(\boldsymbol{D}_0 - \lambda_\perp \boldsymbol{I})\boldsymbol{R}^T - \boldsymbol{R}^T(\boldsymbol{D}_0 - \lambda_\perp \boldsymbol{I})\boldsymbol{R} = (\lambda_\parallel - \lambda_\perp)(\boldsymbol{R}\boldsymbol{P}\boldsymbol{R}^T - \boldsymbol{R}^T\boldsymbol{P}\boldsymbol{R}), \qquad [39]$$

where $\boldsymbol{I}$ is the identity matrix and

$$\boldsymbol{P} \equiv \begin{bmatrix} 1 & 0 & 0 \\ 0 & 0 & 0 \\ 0 & 0 & 0 \end{bmatrix}. \qquad [40]$$

By using the fact that $R_{12} = -R_{21}$, a direct calculation then shows that

$$\delta \boldsymbol{D} = 2(\lambda_\parallel - \lambda_\perp)R_{11}R_{21}\boldsymbol{Q}, \qquad [41]$$

with

$$\boldsymbol{Q} \equiv \begin{bmatrix} 0 & 1 & 0 \\ 1 & 0 & 0 \\ 0 & 0 & 0 \end{bmatrix}. \qquad [42]$$

From Eqs. [34], [37], [38], and [41], we then see that

$$W_{ijkl} = \frac{f(1-f)}{\bar{D}^2}(\lambda_{\parallel} - \lambda_{\perp})^2 \sin^2(2\theta)\left(Q_{ij}Q_{kl} + Q_{ik}Q_{jl} + Q_{il}Q_{jk}\right). \quad [43]$$

Thus, the parameters f, $\lambda_{\parallel}$, $\lambda_{\perp}$, and θ only affect the overall scaling of $\boldsymbol{W}$. Since KFA is invariant with respect to this scaling factor, KFA is strictly independent of f, $\lambda_{\parallel}$, $\lambda_{\perp}$, and θ. By applying the definition of KFA, one may show that it always equals $\sqrt{13/15} \approx 0.931$.

For this same model, FA, in contrast, depends significantly on all four adjustable parameters, illustrating the distinct information provided by FA KFA; FA reflects the directional dependence of the diffusivity mobility, while, for multiple Gaussian compartment models, KFA reflects the directional dependence of the variance of the compartmental diffusivities.

3

Kurtosis-Based Microstructural Modeling

Microstructural modeling aims to increase the specificity of dMRI for characterization of specific features of biological tissue, as these may be differentially affected by disease processes. In this chapter, we will continue to explore novel properties of the kurtosis tensor using various microstructural modeling techniques. The models under consideration assume the kurtosis tensor is affected by particular configurations of microstructural tissue compartmentalization, which are leveraged to estimate specific modeling parameters. This chapter is based on the following peer-reviewed publications:

1. Hui ES, **Glenn GR**, Helpern JA, Jensen JH. Kurtosis analysis of neural diffusion organization. *Neuroimage*. 2015;106:391-403.
2. Jensen JH, **Glenn GR**, Helpern JA. Fiber Ball Imaging. *Neuroimage*. 2016;124:824-33.

Abstract

Typical diffusion parameters from DKI, such as mean diffusivity (MD), fractional anisotropy (FA), and mean kurtosis (MK) characterize general, non-specific changes in tissue microstructure, which may obscure the determination of causal relationships between quantitative dMRI parameters and tissue microstructure. To help better understand the meaning of the

observed changes in the context of pathological disease mechanisms, it is of interest to develop more specific biomarkers. In this chapter, DKI-based modeling techniques are compared to a novel high angular resolution diffusion imaging (HARDI) method termed fiber ball imaging (FBI) for the characterization of specific white matter tissue properties in two healthy volunteers.

Introduction

In addition to quantifying features of *in vivo* water diffusion and estimating the orientation of white matter fiber bundles, the kurtosis tensor may also be used to facilitate more detailed quantitative models of biological tissue architecture. The key idea underlying these methods is that by assuming tissue microstructure consists of multiple, non-exchanging compartments with Gaussian diffusion, the kurtosis tensor can be mathematically represented as a combination of the compartmental diffusion tensors. From this assumption there are a variety of methods which can be used to relate properties of the dMRI signal to specific features of the underlying tissue microstructure.

One such approach is the white matter model (WMM) proposed by Fieremans et al. (54) The WMM assumes that white matter consist of two, non-exchanging Gaussian compartments, the extra-axonal space (EAS) and intra-axonal space (IAS), where the IAS consists of highly aligned white matter fiber bundles. Then, the fraction of MRI visible water confined to the intra-axonal space, the axonal water fraction (AWF), may be evaluated as (54):

$$AWF = \frac{K_{max}}{K_{max}+3}, \qquad [44]$$

where K_{max} is the maximum directional kurtosis value in all directions, and the diffusivity in the IAS, the intra-axonal diffusivity (D_a), may be defined for an arbitrary direction, $\boldsymbol{n}$, by (54):

$$D_a(\boldsymbol{n}) = D(\boldsymbol{n})\left[1 - \sqrt{\frac{K(\boldsymbol{n})(1-AWF)}{3\,AWF}}\right]. \qquad [45]$$

Since Eq. [45] is true for any direction, the compartmental diffusion tensor for the IAS, $\boldsymbol{D_a}$, may be reconstructed using standard diffusion tensor estimation techniques, as $D_a(\boldsymbol{n}) = \boldsymbol{n^T D_a n}$. Then the intra-axonal diffusivity is given by:

$$D_a = tr(\boldsymbol{D_a}), \qquad [46]$$

where $tr(\cdots)$ is the trace operator.

WMM-based parameters, such as AWF and D_a, have been demonstrated to be sensitive to disease related pathology in a variety of disease states including Alzheimer's disease (55,56), multiple sclerosis (57), autism (58), acute axonal injury (59,60), and traumatic brain injury (60), and they can provide insight into specific pathological mechanisms underlying white matter changes such as demyelination (61,62). However, the WMM is only mathematically valid in regions with a single population of aligned white matter fiber bundles. Because brain tissue microstructure can consist of more complex configurations, such as crossing white matter fiber bundles, it is of interest to develop more general microstructural modeling frameworks. One such method using the kurtosis tensor is kurtosis analysis of neural diffusion organization (KANDO)

proposed by Hui et al.(63). As in the WMM, KANDO assumes that the measured kurtosis tensor reflects the underlying organization of restricted compartments of Gaussian diffusion by:

$$W^*_{ijkl} = \frac{1}{\bar{D}^2}\left\{\left[\sum_{n=0}^{N} f_n \left(D^{(n)}_{ij}D^{(n)}_{kl} + D^{(n)}_{ik}D^{(n)}_{jl} + D^{(n)}_{il}D^{(nm)}_{jk}\right)\right] - D_{ij}D_{kl} - D_{ik}D_{jl} - D_{il}D_{jk}\right\}, \quad [47]$$

where $N+1$ is the number of compartments, $\boldsymbol{D}^{(n)}$ is the compartmental diffusion tensor for the n^{th}compartment, f_n is the compartmental water fraction, and the asterisk superscript indicates this is the theoretically predicted kurtosis tensor from the underlying tissue model.

The basic computational problem of KANDO is then to select the set of unknown parameters for a given model (a_m) which minimize the difference between the experimental (observed) kurtosis tensor, $\boldsymbol{W}$, and the model-predicted kurtosis tensor $\boldsymbol{W}^*(a_m)$, where the functional dependence of the predicted kurtosis tensor has been made explicit. The cost function for this general estimation problem is given by (63):

$$C \equiv \sum_{i,j,k,l=1}^{3} \left|\boldsymbol{W}^*_{i,j,k,l}(a_m) - \boldsymbol{W}_{i,j,k,l}\right|^2, \quad [48]$$

which can be minimized with conventional non-linear optimization algorithms to solve for the set of unknown model parameters.

KANDO is a general computational framework for estimating model parameters based on DKI data. Thus, it is compatible with a variety of potential microstructural models. In this chapter we will focus on two models, including a single fiber bundle model (Model 1) comprised of white

matter with unidirectional axons and a dODF model comprised of white matter with potential crossing fibers (Model 2) (63). Model 1 is similar to the WMM proposed by Fieremans et al., except the intra-axonal diffusivity is a model parameter which varies during the optimization. Model 2 incorporates information from the kurtosis dODF and can potentially accommodate voxels with more complex fiber bundle geometries. In all cases, the glial cells are assumed to be in fast exchange with the EAS. A schematic for Model 2 is given in Figure 8.

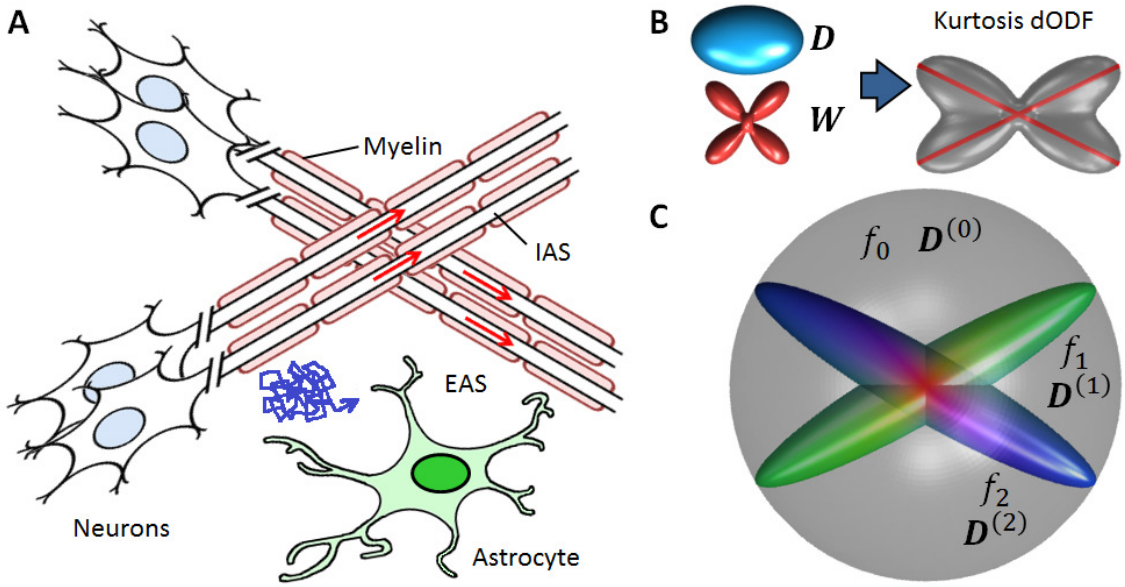

Figure 8. Schematic for Model 2 representing white matter regions with crossing fibers. (A) KANDO assumes that the IAS is isolated from the EAS by myelin and no water is exchanged between the compartments. Diffusion of water molecules in the IAS and EAS are indicated by the red and blue arrows, respectively. (B) DKI estimates the net diffusion tensor (blue) and the net kurtosis tensor (red) to characterize the overall non-Gaussian diffusion dynamics from the underlying tissue architecture. The diffusion and kurtosis tensors are combined to estimate the kurtosis dODF (gray), which can detect multiple fiber bundle orientations (red lines). (C) Taken together the diffusion tensor, the kurtosis tensor, and the kurtosis dODF can be used to estimate diffusion dynamics in each individual compartment, where f_0 and $\boldsymbol{D}^{(0)}$ indicate the volume fraction and compartmental diffusion tensor of the EAS (gray sphere), f_1, $\boldsymbol{D}^{(1)}$, f_2, and $\boldsymbol{D}^{(2)}$indicate the volume fraction and compartmental diffusion in first and second fiber bundles (green and blue ellipsoids, respectively). By applying constraints of the WMM, there are only 2 independent parameters that need to be estimated from KANDO, which determine the AWF and the intra-axonal diffusivity, which then yield information on diffusion dynamics in the IAS and EAS.

To test these models, we will compare with a novel technique proposed by Jensen et al., termed Fiber Ball Imaging (FBI) (64). FBI is a high angular resolution diffusion imaging (HARDI) approach which uses strong diffusion weightings and relatively dense q-space sampling distributions to model white matter fiber bundles with the fiber orientation distribution function (fODF). Unlike the dODF, the fODF makes explicit assumptions about the relationship between the underlying tissue microstructure and the diffusion signal. Like the WMM and KANDO, FBI assumes that water in white matter can be divided into two non-exchanging intra- and extra-axonal pools. The water in the EAS is relatively free for diffusion mobility and the dMRI signal in this compartment decays rapidly with increased diffusion weighting. Thus, with high diffusion weighting, the dMRI signal in the IAS predominates, allowing this compartment to be characterized more effectively. FBI also explicitly assumes that D_a is constant for all axons within a given voxel and that the axons can be regarded as thin, straight cylinders. With these assumptions it can be shown that (64):

$$\zeta \equiv \frac{AWF}{\sqrt{D_a}} \approx \frac{1}{2\pi S_0 q_0^2}\sqrt{\frac{b}{\pi}}\int d\boldsymbol{q} S(\boldsymbol{q})\delta(|\boldsymbol{q}| - q_0), \qquad [49]$$

where ζ is a measurable property of the tissue microstructure q_0 is the magnitude of the q-space vector, $\boldsymbol{q}$, corresponding to the b-value, b, and δ is the Dirac delta function, indicating integration of a spherical shell in q-space, with the approximation becoming more exact for increasing b-value up to the limit that the diffusion signal becomes sensitive to the internal geometry of the IAS.

Because of the general biophysical derivation of the FBI model and the markedly distinct computational approach for approximating ζ, the FBI approach can be used as a reference to compare the DKI-based modeling techniques. In this chapter, we will compare parameters derived from both the WMM and KANDO to ζ derived from FBI in white matter regions with highly aligned white matter fiber bundles.

Methods

HARDI datasets were acquired for 2 healthy, adult volunteers ranging in age from 25 to 55, with a 3T TIM Trio MRI scanner (Siemens Medical, Erlangen, Germany) using a vendor-supplied diffusion sequence with a twice-refocused spin echo (65), 4 b-values of 0, 1000, 2000, and 5000 s/mm^2, and 128 isotropically distributed gradient directions. Acquisition parameters used were TR = 7200 ms, TE = 149 ms, voxel dimensions = 3.0 × 3.0 × 3.0 mm^3, matrix size × number of slices = 74 × 74 × 40, parallel imaging factor of 2, bandwidth = 1351 Hz/Px, and a 32 channel head coil with adaptive combine mode. A total of 20 images with no diffusion weighting (b0 images) were acquired for each subject, with a single b0 image preceding each block of 128 diffusion weighted images for each respective b-value. All b0 images were coregistered to the b0 image preceding the b = 1000 s/mm^2 images, and an average b0 image was created. In the case where the b0 image was followed by a set of diffusion weighted images, the coregistration matrix was applied to the subsequent block of diffusion weighted images. The diffusion encoding gradient vectors were updated to account for rotations of the image volume that occurred during coregistration (66).

Diffusion and kurtosis tensors were reconstructed from the b0 and b = 1000 and 2000 s/mm^2 images using diffusional kurtosis estimator (DKE) software (http://www.nitrc.org/projects/dke/)

and the WMM and KANDO parameters were estimated with in-house scripts. FBI was performed using the b0 and b = 5000 s/mm^2 images using in-house software and ζ was calculated using the a_0^0 coefficient for the spherical harmonic expansion of the diffusion signal (64). To evaluate ζ calculated with each method a white matter mask was created with FA > 0.4 to represent white matter regions with highly-aligned fiber bundles.

Results

Comparisons between each of the different methods for calculating ζ are given in Figure 9. Mean (± SD) values for ζ in the aligned white matter region (FA > 0.4) across both subjects are 0.46 (± 0.07) for FBI, 0.48 (± 0.06) for WMM, 0.54 (± 0.08) for Model 1 of KANDO, and 0.52 (± 0.08) for Model 2 of KANDO. Compared to FBI, the Pearson's product moment correlation coefficient for ζ is 0.83 for WMM, 0.62 for Model 1 of KANDO, and 0.52 for Model 2 of KANDO.

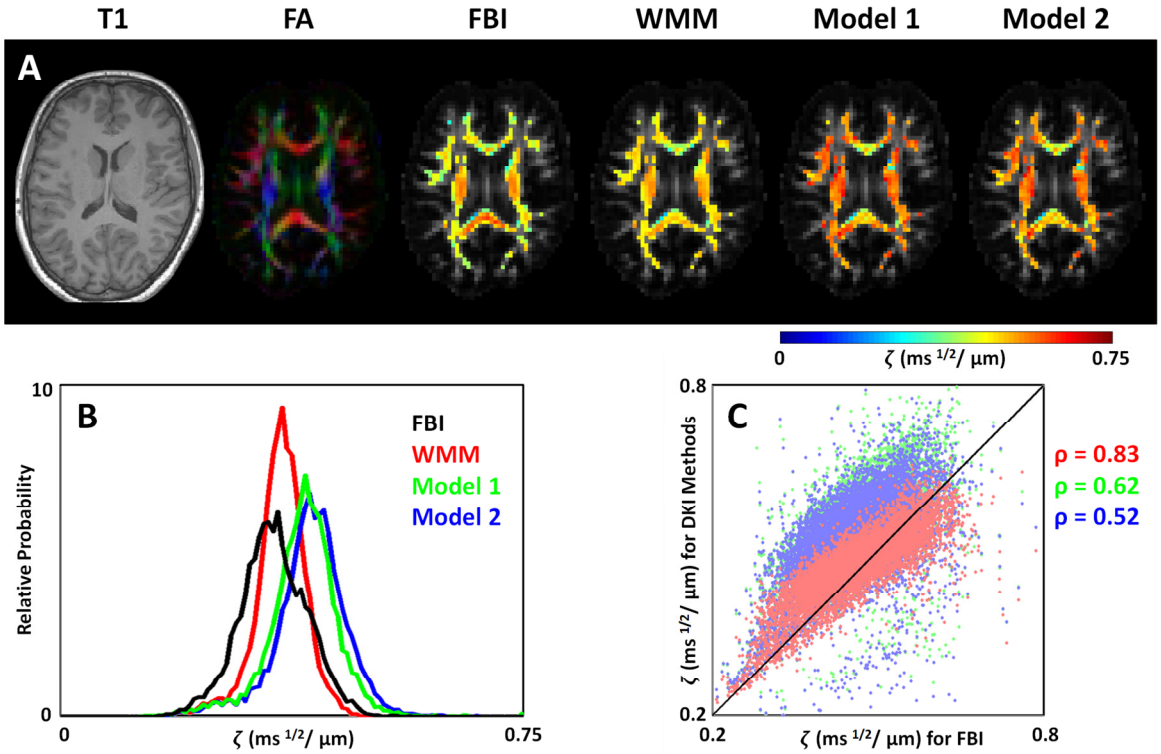

Figure 9. ζ calculations for each of the different modeling methods in regions with aligned white matter fiber bundles (FA > 0.4). (A) Representative transverse slices for a single volunteer. The T1 and FA colormap images are given for anatomical reference. FBI is used as a criterion standard to assess the DKI-based modeling methods. The WMM method agrees qualitatively with FBI, whereas the two KANDO models tend to overestimate ζ, qualitatively. (B) Distribution of ζ values demonstrates the relative probability of $\zeta$for each technique. (C) Voxel-wise correlation plots of ζ for the DKI-based techniques relative to FBI, where ρ is the Pearson's product moment correlation coefficient and the solid black line representing unity. In (B) and (C) red represents the WMM, green represents Model 1 of KANDO, and blue represents Model 2 of KANDO.

Discussion and Conclusion

DKI-based modeling techniques are promising candidates for developing biomarkers for specific biophysical properties of tissue microstructure such as AWF and D_a, which may be differentially affected by pathological mechanisms. The WMM is a straightforward algebraic method for estimating modeling parameters from DKI data and it is in remarkable agreement with FBI for

calculating ζ ($AWF/\sqrt{D_a}$) throughout regions with high FA. KANDO is a general computational framework for estimating parameters from a given model based on the measured and theoretical kurtosis tensors, which is desirable as it can, in general, accommodate distinct microstructural models, thereby accounting for a variety of complex cytoarchitectural configurations. However, the KANDO models tested in this study tend to overestimate ζ compared to FBI and demonstrate lower voxel-wise correlation with FBI compared to the WMM. Although the precise origin of this is unclear this may reflect that KANDO models are more sensitive to noise effects in estimation of the kurtosis tensor.

Microstructural modeling remains an area of active research, and holds promise for increasing the specificity of quantitative dMRI parameters to a variety distinct properties of tissue microstructure. The methods discussed in this chapter may help elucidate the complex and subtle relationships between the dMRI signal and tissue microstructure, which are of interest for the improved characterization of disease mechanisms and provide insight for a variety of pathological processes affecting the structural organization of the human brain.

4

Optimization of Kurtosis-Based White Matter Tractography

White matter tractography exploits anisotropic properties of water diffusion to reconstruct white matter pathways in the human brain. In this chapter, we will further explore properties of the kurtosis tensor which can be used to estimate the orientation of white matter fiber bundles. We will also develop efficient image analysis algorithms to help reduce the computational demands of this technique. This chapter is based on the following peer-reviewed publication:

1. **Glenn GR**, Helpern JA, Tabesh A, Jensen JH. Optimization of white matter fiber tractography with diffusional kurtosis imaging. *NMR Biomed.* 2015;28:1245-56.

The algorithms developed in this chapter have been incorporated into the DKE Tractography Module, which is freely available online and may be downloaded online at:

http://www.nitrc.org/projects/dke/

Abstract

DKI is a clinically feasible dMRI technique for white matter tractography with the ability to directly resolve intra-voxel crossing fibers by means of the kurtosis dODF. Here we expand on

previous work by exploring properties of the kurtosis dODF and their subsequent effects on white matter tractography for in vivo human data. For comparison, the results are contrasted with fiber bundle orientation estimates provided by the diffusion tensor, which is the primary quantity obtained from diffusion tensor imaging. We also outline an efficient method for performing DKI based tractography that can substantially decrease the computational requirements. The recommended method for implementing the kurtosis ODF is demonstrated to optimize the reproducibility and sensitivity of DKI for detecting crossing fibers while reducing the occurrence non-physically meaningful, negative values in the kurtosis dODF approximation. In addition, DKI-based tractography is illustrated for different protocols differing in image acquisition times from 48 to 5.3 minutes.

Introduction

The inability of DTI to directly resolve multiple white matter fiber bundle orientations has prompted the development of a number of advanced dMRI methods capable of overcoming this limitation. Underlying several of these techniques is estimation of the dODF. These methods include diffusion spectrum imaging (DSI), which exploits the Fourier relationship between diffusion data in q-space and the dODF (39,67), and Q-ball imaging (QBI), which applies the Funk transform on high angular resolution diffusion imaging (HARDI) data to estimate the dODF (37,38). These reconstruction techniques are typically best suited for dMRI acquisitions with relatively high maximum b-values and a large number of diffusion weighted images, which can limit clinical applicability (37-39,67-70). Moreover, QBI acquisitions are not optimal for estimation of the diffusion tensor or quantitative tensor-derived parameters as these primarily reflect the low b-value behavior of the dMRI signal (37,67).

DKI is an extension of DTI that estimates both the diffusion and kurtosis tensors in order to characterize non-Gaussian diffusion dynamics within complex biological tissue (29,30). Approximating the dODF from the diffusion and kurtosis tensors is one approach for resolving the orientation of crossing white matter fiber bundles, which is not possible utilizing just the diffusion tensor (32,36,71). In addition, DKI typically uses a maximum b-value of about 2000 s/mm^2 and always allows for estimation of the diffusion tensor and its associated metrics (e.g., fractional anisotropy). Consequently, DKI may be more suitable for a variety of clinical applications where scan times and quantitative, tensor-derived parameters are of interest.

The closed-form, analytic solution of the kurtosis dODF has recently been derived, facilitating its implementation for tractography (32). In previous work, radial weighting was added to the kurtosis dODF in order to enhance the accuracy and sensitivity of DKI for detecting fiber bundle orientations (32). A primary goal of this paper is to optimize the implementation of DKI-derived tractography in human brain by systematically investigating how the properties of the kurtosis dODF depend on the choice of radial weighting power. In addition, we present an efficient numerical algorithm for finding the local maxima of the kurtosis dODF, which are used to estimate the fiber directions.

Theory

The dODF for a normalized direction in space, $\boldsymbol{n}$, may be defined as in Eq. [13] by: $\psi(\boldsymbol{n}) = \frac{1}{Z}\int_0^\infty s^\alpha ds P(s\boldsymbol{n}, t)$, where $P(\boldsymbol{s}, t)$ is the diffusion displacement probability density function (dPDF) for a molecular displacement $\boldsymbol{s}$ over a diffusion time t, $s = |\boldsymbol{s}|$, α is the radial weighting power, and Z is a normalization constant.

The radial weighting power is included to increase the contribution of relatively long diffusion displacements, which may have low diffusion displacement probabilities but demonstrate a stronger dependence on the anisotropic properties of complex diffusion environments (39,67). Consequently, radial weighting can increase the resolving power for detecting directional differences. When this power is set to $\alpha = 2$, the dODF can be interpreted as the cumulative probability density for a diffusion displacement in the direction $\boldsymbol{n}$ (67). However, this is not a strict requirement for the dODF, and in general, the dODF magnitude may be interpreted as a relative degree of diffusion mobility (39). Q-ball imaging, for example, typically uses a radial weighting power of zero (37,38).

DKI assumes that the dPDF can be well described by the second and fourth order diffusion and kurtosis tensors, respectively, provided the b-value is not too large (typically with $b \leq 3000$ s/mm^2) (29,30,51,72). Consequently, a closed-form expression for evaluating Eq. [13] from DKI data, termed the kurtosis dODF, may be derived (32). The kurtosis dODF includes a correction factor, $\Lambda_\alpha(\boldsymbol{n})$, to account for the leading effects of non-Gaussian diffusion that go beyond the Gaussian dODF approximation, which is obtainable with DTI (40,73,74). Thus, the equation for the kurtosis dODF has the form:

$$\Psi_{\alpha,K}(\boldsymbol{n}) = \Lambda_\alpha(\boldsymbol{n})\, \Psi_{\alpha,G}(\boldsymbol{n}), \qquad [50]$$

where $\Psi_{\alpha,K}$ and $\Psi_{\alpha,G}$ refer to the kurtosis and Gaussian ODF approximations, respectively, and $\Lambda_\alpha(\boldsymbol{n})$ is a function of $\boldsymbol{n}$ to account for non-Gaussian diffusion, which is calculated directly

from the diffusion and kurtosis tensors and the chosen value for α. By accounting for the effects of non-Gaussian diffusion, the number of local maxima pairs in the kurtosis ODF can exceed one enabling the resolution of crossing fibers (32,36,71,75).

Because the diffusion and kurtosis tensors are symmetric, the kurtosis dODF is symmetric. Consequently, local maxima occur in pairs, which only need to be detected once over one-half of the dODF. An efficient method for evaluating $\Lambda_\alpha(\boldsymbol{n})$ and detecting local maxima pairs in the kurtosis dODF is given in the Appendix and is shown to improve image processing times over previously published methods (32,71).

Data Acquisition

DKI datasets were acquired from 5 healthy volunteers whose ages ranged from 27 to 53 y with a 3T TIM Trio MRI scanner (Siemens Medical, Erlangen, Germany) using a vendor-supplied, single-shot diffusion-weighted EPI sequence with a twice-refocused spin echo (65). All protocols were approved by the institutional review board at the Medical University of South Carolina, and informed consent was obtained from all the volunteers prior to participation in the study. All subjects underwent a primary protocol (Protocol A), and for one subject, two additional DKI datasets were acquired using a clinically oriented protocol (Protocol B) and a more time demanding research protocol (Protocol C). All protocols used 3 b-values of 0, 1000, and 2000 s/mm^2 and a 32 channel head coil with adaptive combine mode.

Protocol A consisted 3 full DKI datasets with 64 isotropically distributed gradient directions, TR/TE = 7200/103 ms, voxel dimensions = 2.5 × 2.5 × 2.5 mm^3, matrix size × number of slices = 88 × 88 × 52, parallel imaging factor of 2, and bandwidth = 1352 Hz/Px. For each subject, a total

of 25 images without diffusion weighting (b0 images) and a T1-weighted MPRAGE image with 1.0 × 1.0 × 1.0 mm^3 voxel dimensions were also acquired. The acquisition time for each independent DKI acquisition was 15.5 min, and the full DKI acquisition including 3 independent acquisitions for each diffusion-encoding vector and 25 b0 images took 48.0 min.

Protocol B used decreased scanner requirements which are more appropriate for clinical environments. This scan was performed during the same MRI session as the DKI dataset described above and acquisition parameters included 3 b-values of 0, 1000, and 2000 s/mm^2, a single b0 image, 30 isotropically distributed gradient directions, TR/TE = 5200/96 ms, voxel dimensions = 3.0 × 3.0 × 3.0 mm^3, matrix size × number of slices = 74 × 74 × 40, parallel imaging factor of 2, bandwidth = 1352 Hz/Px. The acquisition time for this protocol was 5.3 min.

Protocol C was performed with more demanding scanner settings during a second MRI session. Acquisition parameters for this scan included 3 b-values of 0, 1000, and 2000 s/mm^2, a single b0 image, 64 isotropically distributed gradient directions, TR/TE = 8400/100 ms, voxel dimensions = 2.0 × 2.0 × 2.0 mm^3, matrix size × number of slices =110 × 110 × 60, parallel imaging factor of 2, bandwidth = 1337 Hz/px. The acquisition time for this protocol was 18.1 min.

Data Analysis

All images for each subject were co-registered to the b0 image from their initial, independent DKI dataset in Protocol A using SPM8 (Wellcome Trust Center for Neuroimaging, London, UK). An average DKI dataset was then created by averaging all corresponding b0 images and DWIs from Protocol A. For each independent DKI acquisition, the gradient table was rotated to reflect

rotations of the image volume from co-registration (66). For the datasets in Protocol B and C, the affine transformation matrix from co-registration was modified to preserve rotations and translations but discard dilations and contractions in order to preserve the original voxel dimensions. All data analyses were performed on the average DKI datasets from Protocol A, with the exception of analysis of angular dispersion and reproducibility (described below), which were performed on the independent DKI acquisitions.

Tensor fitting was performed using a previously proposed constrained weighted linear least squares algorithm (52). Because our analyses included image datasets with only one b0 image, the algorithm was modified to fit directly to the signal magnitude with the log of the b0 signal intensity, $\ln(S_0)$, included as an unknown parameter to be estimated (73). Unless otherwise stated, kurtosis dODFs were evaluated with $\alpha = 4$.

Brain masks were created by performing a semi-automated, connected components analysis on the signal intensity values in the average b0 image from Protocol A for all subjects. Additional brain masks were similarly defined for the DKI datasets from protocols B and C, as these have different voxel dimensions. The diffusion tensor, the kurtosis tensor, and the kurtosis dODF were estimated throughout the brain mask prior to tractography. For comparison, orientations predicted from the Gaussian dODF were also calculated throughout the brain mask. Since these are equivalent to the principal eigenvector of the diffusion tensor (corresponding to the maximum eigenvalue) (38,74), Gaussian dODF orientation estimates were calculated directly from the diffusion tensor.

White matter masks were defined from the average DKI dataset of each subject as voxels within the brain mask with mean kurtosis (MK) values greater than 0.9. To avoid cerebrospinal fluid and reduce the influence of partial volume effects, voxels with mean diffusivity (MD) values less than 1.5 $\mu m^2/ms$ were excluded from the white matter masks. These values were selected based on the work of Falangola et al. (76). White matter masks were used to analyze properties of the kurtosis dODF and to calibrate the radial weighting parameter, as this function is intended for characterization of white matter microstructural features.

To detect the local maxima pairs of the kurtosis dODF, a spherical grid was defined using a tessellation of the icosahedron, and Eq. [[15] was evaluated in each voxel for points over one half of the surface of the spherical grid. All points of the spherical grid were then tested with their nearest neighbors to estimate local maxima. Local maxima estimates were then refined using the iterative quasi-Newton method with the Broyden-Fletcher-Goldfarb-Shanno (BFGS) algorithm (32,71,77) Our method for peak detection is described and motivated further in the Appendix. Unless otherwise stated a tessellation of the icosahedron resulting in 1281 points over one-half surface of the spherical grid was used.

Tractography was performed using the deterministic fiber assignment by continuous tracking (FACT) algorithm (78) using an FA cutoff threshold of 0.1, angle threshold of 35°, a minimum tract length of 20 mm, and 100,000 seed points randomly generated throughout the brain mask. Tractography was performed separately based on the kurtosis and Gaussian dODFs using the same seed point distributions. The effects of crossing fiber bundles on tractography are assessed visually in regions with well-known crossing fibers, such as between the corpus callosum (CC), superior longitudinal fasciculus (SLF), and the corona radiata (CR).

Conventional DKI parameter maps, such as MD, MK, and FA, were calculated from the diffusion and kurtosis tensors (52). Additional parameters, including generalized fractional anisotropy (GFA) (37,79), number of fiber directions (NFD) (32,79), and apparent tract density (TD) (80) were also calculated following optimization of the kurtosis dODF and subsequent tractography.

To test the effects of the radial weighting parameter, α, the kurtosis dODF was evaluated for 11 consecutive integer values of α between 0 and 10 from the average dataset as well as each independent DKI scan from each subject. Peak detection sensitivity was assessed by the relative probability of detecting a given value for NFD in a randomly chosen voxel, as well as the mean NFD value throughout the white matter. The influence of α on the predicted fiber bundle orientations was assessed by angular difference, which was defined as the difference in degrees between the orientation of the maximum of the Gaussian dODF, which does not depend on α, and the nearest direction detected from the kurtosis dODF. The nearest direction was chosen as opposed to the global maximum from the kurtosis dODF, as small fluctuations in the magnitude of kurtosis dODFs with multiple peaks could vary which peak was identified as the global maximum, resulting in artificially large angular difference estimates. Although angular difference quantifies the effect of accounting for non-Gaussian diffusion with the kurtosis dODF, this measure does not quantify accuracy of the orientation estimates as the true fiber bundle orientations for in vivo human data are unknown. The effects of radial weighting were also assessed qualitatively by their effects on tractography.

The angular dispersion of dODF estimates was measured to test variability in the orientations predicted across multiple independent acquisitions. To calculate angular dispersion, orientation vectors from the 3 independent scans were taken from each voxel and averaged. Angular dispersion was then defined as the average angle between each orientation vector and the average of the 3 orientation vectors. In the Gaussian dODF dataset, these orientation vectors were the principal eigenvectors from the diffusion tensor. However, in the DKI dataset each orientation vector was defined as the closest maxima pair to the principal orientation from the average dataset.

Since the dODF evaluates the radial integral of the dPDF, physically meaningful values of the dODF are non-negative, as the probability of diffusion is non-negative for all real displacements. To assess the physical plausibility of the kurtosis dODF approximations, the fraction of non-positive definite dODFs was calculated as the fraction of image voxels with at least one negative value of the kurtosis dODF. Positive definiteness was assessed with a finite sampling distribution over vertices in the pre-defined spherical grid.

All data was processed using in-house software written in MATLAB 2012a (Mathworks, Natick, MA) using the parallel computing toolbox on a personal computer with 32 GB of RAM and a 2.4 GHz, Intel Xeon 8-core processor. Our software builds off of tensor fitting algorithms provided by Diffusional Kurtosis Estimator (DKE) (http://www.nitrc.org/projects/dke/, Center for Biomedical Imaging, Medical University of South Carolina), and was written to be compatible with both DSI Studio (dsi-studio.labsolver.org, Department of Psychology, Carnegie Mellon University) and TrackVis (trackvis.org, Martinos Center for Biomedical Imaging, Massachusetts General Hospital) software. DKE was used for tensor estimation, DSI Studio was used for 3D

rendering of the kurtosis dODFs over an entire image slice, and TrackVis was used for 3D rendering the white matter fiber tracts. All other images were created using MATLAB.

Results

DKI-derived parameter maps as well as kurtosis dODFs for a transverse brain slice from a single volunteer are given in Figure 10. GFA, NFD, and TD differ from typical DKI derived parameters (e.g. MK) in that they require computation of the kurtosis dODF. In Figures 10 B and C, kurtosis dODFs with corresponding FA values below 0.1 are not shown to illustrate the applicability of the FA cutoff threshold used for tractography. Intra-voxel features from multiple fiber bundle orientations can be appreciated from the kurtosis dODF in well-known crossing fiber regions.

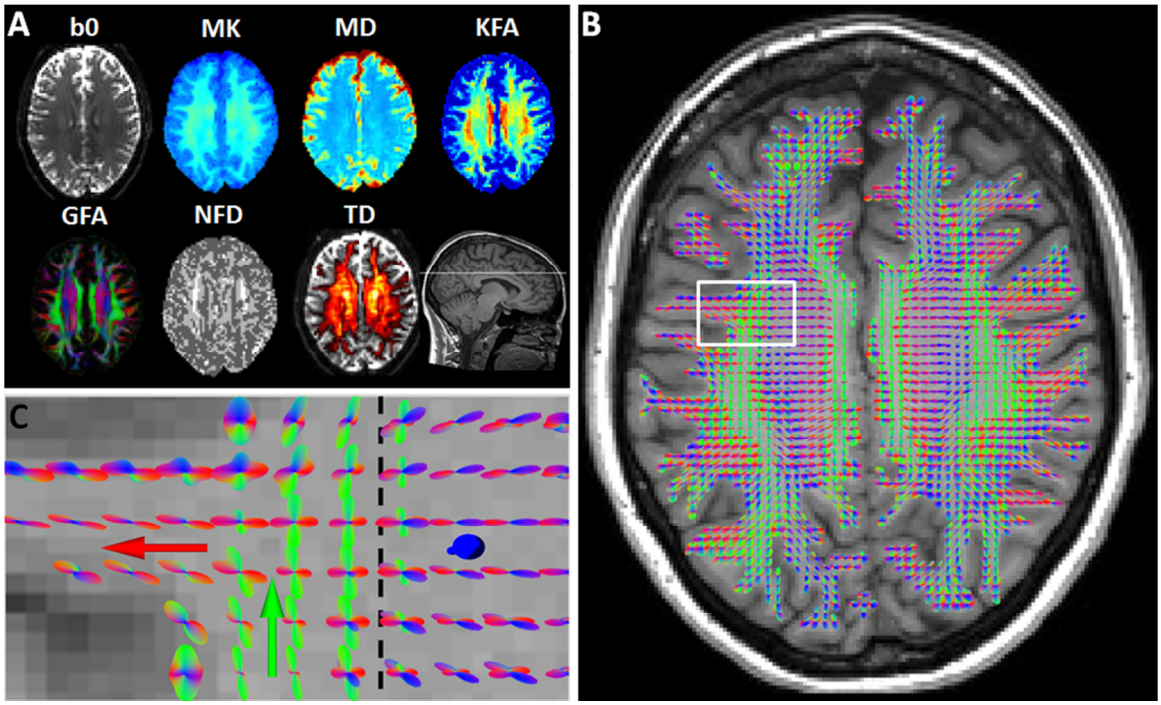

Figure 10. The kurtosis dODF. (A) A b0 image from a single transverse slice from a healthy volunteer, as well as DKI-derived parameters from the diffusion and kurtosis tensors, such as MK, MD, and kurtosis fractional anisotropy (KFA) (79) are given in the top row. The kurtosis dODF enables calculation of additional parameter maps, such as GFA, NFD, and TD, which are depicted in the bottom row. The GFA color map (4) illustrates anisotropy in the kurtosis dODF,

NFD depicts the number of local maxima pair detected from the kurtosis dODF in each voxel (32,79), and TD depicts the relative density of streamlines that pass through a given voxel with a particular tractography algorithm (80). A sagittal MPRAGE slice is also given, where the white bar indicates the location from which the parameter maps are taken. (B) 3D renderings of the kurtosis dODF overlaid on the corresponding transverse slice from the volunteer's anatomical MPRAGE image. (C) A zoomed in section from the white box in panel (B) illustrates the morphology of individual kurtosis dODFs. These kurtosis dODFs detect contributions in the diffusion environment from three well known fiber tracts; cortical projections from the CC (red arrow), the SLF (green arrow), and ascending and descending fibers in the CR (blue arrow coming out of the plane of the page). These three fiber bundles putatively overlap around the dashed black line, where 3 distinct peaks can be seen in the kurtosis dODF. The location of these fiber tracts can also be appreciated in the corresponding GFA map in panel (A).

Qualitative visualization of white matter fiber tracts are illustrated in Figure 11. The white matter tracts shown were selected with TrackVis to highlight the effect of detecting crossing fibers on the continuity of fibers detected in the SLF. The highlighted region has complex fiber bundle geometries as cortical commissural fibers from the CC pass through voxels with contributions from other fiber bundles, such as the CR and the SLF, limiting the applicability of the Gaussian diffusion approximation. The kurtosis dODF can resolve detectable features from these separate fiber bundles, which affects their visualization with white matter tractography. Streamlines estimated from the Gaussian dODF cannot resolve the orientations of multiple, distinct intra-voxel fiber bundles and are consequently more likely to fuse anatomically distinct tracts, as indicated by the white arrows in panels C and D.

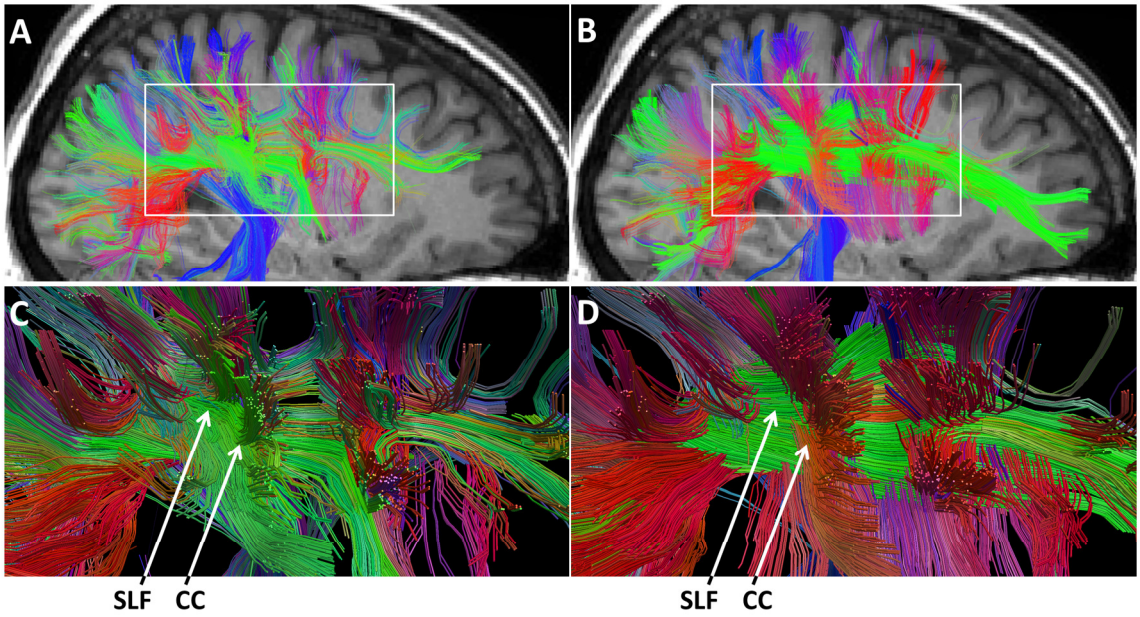

Figure 11. DKI-based tractography. (A-B) Illustrate fibers estimated from the Gaussian and kurtosis dODF, respectively overlaid on a sagittal MPRAGE image for anatomical reference. The SLF runs in the anterior–posterior direction from the temporal lobe to the frontal lobe, the CC connects the left and right cerebral hemispheres, and the CR is part of the pathway which connects the cerebral cortex with the brainstem. (C-D) Zoomed in sections from the regions depicted in the white box of panels A and B, respectively. Fiber tracts identified from the kurtosis dODF (D) show more coherent green fibers in the SLF and more red CC fibers crossing through the SLF. Fibers identified from the Gaussian dODF (C) are more disorganized. These fibers were selected to demonstrate continuity of tracts in the SLF and the effects that crossing fibers can have in complex regions such as this with multiple fiber bundle orientations. The white arrows point to regions putatively containing tracts from the CC and SLF. In Panel C, these tracts are fused together resulting in green tracts. However in Panel D, these tracts are distinct.

The effects of radial weighting are highlighted in Figures 12 and 13. In Figure 12, radial weighting sharpens the convexities of the kurtosis dODF, enhancing the resolving power for detecting multiple peaks. This has noticeable effects on the visualization of specific white matter fiber tracts. In this example, the SLF passes through voxels with non-uniform fiber bundle distributions and radial weighting of the kurtosis dODF affects the fibers identified with white matter tractography.

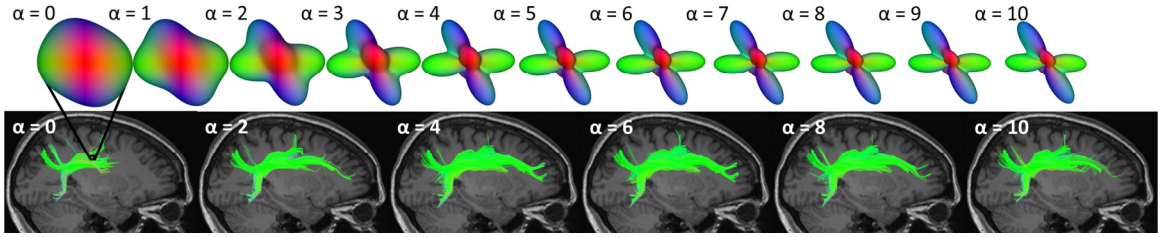

Figure 12. The effects of radial weighting for a single kurtosis dODF for integer values between 0 and 10 are given in the top row, and WHITE MATTER tracts in the SLF for even integer values between 0 and 10 are given in the bottom row. The region from which the kurtosis dODF was taken is indicated by the black box in the first image in the bottom row.

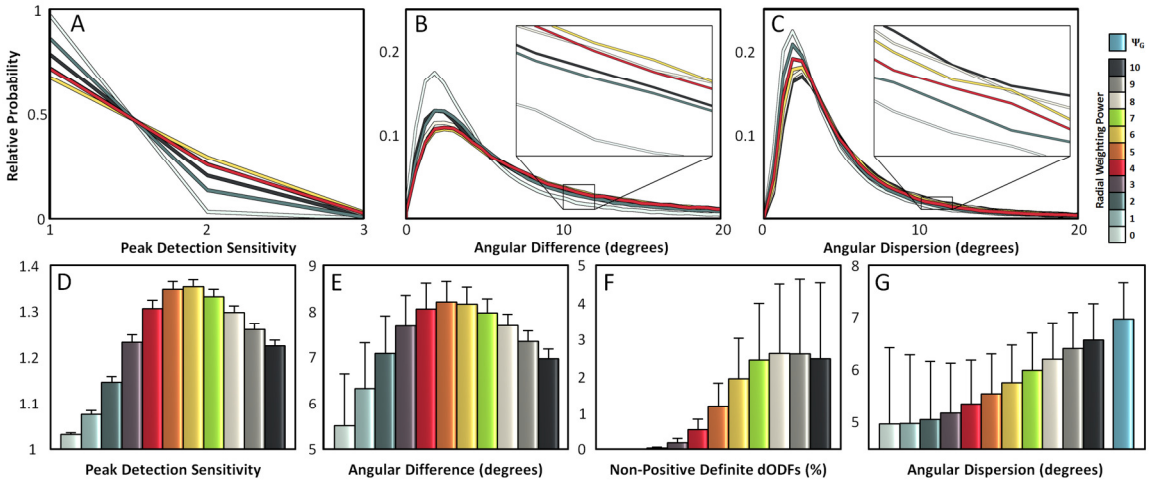

Figure 13. Effects of radial weighting on the kurtosis dODF. (A-C) Relative probability for detecting a given number of fiber directions (peak detection sensitivity), angular difference (which quantifies the effect of accounting for non-Gaussian diffusion), and angular dispersion, respectively, in a randomly chosen white matter voxel averaged across all 5 subjects for even powers of radial weighting. (D-G) Histograms for mean peak detection sensitivity, mean angular difference, mean percentage of non-positive definite dODFs, and mean angular dispersion. Mean white matter parameter estimates are calculated for each subject and then averaged across all 5 subjects. Error bars represent the standard deviation of the mean parameter estimates, across all 5 subjects and reflect inter-subject variability.

In Figure 13, properties of the kurtosis dODF as functions of the radial weighting parameter are quantified. Increasing radial weighting can increase the sensitivity of peak detection and the effects of including non-Gaussian corrections in the dODF reconstruction. However, radial

weighting also increases the variability in the principal orientation and can lead to dODFs that are not positive definite, due to the exclusion of higher-order terms from the DKI signal approximation. The peak detection sensitivity is maximized for $\alpha = 6$, as indicated by the magnitude of the bars in Figure 13 D, with a mean (± std) white matter NFD value of 1.35(±0.02) and 2 or more detected fiber directions in 32.4(±1.4)% of white matter voxels. The angular difference is maximized for $\alpha = 5$ with a mean angular difference of 8.21(±0.45) degrees throughout the white matter. Note that angular difference quantifies the effect of accounting for non-Gaussian diffusion on orientations from the kurtosis dODF and does not indicate improved accuracy as the true fiber bundle orientations is unknown for *in vivo* human data. For $\alpha = 4$, the mean percentage of white matter voxels with non-positive definite kurtosis dODFs is 0.53(±0.29)%, but for $\alpha = 5$ and higher, this percentage exceeds 1% on average. The mean angular dispersion from the kurtosis dODF increases on average with increased radial weighting; however, in all cases the angular dispersion of the kurtosis dODF is less than the angular dispersion of the Gaussian dODF. For $\alpha = 4$, the angular dispersion of the kurtosis dODF was found to be 5.37(±0.83) degrees.

Differences between the kurtosis and Gaussian dODFs are further demonstrated in Figure 14. Angular difference is elevated in regions with crossing white matter fibers (indicated by NFD > 1), suggesting accounting for non-Gaussian diffusion has the largest effect in orientation estimates in this region. The mean (± std) angular difference in crossing fiber regions across all subjects (n = 38,230 voxels) was 14.1(± 9.1) compared to 5.6(± 4.3) in regions where only a single fiber bundle was detected (n = 97,716 voxels). Similarly, the mean (± std) angular dispersion for the Gaussian/kurtosis dODFs was 11.6(± 12.5) / 6.2(± 7.1) in crossing fiber regions and 5.2(± 4.9) / 5.0(± 4.7) when only a single fiber bundle orientation was predicted. In Figure 14

E, angular dispersion in the kurtosis dODF is plotted as a function of the radial weighting power in both the single and crossing fiber bundle regions, and these two populations show differing trends. When only one fiber bundle distribution is present, radial weighting increases angular dispersion, but when multiple fiber bundles orientations are present, angular dispersion is minimized for α = 3 or α = 4.

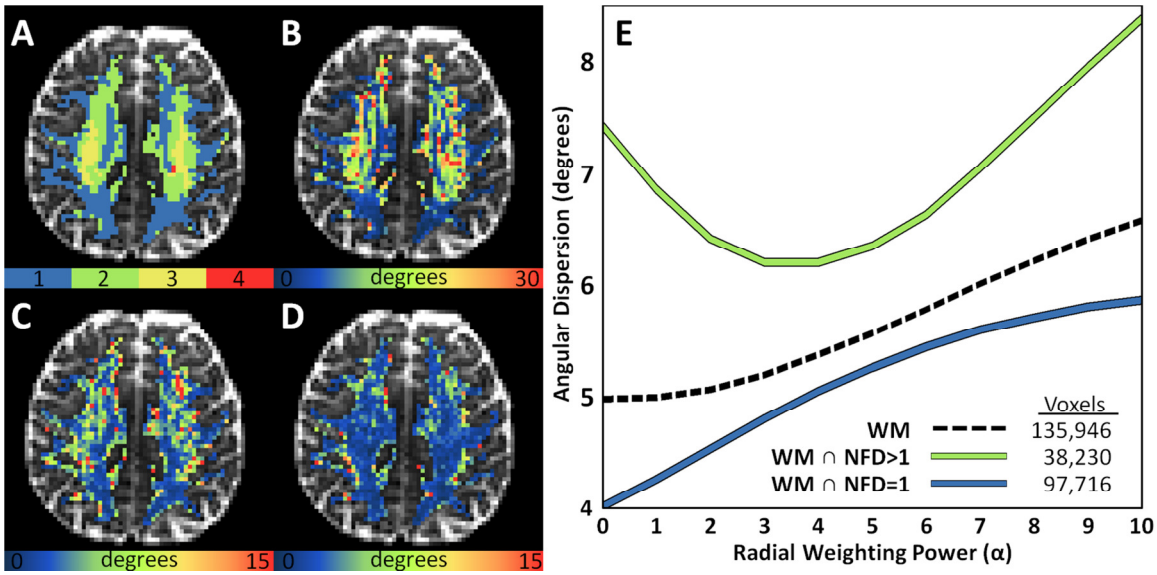

Figure 14. Properties of the kurtosis and Gaussian dODFs are influenced by the underlying fiber bundle geometries. (A) NFD map for a single transverse slice illustrates regions where multiple fiber bundle directions are detected (NFD > 1). (B) Angular difference is increased in regions with crossing fibers, suggesting accounting for non-Gaussian diffusion has the greatest effect in these regions. (C-D) Angular dispersion in the Gaussian and kurtosis dODFs, respectively, quantifies the variation of the predicted orientations from 3 independent acquisitions. Angular dispersion for the Gaussian dODF is increased in regions where multiple fiber directions are detected, but it is significantly less affected by the number of fiber directions in the kurtosis dODF. (E) The effects of radial weighting on angular dispersion in the kurtosis dODF are influenced by the underlying fiber geometry. When only one fiber bundle distribution is present (blue) angular dispersion is relatively small, but increases gradually with α. Angular dispersion is increased with more complex fiber distributions (green), but is minimized with a moderate amount of radial weighting (up to about α = 4).

Reproducibility of DKI based tractography is illustrated in Figure 15. The voxel dimensions and scan times differed substantially between the different protocols, but fibers identified with

DKI-based white matter tractography demonstrate good qualitative consistency. However, the TD images show regions with distinct tract density concentrations in the higher resolution scans, suggesting that the streamlines fill the brain volume with slightly different trajectories, although the overall trends are similar.

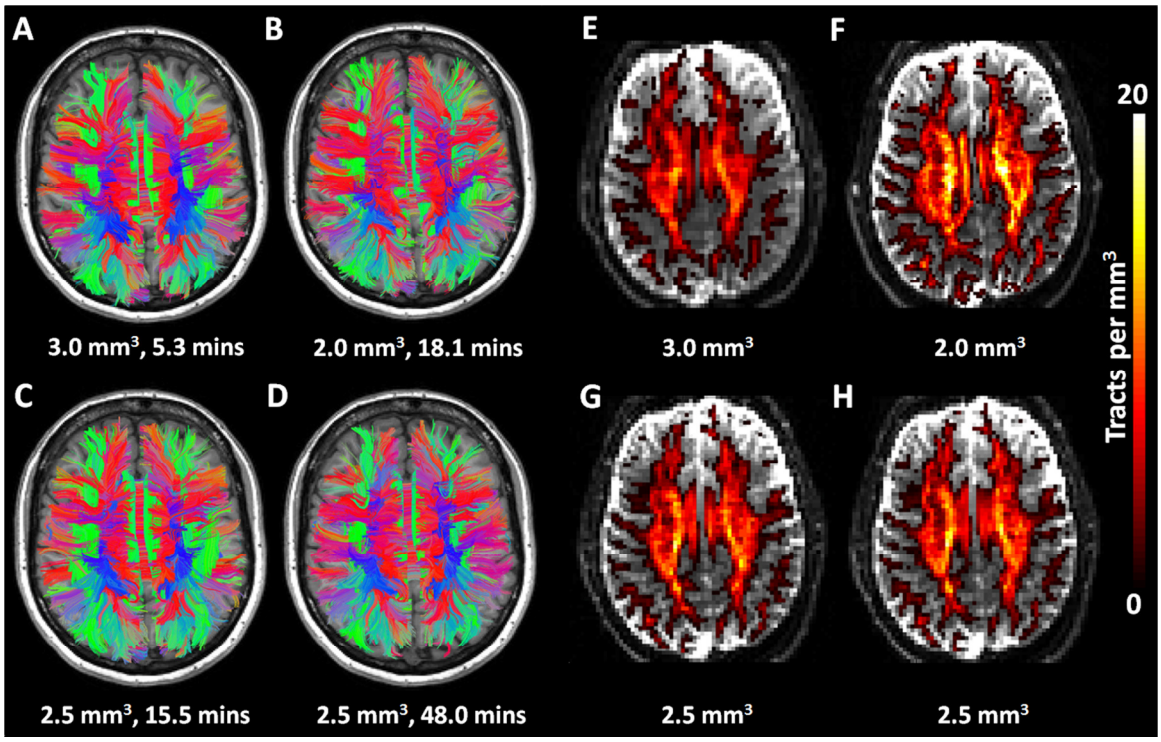

Figure 15. Reproducibility of the DKI-based white matter tractography across different acquisition schemes. (A-D) white matter fiber tracts identified from DKI acquisitions with voxel dimensions ranging from 3.0 × 3.0 × 3.0 mm^3 to 2.0 × 2.0 × 2.0 mm^3 and scan times ranging from 5.5 to 48.0 minutes. All fiber tracts shown pass through the transverse brain slice given, with (E-H) corresponding TD images for the same slice. TD images quantify the density of tracts passing through each voxel for a given tractography algorithm. In each case tractography was performed from 100,000 seed points, randomly generated within the brain mask. Protocol A was used for C,D,G, and H, Protocol B was used for A and E, and Protocol C was used for B and F.

Discussion

The kurtosis dODF provides a convenient framework for performing DKI-based tractography from standard DKI datasets. By directly resolving the orientations of intra-voxel, crossing white matter fiber bundles, the kurtosis dODF improves upon Gaussian-based methods for tractography. The kurtosis dODF shows high reproducibility across independent scans, as well as good qualitative consistency from different acquisition schemes. We chose to use 60 isotropically-distributed gradient directions and relatively high resolution for our primary analyses because we were primarily interested in image quality rather than scan time for these experiments. However, the DKI-based tractography results from the scan with lower resolution and only 30 gradient directions are quite comparable and more applicable to a clinical environment, where scan time is a major concern. This suggests that DKI-based tractography can be performed with many existing datasets having similar acquisition protocols.

In addition to the dODF a separate class of model-dependent functions termed fiber orientation distribution functions (fODFs) can be used to model the orientations of fiber bundles from dMRI data (81). A common fODF reconstruction technique is spherical deconvolution, which assumes the diffusion signal over a spherical shell in q-space can be represented by the convolution of the fODF and a single fiber bundle response function, which is estimated from DW images (DWIs) with the highest FA values (82). The fODF and dODF differ in that the fODF presumes a specific model of white matter microstructure whereas the dODF is based on model-free, or general properties of diffusion dynamics. Consequently, fODF measures may have improved peak detection sensitivity and resolving power for detecting directional differences. However, fODF measures suffer from their own limitations, including the accuracy of the model used to describe in vivo properties of neural tissue in normal and diseased states. Spherical deconvolution is also typically best suited for relatively high diffusion weighting b-values (i.e.

3000 s/mm^2) (82). However, constrained (or super-constrained) spherical deconvolution (CSD) can resolve crossing fibers at relatively low b-value (e.g. b = 1000 s/mm^2) (77,83,84), and it has recently been shown to improve fiber detection rate and minimize orientation estimation errors relative to other advanced diffusion techniques (such as QBI) in simulated dMRI data with b = 1000 s/mm^2 (85). A related technique, termed diffusion deconvolution, can be applied to estimate the fODF from dODF reconstructions to improve the angular resolution (86). However, fODF measures have not yet been investigated in relation to DKI data or the kurtosis dODF.

In the analysis of the kurtosis dODF, the radial weighting power is an important parameter to be optimized as it affects orientations predicted from the kurtosis dODF, thereby impacting DKI-based tractography. Beyond $\alpha = 6$, the benefits from radial weighting diminish, which can be appreciated by the decrease in the mean peak sensitivity in Figure 13 as well as the reduction in fibers identified in the SLF in Figure 12, which is in agreement with the simulations provided by Jensen et al. (32). The negative effects of radial weighting increase gradually, including an increase in the percentage of non-positive definite dODFs (an indicator that the kurtosis approximation is failing) and an increase in the angular dispersion of the orientations predicted, which is likely due to the approximate nature of the kurtosis dODF and the effects of signal noise on estimation of the diffusion and kurtosis tensors. Thus in Figure 12, the number of fibers identified in the SLF increases up to about $\alpha = 6$ as radial weighting increases peak detection sensitivity, but begins to diminish with further radial weighting as the kurtosis dODF approximation becomes less reliable.

We chose $\alpha = 4$ for our analyses, because it provides a good balance between increasing peak detection sensitivity, increasing the effects of accounting for non-Gaussian diffusion, and

minimizing the negative consequences of too strong radial weighting, such as increasing variability in the principal orientation vector and the occurrence of non-positive definite ODFs. This choice of radial weighting also minimizes the dispersion in the orientation estimates when multiple fiber bundles are detected (Figure 14 E), which may be beneficial for tractography when streamlines pass through complex white matter regions. This is the first time angular dispersion measures in the kurtosis dODF have been quantified. Moreover, this is the first time the negative consequences of too strong radial weighting in the kurtosis dODF have been reported for real human data.

When $\alpha = 4$, the kurtosis dODF estimates approximately 28.2% of white matter voxels contain multiple fiber bundle orientations. This is significantly less than the value of >90% reported by Jeurissen et al. using CSD (77). Although both methods can resolve distinct orientations from intra-voxel crossing fibers (cf. Figure 10 C in this chapter and Figure 5 B in Jeurissen et al. (77)), CSD is more sensitive at detecting fiber bundle orientations than DKI, owing in part, to the strong assumptions employed in modeling white matter by the fODF measures.

Averaging the co-registered DWIs to form an average DKI dataset is a possible limitation of our study design, as each DWI has slightly different contrast owing to rotations of the image volume to account for subject motion that accumulates over the duration of the scan. Correcting for rotation of the image volume is necessary to account for changes to the image coordinate system that occur when selecting the field of view or correcting for subject motion (66), which may lead to small errors in angle estimates when the signals are averaged. However, the average angle of rotation from the affine transformation matrices applied during image co-registration in

this study was calculated to be only 0.85 degrees. Thus, corrections for subject motion were minimal, and we do not expect this to be a confounding factor in our analyses. An additional approach would be to combine all co-registered DWIs independently in the tensor estimation to form a reference dataset. Although this approach may have some advantages in keeping signals with slightly different diffusion contrast separate, this was not explored here for continuity with previous work (32). In addition, although correction for subject motion was small, subject motion may still contribute to some variability that occurs in the kurtosis dODF orientation estimates from co-registration errors. Thus, orientation dispersion estimates from repeated scans may overestimate the pure random error in the measurement techniques. Nevertheless, the values reported here provide a reasonable estimate for the intrinsic variability that occurs in kurtosis dODF measures for real human data.

In this chapter, we have demonstrated that a radial weighting power of $\alpha = 4$ is a reasonable choice for performing the kurtosis dODF reconstruction for in vivo human scans. From the data presented in Figure 5, when $\alpha = 4$, crossing fibers are detected in 28.2(±1.56)% of white matter voxels, the average NFD was 1.31(±0.02), the average angular difference was 8.06(±0.56) relative to the Gaussian orientation estimates, the average angular dispersion was 5.37(±0.83) for kurtosis dODF estimates, and 0.53(±0.29)% of voxels had at least one non-physically meaningful negative value. The radial weighting power of $\alpha = 4$ is also shown to minimize angular dispersion estimates in crossing fiber regions, with a mean angular dispersion of 6.20(±0.82) degrees. The angular difference relative to the Gaussian dODF in crossing fiber regions increases to 14.2(±0.31) degrees, supporting the notion that accounting for non-Gaussian diffusion has the largest effect in these regions. This choice for radial weighting is in agreement with previous work from Jensen et al., where α was shown to influence angular accuracy in simulated data (32).

In addition, we have demonstrated that DKI-based tractography can be performed on DKI datasets with significantly different acquisition parameters ranging in voxel dimensions from 2.0 × 2.0 × 2.0 mm^3 to 3.0 × 3.0 × 3.0 mm^3, TR from 5.2 to 8.4 s, TE from 96 to 103 ms, and acquisition times from 5.3 to 48.0 mins. These results agree with those of Henriques et al. (71), who found the performance of the kurtosis dODF to be stable across different acquisition settings by varying the number of b-values tested (71). This suggests that the kurtosis dODF and subsequent DKI-based tractography may be less sensitive to protocol acquisition settings than other techniques, which is also in agreement with previous work by Veraart et al. (87), suggesting DKI-derived tensor parameters are relatively stable to changes in acquisition parameters. The stability of the DKI-dODF may, in part, be due to the unique method used to reconstruct the kurtosis dODF from the diffusion and kurtosis tensors as opposed to applying integral transforms on q-space data, where angular resolution, for example, does depend on the q-space sampling density and the b-values used (37,39). However we do find some differences in the TD images resulting from DKI data with different acquisition settings, suggesting that the voxel dimensions used does affect the trajectory of streamlines through the image volume. Note that biological interpretation of TD is problematic (81). Here, TD is not intended to reflect or infer the actual density of axonal projections but rather to highlight similarities and differences in DKI-based tractography from differing protocols.

In the Appendix, novel tensor-derived coefficients are provided that remove redundancy from evaluations of the kurtosis dODF in order to improve computational efficiency and a peak detection routine is proposed to further reduce the computation demands. The proposed method

provides a practical technique for performing DKI-based tractography from standard DKI datasets.

Conclusion

DKI is a clinically-feasible dMRI technique which shows promise for tractography due to its ability to directly resolve crossing fibers with the kurtosis dODF. Here, we consider properties of the kurtosis dODF for in vivo human data, including quantification of positive and negative effects of varying degrees of radial weighting, reproducibility of DKI derived tractography across different acquisition schemes, and strategies for reducing the image processing times for detecting peaks from the kurtosis dODF. By accounting for non-Gaussian diffusion, the kurtosis dODF can significantly enhance tractography when compared to Gaussian-based methods. The proposed method for analyzing the kurtosis dODF provides an efficient and effective method for performing tractography with DKI. Since the kurtosis dODF can be reliably calculated from standard DKI data, DKI-based tractography may be applied to pre-existing DKI datasets for retrospective studies.

Appendix: Numerical evaluation of the kurtosis dODF

The Gaussian dODF approximation depends solely on the diffusion tensor and the degree of radial weighting and may be given by Eq. [14].

The leading non-Gaussian correction factor for the Gaussian dODF approximation in Eq. [50], $\Lambda_\alpha(\hat{\boldsymbol{n}})$, is given by (32):

$$\Lambda_\alpha(\boldsymbol{n}) = 1 + \frac{1}{24}\sum_{ijkl}\left[3U_{ij}W_{ijkl}U_{kl} - 6(\alpha+1)U_{ij}W_{ijkl}V_{kl} + (\alpha+1)(\alpha+3)V_{ij}W_{ijkl}V_{kl}\right]. \quad [51]$$

To evaluate the kurtosis dODF and estimate local maxima pairs, Eq. [51] must be evaluated numerous times for each image voxel (more than 1281 evaluations for our protocol, as Eq. [51] must be evaluated at each vertex in the sampling distribution followed by iterative, non-linear optimization). This is a computationally intensive problem resulting from repeated tensor calculations and the non-linearity of Eq. [51], which can result in substantial image processing times when evaluated over an entire image volume. As a result, removing all redundancy in evaluation of $\Lambda_\alpha(\boldsymbol{n})$ can result in a significant decrease in image processing times. This can be accomplished with a single-pass coefficient calculation for all components that depend only on $\boldsymbol{D}$, $\boldsymbol{W}$, and α, and are thus independent of the sampling direction, $\boldsymbol{n}$, which is varied in the sampling distribution.

To accomplish this, we can break apart each term in Eq. [51] and calculate coefficients which do not depend on the orientation being varied, $\boldsymbol{n}$. The first term can be defined as

$$A = \sum_{i,j,k,l} 3U_{ij}W_{ijkl}U_{kl}. \qquad [52]$$

Then, let $P_2(i_1, i_2)$ be the set of all permutations of the indices $\{i_1, i_2\}$ and $P_4(i_1, i_2, i_3, i_4)$ be the set of all permutations of the indices $\{i_1, i_2, i_3, i_4\}$, and define

$$B_{i_1,i_2} = \sum_{i,j,k,l} -6(\alpha + 1)U_{ij}W_{ijkl} \cdot \sum_{I \epsilon P_2(i_1,i_2)} U_{k,I_1}U_{l,I_2}, \qquad [53]$$

and

$$C_{i_1,i_2,i_3,i_4} = \sum_{i,j,k,l}(\alpha+1)(\alpha+3)W_{ijkl} \cdot \sum_{I \epsilon P_4(i_1,i_2,i_3,i_4)} U_{i,I_1}U_{j,I_2}U_{k,I_3}U_{l,I_4}. \qquad [54]$$

After calculating all of the scalar coefficients for a given image voxel,

$$\begin{aligned}
&\psi_{\alpha,K}(\boldsymbol{n}) = \left(\frac{1}{\boldsymbol{n}^T\boldsymbol{U}\boldsymbol{n}}\right)^{(\alpha+1)/2}\Big\{1 + \\
&\frac{1}{24}\Big[A + (B_{11}n_1^2 + B_{22}n_2^2 + B_{33}n_3^2 + B_{12}n_1n_2 + B_{13}n_1n_3 + B_{23}n_2n_3)/(n'Un) + \\
&(C_{1111}n_1^4 + C_{1112}n_1^3n_2 + C_{1113}n_1^3n_3 + C_{1122}n_1^2n_2^2 + C_{1123}n_1^2n_2n_3 + C_{1133}n_1^2n_3^2 + \\
&C_{1222}n_1n_2^3 + C_{1223}n_1n_2^2n_3 + C_{1233}n_1n_2n_3^2 + C_{1333}n_1n_3^3 + C_{2222}n_2^4 + C_{2223}n_2^3n_3 + \\
&C_{2233}n_2^2n_3^2 + C_{2333}n_2n_3^3 + C_{3333}n_3^4)/\left(\boldsymbol{n}^T\boldsymbol{U}\boldsymbol{n}\right)^2\Big]\Big\},
\end{aligned} \qquad [55]$$

which can be evaluated approximately 81 times faster than its equivalent formulation given above due to the absence of redundant calculations and nested for loops. When incorporating Eqs. [52-54] into a script for coefficient calculation, the nested for loops can be eliminated all together by expanding the summations and writing each term in the equations explicitly.

Appendix: Detection of local maxima

Because the kurtosis dODF is a continuously differentiable function the quasi-Newton method with the BFGS algorithm for peak estimation is used (32,71,77), as it utilizes both the function and its first-order partial derivatives. However, non-linear optimization of the kurtosis dODF is computationally intensive. So to limit the number of times non-linear optimization is invoked and minimize image processing time, we first performed brute force peak estimation over a pre-defined sampling distribution and then apply the quasi-Newton method to refine peak estimates.

Undersampling the kurtosis dODF decreases the sensitivity of peak detection and oversampling increases processing time. By only invoking the non-linear step from a few seed points which are relatively close to the precise local-maximum, this method suffers from lower peak-detection sensitivity but can dramatically decrease the computational time. The pre-defined sampling distribution is also used to calculate GFA. As a result, it provides a convenient framework for analyzing the kurtosis dODF.

Evaluating the kurtosis dODF over the entire brain for each dataset with $2.5 \times 2.5 \times 2.5$ mm^3 voxel dimensions (including the all radial weighting powers in the average and independent DKI datasets) throughout the brain mask took 32.3 ± 2.3 minutes using MATLAB's parallel computing toolbox on a personal computer with 32 GB of RAM and a 2.4 GHz, Intel Xeon 8-core processor.

Our method for choosing a sampling distribution is illustrated in Figure and Table 1. To generate a relatively evenly spaced sampling distribution over the domain of the kurtosis dODF function, we performed a tessellation of the icosahedron by iteratively quadrisecting each face and projecting the new vertices onto the surface of the unit sphere, which generates $\mathrm{V_n} = V_{n-1} + 4^{n-1} \times 30$ vertices, where n is the number of iterations, and $V_0 = 12$ are the number of vertices of an icosohedron. In addition to generating relatively evenly spaced points, this method has the added benefits that the vertices occur on a well-defined geometrical surface, which facilitates estimating candidate local maxima, as each vertex can readily be tested against its nearest neighbors to determine if it is the local maximum of its neighborhood. After local maxima are estimated, the candidate points are used as seed points for the quasi-Newton method to iteratively refine the peak estimates and precisely identify the peaks. This differs from previously published

methods which use electrostatic repulsion (ESR) to define a sampling distribution and then uses all of the sampling distribution vertices as seed points for non-linear optimization (32,71,77). For comparison with previous methods (32,71), we also generated a sampling distribution with 100 points distributed over one half surface of the spherical grid using an ESR algorithm (88).

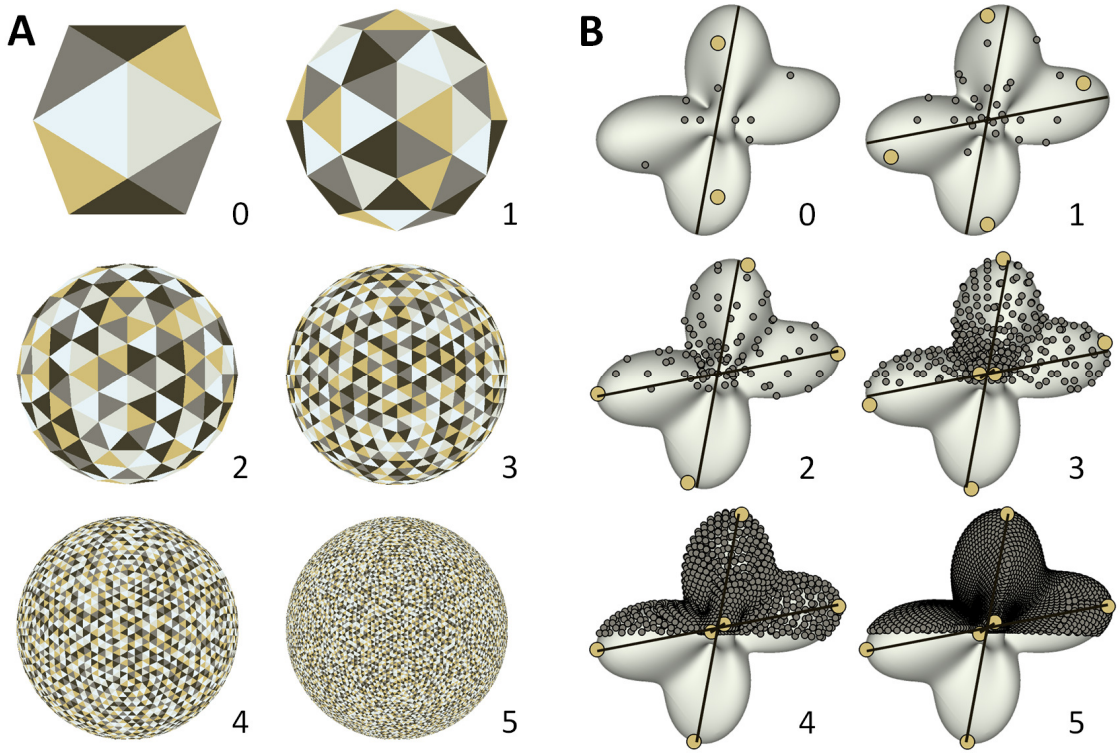

Figure 16. The kurtosis dODF sampling distribution. (A) Experimental sampling distributions were defined by iteratively quadrisecting the faces of an icosohedron, where the number in the bottom right indicates the number of iterations used, and vertices over one half of the distribution were used to identify local maxima pairs. (B) The vertices of the quadrisected icosahedron are then projected onto the surface of kurtosis dODF using Eq. [55] (small dark gray spheres). Each vertex is then tested against its nearest neighbors (connected by an edge) and candidate local maxima identified by having the largest value in their neighborhood (large gold spheres). The corresponding vertex in the sampling distribution is then used to seed the non-linear optimization algorithm to precisely identify the local maxima of the kurtosis dODF (brown lines).

Table 1. Summary Statistics for Sampling Distributions

SD	n	$\bar{\theta}$	Crossing Fibers (% voxels)	Missed Peaks (%)	NFD	GFA	Fiber Count (k)	Processing Time (min)
0	6	63.4(0.0)	0 (0)	23.8(1.1)	1.0(0.0)	0.4(0.0)	43.8(1.8)	4.9(0.52)
1	21	33.9(2.2)	17.3(0.9)	10.2(0.9)	1.2(0.0)	0.5(0.0)	54.8(2.3)	5.2(0.40)
2	81	17.2(1.1)	25.0(1.3)	3.5(0.4)	1.3(0.0)	0.5(0.0)	60.3(2.3)	6.7(0.43)
3	321	8.6(0.6)	27.5(1.5)	1.3(0.2)	1.3(0.0)	0.5(0.0)	62.4(2.2)	11.3(0.83)
4	1281	4.3(0.3)	28.2(1.6)	0.6(0.1)	1.3(0.0)	0.5(0.0)	63.1(2.4)	29.4(2.14)
5	5121	2.2(0.1)	28.4(1.6)	0.4(0.0)	1.3(0.0)	0.5(0.0)	63.3(2.4)	100.1(7.21)
ESR	100	14.8(1.1)	28.9(1.6)	——	1.3(0.0)	0.5(0.0)	63.6(2.5)	402.5(30.15)

Note: SD is sampling distribution. Values represent the mean (± standard deviation) for each measure in the white matter ROI, pooled from all 5 subjects. Values were calculated from the average DKI scan with α = 4. With the ESR-derived sampling distribution, iterative non-linear optimization was performed for each vertex (n). However, for all other sampling distributions, non-linear optimization was only performed on a small subset of the vertices, which reflect local maxima estimates obtained over the spherical grid

In Table 1, summary statistics are given for each a sampling distribution used in analysis of the kurtosis dODF with $\alpha = 4$, where SD defines the sampling distribution (numbers represent the number of iterations used for iterative quadrisection of the icosahedron and ESR denotes the previously published peak detection routine) (32,71), n is the number of vertices in the sampling distribution, $\bar{\theta}$ is the average separation angle between each point and its surrounding neighbors, crossing fibers represents the percentage of voxels with NFD > 1, missed peaks represents the percentage of orientation estimates missed using the previously published method as a reference, NFD is the average NFD throughout the white matter, GFA is the average value for GFA throughout the white matter, fiber count is the number of fibers (in thousands) identified by tractography from 100,000 seed points, and processing time is the total amount of time in minutes required for estimation of the kurtosis dODF orientations from DKI data, including tensor estimation and evaluation of the kurtosis dODF for peak detection. Increasing the sampling density increases the number of crossing fibers regions as well as white matter fiber tracts

identified but has minimal effects on mean GFA estimates after the second iteration. From SD 3 to 4 there is a small increase in the number of peaks and fibers detected and a decrease in the number of missed peaks. However, image processing time increases from 11.3 to 29.4 minutes. We chose SD 4 as opposed to 5 as the incremental improvement in peak sensitivity was not worth the significant increase in image processing time (from 29.4 to 100.1 minutes per dataset) for our primary analyses (with 220 image datasets). However, the sampling distribution defined with 3 iterations also offers good performance when decreasing image processing time further is a major concern. The previously published ESR method does have the highest peak detection sensitivity but at the expense of substantially longer image processing times. Image processing times presented include constrained weighted linear least squares estimation and depend on our specific implementation, which was performed in MATLAB. However, similar improvements in image processing times can be expected on other platforms, as this reflects the computational efficiency.

5

Mapping the Orientation of White Matter Fiber Bundles

DKI is a promising method for tractography owing to its ability to directly resolve crossing white matter fiber bundles with the kurtosis dODF. In this chapter, we will compare the orientations estimated from the kurtosis-dODF approximation to the full dODF reconstructed via diffusion spectrum imaging (DSI). This chapter is based on the following peer-reviewed publication:

1. **Glenn GR**, Kuo LW, Chao YP, Lee CY, Helpern JA, Jensen JH. Mapping the orientation of white matter fiber bundles: A comparative study of diffusion tensor imaging, diffusional kurtosis imaging, and diffusion spectrum imaging. AJNR Am. J. Neuroradiol. 2016:[Epub ahead of print].

Abstract

White matter tractography relies on fiber bundle orientation estimates from dMRI. However, clinically feasible techniques such as DTI and DKI utilize assumptions, which may introduce error into *in vivo* orientation estimates. In this study, fiber bundle orientations from DTI and DKI are compared to DSI as a gold standard to assess the performance of each technique. For each

subject, full DTI, DKI, and DSI datasets were acquired during 2 independent sessions, and fiber bundle orientations were estimated using the specific theoretical assumptions of each technique. Angular variability and angular error measures were assessed by comparing the orientation estimates. Tractography generated with each of the three reconstructions was also examined and contrasted. Orientation estimates from all three techniques had comparable angular reproducibility, but DKI decreased angular error throughout the white matter compared to DTI. DSI and DKI enabled the detection of crossing fiber bundles, which had pronounced effects on tractography relative to DTI. DSI had the highest sensitivity for detecting crossing fibers; however, the DSI and DKI tracts were qualitatively comparable. Fiber bundle orientation estimates from DKI were found to have less systematic error than those from DTI, which can have notable effects on tractography. However, tractography obtained with DKI is qualitatively comparable to that of DSI. Since DKI has a shorter typical scan time than DSI, DKI is potentially more suitable for a variety of clinical applications.

Introduction

White matter tractography is used clinically to visualize functionally important white matter tracts and aid neurosurgeons during pre-surgical planning (89,90). Tractography is also an important research tool for studying structural connectivity, as tractography is currently the only non-invasive technique for mapping *in vivo* anatomical neural connections in the human brain (36). However, tractography relies on fiber bundle orientation estimates derived from particular dMRI techniques, which may suffer from inherent methodological limitations, potentially resulting in clinically misleading information (91,92).

Of the several proposed dMRI methods for estimating the orientation of white matter fiber bundles, a common approach utilizes the dODF, which quantifies the relative degree of diffusion mobility along a given direction from physical properties of water diffusion (37-39,67). Diffusion of water is assumed to be least restricted parallel to the orientation of white matter fiber bundles resulting in local maxima of the dODF.

There are several distinct techniques for reconstructing the dODF from dMRI data that differ in their theoretical assumptions and optimal experimental implementation. These include DTI which assumes the diffusion of water can be completely described by Gaussian (normal) diffusion (40,73,74); diffusional kurtosis imaging (DKI), which extends the DTI model to account for non-Gaussian diffusion effects (29,30,32,33); q-ball imaging, which applies the Funk transformation to dMRI data from high angular resolution diffusion-weighted imaging (37,38), and diffusion spectrum imaging (DSI) (39,67).

In contrast to other methods, DSI quantifies the dODF by employing an exact (in the narrow gradient pulse limit) Fourier transform relationship between the dMRI signal and the dPDF. To accomplish this requires a dense sampling of q-space with relatively high maximum b-values. In this way, DSI effectively characterizes complex intra-voxel microarchitecture without the need for intricate tissue models or ancillary approximations, although it tends to have more demanding data acquisition requirements than alternative methods. Due to its rigorous mathematical formulation and comprehensive description of intra-voxel diffusion dynamics, DSI may be considered a reference standard for validating of other dODF techniques for *in vivo* experiments (93). Nonetheless, it should be appreciated that even the exact dODF may not give the precise

orientation of white matter fiber bundles, reflecting the complex and subtle relationship between diffusion and microstructure.

The DTI dODF contains the same information as the diffusion ellipsoid, and the global maximum of the DTI dODF gives the same direction as the principal eigenvector of the diffusion tensor (32,37). Although efficient in terms of image acquisition time, DTI is not capable of directly resolving intra-voxel fiber crossings (40,73,74), which can lead to significant errors in orientation estimates from regions with complex tissue architecture (77,91).

The motivation for considering the kurtosis dODF is twofold. First, there have been a significant number of prior studies employing DKI to investigate neuropathology, including stroke (59,94-97), Alzheimer's disease (55,56,98-100), cancer (101-103), and numerous others (75). Therefore, a tractography method that is compatible with DKI can be of value. Second, DKI shares some of the practical advantages of DTI that make it particularly attractive for clinical settings, such as small maximum b-values and protocol options with relatively short scan times (30,59,104). For example, in clinical settings, a whole-brain DKI dataset with reasonable image quality may be acquired in approximately 7 minutes (59) and good quality whole-brain DKI tractography has been demonstrated with acquisition times as short as 5.3 minutes (104). Moreover, DKI inherently provides measures of the diffusion and kurtosis tensors, as well as all tensor-derived quantitative measures (e.g., fractional anisotropy and mean kurtosis), which are of interest for characterizing tissue microstructure (52).

In this study, dODFs derived from DSI, DKI, and DTI from *in vivo* human measurements are directly compared, particularly with regard to their fiber bundle orientation estimates. The errors

intrinsic to the dODF orientations from DTI and DKI are calculated using the DSI orientations as benchmarks. In addition, the intra-subject variabilities of dODF orientation estimates are calculated across independent sessions for all three methods. A primary goal of this study is to assess the degree to which the DKI dODF approximates the DSI dODF and improves upon the DTI dODF. Tractography results are also compared qualitatively for the three dODF reconstruction techniques.

Methods

The study was approved by the institutional review board at the National Health Research Institutes (Taiwan), and informed consent was obtained from all participants prior to enrollment in the study. All imaging experiments were performed on a 3T MRI system with a maximum gradient strength of 45 mT/m and a maximum single direction slew rate of 200 mT/m/ms (Tim Trio, Siemens, Erlangen, Germany), using a twice-refocused balanced spin-echo diffusion echo-planer imaging pulse sequence (65) with fat suppression. Each session included independent DSI and DKI acquisitions, with the DTI data being taken as a subset of the DKI acquisition. To quantify variability for each dMRI method, each volunteer was scanned during two separate sessions, resulting in a total of 6 complete DSI and DKI datasets. The dMRI protocols were optimized to maximize the SNR rather than minimize the acquisition times in order to facilitate the assessment of the accuracy of DKI and DTI fiber orientation estimates relative to those of DSI.

Acquisition parameters common to both DSI and DKI acquisitions were: voxel size = 2.7 × 2.7 × 2.7 mm^3, matrix = 82 × 82, number of slices = 45, bandwidth = 1356 Hz/Pixel, and a 32 channel head coil with an acceleration factor of 2 using generalized autocalibrating partially

parallel acquisition (105) and adaptive combine coil mode (106). Additional parameters for the DSI acquisition were TR/TE = 8300/151 ms and a total of 515 diffusion encoding gradient directions over a Cartesian grid with a maximum b-value of 6000 s/mm^2, which was optimized for diffusion sensitivity and gradient performance (70), resulting in a total acquisition time of 71.7 minutes. For the DKI acquisitions, additional parameters were TR/TE = 6100/102 ms, 64 diffusion encoding gradient directions at b-values of 1000 s/mm^2 and 2000 s/mm^2 , and a total of 20 independent acquisitions without diffusion weighting (b0 images), resulting in a total acquisition time of 15.6 minutes. In both cases, TE was minimized to maximize SNR. DTI data were also analyzed using the 0 and 1000 s/mm^2 b-value images from the DKI dataset. During each session, an additional T1-weighted magnetization-prepared rapid gradient echo (MPRAGE) image with 1.0 × 1.0 × 1.0 mm^3 voxel dimensions was also acquired for anatomical reference. By assuming 80% of the maximum gradient strength (45 mT/m), i.e. 36 mT/m, was used to achieve the minimum echo time δ and Δ can be estimated to be 32 ms and 74 ms for the DSI scan, and for 22.5 ms and 50 ms for the DKI scan, respectively.

Each scan for each subject was co-registered to the subject's initial DSI scan using a 12-parameter affine transformation with SPM12 (Wellcome Trust Center for Neuroimaging, London, UK). Following co-registration, spatial smoothing was applied to all diffusion weighted images to reduce the effects of signal noise using a Gaussian smoothing kernel of 1.25 times the voxel dimensions (52).

The intra-voxel DSI dODF was reconstructed using DSI Studio (dsi-studio.labsolver.org, Department of Psychology, Carnegie Mellon University) with a Hanning filter of width 17 applied to the q-space data. DKI-derived diffusion and kurtosis tensors were calculated using a

constrained weighted linear least squares algorithm (52), and the DKI dODF was calculated using the closed form solution derived by Jensen et al. (32). The DTI-derived diffusion tensor was obtained by using weighted linear least squares (73). Following previous studies, the radial weighting power was set to $\alpha = 2$ for DSI (39,67) and $\alpha = 4$ for DKI (32,71,104). For visualization of DTI dODFs, the radial weighting power was set to $\alpha = 4$; however this has no effect on the DTI-derived orientation estimates. All orientations were corrected for rotations of the image volume that occurred during image acquisition and co-registration (66). The kurtosis dODF reconstruction was performed using the Diffusional Kurtosis Estimator Fiber Tractography Module (https://www.nitrc.org/projects/dke/), and the DTI dODF was reconstructed using in-house software.

Angular variability of the dODFs was calculated by the absolute voxel-wise angular difference for each reconstruction between the principal orientation (the orientation corresponding to the global maxima pair) from the first scan and the nearest orientation from the second scan. Angular errors in the DKI and DTI dODFs were calculated using the absolute angular differences between the principal orientation from the corresponding DSI scan and the nearest dODF maximum from the respective reconstruction. For angular difference measures, the nearest orientation in the second scan was chosen as opposed to the global maximum from the second scan as small fluctuations in dODF magnitudes in voxels with multiple orientation estimates could vary which orientation was identified as the global maximum resulting in artificially large angular differences (104). Angular error estimates include intrinsic variability in the reconstruction techniques and hence combine both random and systematic error. In addition, because absolute differences are employed, these measures are positively biased by noise and will

consequently overestimate the true systematic differences. The experimental design is illustrated in Figure 17, and the angular variability and error measures are illustrated in Figure 18.

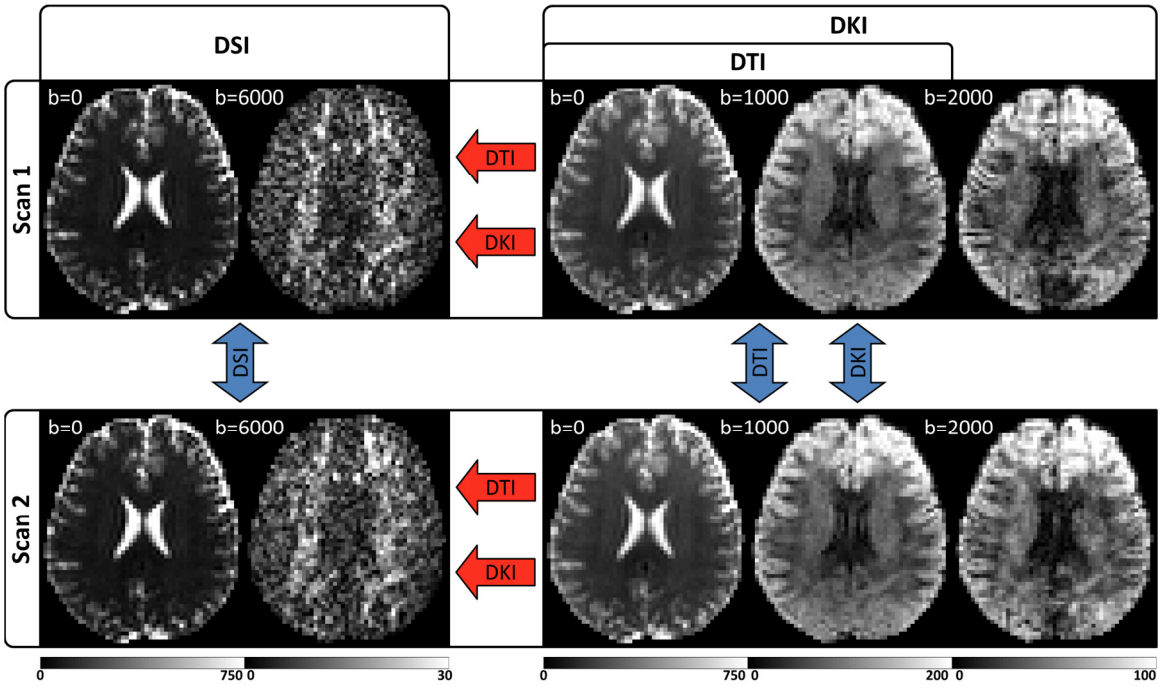

Figure 17. Experimental design illustrated with example images from a single subject. For each subject, 2 separate scans are performed, which include independent DSI and DKI acquisitions optimized for the respective reconstructions. The DTI reconstruction is calculated from a subset of the DKI acquisition and is fully independent from the DSI scan but not the DKI scan. Angular variability is calculated between scans (blue arrows) and angular error is calculated for DKI and DTI in reference to the corresponding DSI scan (red arrows). Units for the b-value are s/mm^2, and the signal intensity ranges for each image are given by the corresponding color bar (in arbitrary units). DWIs from the highest b-value for each acquisition are given to illustrate the range of diffusion weighting applied, and for all DWIs shown, the diffusion encoding vector was oriented in the left-right orientation ($\boldsymbol{n} = [1,0,0]^T$).

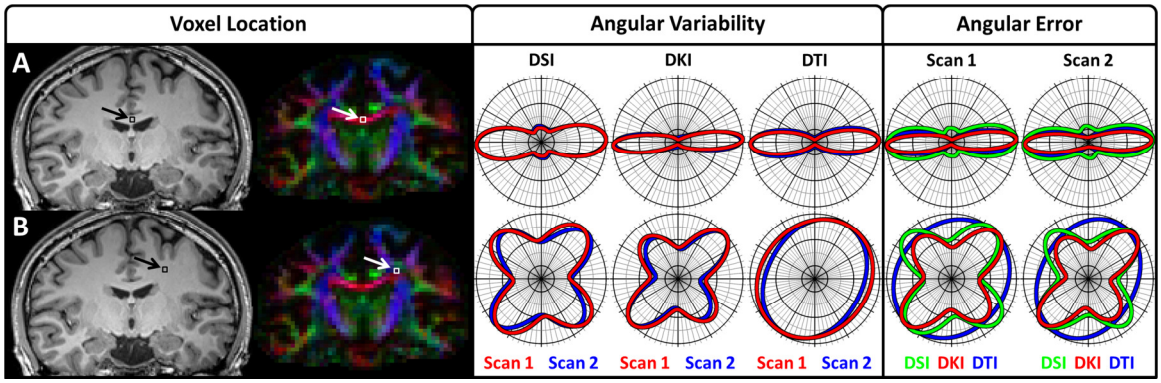

Figure 18. Polar 2D dODF cross-section plots illustrate angular variability and angular error measures. Row (A) illustrates dODFs taken from a single voxel in the corpus callosum where one predominant fiber bundle orientation is expected, and Row (B) illustrates dODFs taken from a single voxel where multiple fiber bundles are expected to occur between cortical projections from the corpus callosum and ascending and descending fiber bundles in the corona radiata. The Voxel Location tab illustrates the location of the voxels overlaid on the corresponding slice from the MPRAGE image and the FA color map for anatomical reference; the Angular Variability tab illustrates angular variability measures, which are taken between scans for each reconstruction; and the Angular Error tab illustrates the angular error measures, which are taken relative to the corresponding DSI dODF for each scan. The slice plane for the polar plots is rotated to contain the first and second largest orientations of the DSI dODF, as DSI is used as a reference. For visualization, each dODF is scaled to a maximum value of 1.

To quantify angular variability and angular error, ROIs were defined for each subject. These include an inclusive white matter ROI, which was defined as voxels with FA > 0.1; a conservative white matter ROI, which was defined as voxels with FA > 0.3; a single fiber bundle ROI, which was defined as voxels within the inclusive white matter ROI with the estimated number of fiber directions (NFD) equal to 1 in the DSI scan; a two crossing fibers ROI, which was defined as voxels within the inclusive white matter ROI with NFD = 2 in the DSI scan; and a 3 or more crossing fibers ROI, which was defined as voxels within the inclusive white matter ROI with NFD $\geq$ 3 in the DSI scan. To reduce CSF partial volume effects, voxels within each ROI with mean diffusivity > 1.5 $\mu m^2/ms$ were excluded from quantitative analyses (32,104). To help reduce the occurrence of spurious peaks in the DSI reconstruction a quantitative anisotropy

threshold of 0.1 was used to filter the DSI orientations (107). To visualize group differences in the angular variability and angular error measures, parameter maps from each subject were normalized to the International Consortium for Brain Mapping white matter template (53) using SPM12 with non-linear registration, and average, group-wise parameter maps were constructed.

The angular error estimates quantified in this study include two sources of error; intrinsic variability resulting from random error in independent acquisitions and systematic error inherent to the DTI and DKI dODF approximations. Intrinsic variability results from thermal noise, insufficient SNR, insufficient q-space sampling resolution, and physiological effects such as pulsatile flow, CSF partial volume effect, and bulk subject motion. Systematic error results from theoretical and methodological error in the dODF approximations employed. By assuming the angular variability is equivalent for all three techniques, the intrinsic variability from the angular error estimate reduces to the angular variability calculated between repeated scans. Thus, the qualitative degree of systematic error can be appreciated by the difference between the angular error and respective angular variability estimates for a given reconstruction method. In this study we used this heuristic method for calculating systematic error in DTI and DKI by assessing the difference between the angular error and angular variability measures for the DTI and DKI reconstructions.

White matter tractography was performed with DSI Studio using the Euler method (74) with a step size of 1.35 mm, a minimum track length of 20 mm, and a maximum track length of 450 mm. For direct and qualitative comparison across the three techniques, a common white matter tracking ROI was defined to include regions in the inclusive white matter ROI with quantitative anisotropy > 0.1 in the DSI scan. The fiber tracking algorithm was seeded with 200,000 random

seed points within the white matter tracking ROI. White matter fiber tracts were visualized using TrackVis (trackvis.org, Martinos Center for Biomedical Imaging, Massachusetts General Hospital). Tractography results are assessed qualitatively by examining the reconstructed tracts over the whole brain and in specific regions with complex fiber bundle geometries, including corpus callosum, cortico-spinal tract, superior longitudinal fasciculus, and cingulum bundle, as shown in the video provided in the online-supplemental material for Glenn et al. (108). To aid the qualitative assessment visually, a color-encoding scheme is employed where each individual tract is colored by its overall displacement from the starting point to the ending point of the tract, with red indicating a left-right displacement, blue indicating an inferior-superior displacement, and green indicating an anterior-posterior displacement. Similar colors represent similar overall trajectories whereas differing colors indicate tracts following different overall trajectories.

Results

Summary statistics for each subject and ROI are given in Table 2. DTI has the lowest angular variability in both the inclusive and conservative white matter ROIs as well as the single fiber bundle ROI, and DSI has the lowest angular variability in the both the two and three or more crossing fibers ROI. Conversely, DKI has the highest angular variability in all ROIs, with the exception of the three or more crossing fibers ROI, where DTI has the highest angular variability. However, the angular variabilities for all reconstructions are comparable within each of the ROIs, differing by at most 2.1 degrees in the single fiber bundle ROI. On the other hand, DKI consistently improves angular error compared to DTI in all ROIs. Moreover, the DKI angular error measures are typically comparable to the size of the DKI angular variability estimates, differing by at most 3.2 degrees in the 3 or more crossing fibers ROI, whereas the DTI angular error measures are larger relative to their angular variability estimates, increasing to 11.9 degrees

in the 3 or more crossing fibers ROI, supporting the notion that the DTI dODF approximation assumes greater systematic error relative to the DKI dODF approximation. For the ROIs tested, dODF performance measures are significantly influenced by the FA value, with the reliability being greater for regions with higher FA. Conversely, the occurrence of crossing fibers decreases the reliability of dODF-derived orientation estimates. However, the performance of the DKI dODF is less affected than the DTI-derived dODF in crossing fiber regions. Performance of the dODF reconstructions is explored further in Figs 19 and 20.

Table 2. Summary of dODF performance stats in the FA- and NDF-defined white matter ROIs.

Inclusive White Matter ROI (FA > 0.1)

	Angular Variability			Angular Error		Systematic Error	
	DSI	**DKI**	**DTI**	**DKI**	**DTI**	**DKI**	**DTI**
Subject 1	8.7 (9.7)	8.2 (9.4)	7.6 (9.9)	9.9 (10.4)	13.7 (13.8)	1.7	6.1
Subject 2	9.5 (9.7)	9.9 (9.9)	7.7 (9.7)	11.4 (12.3)	14.0 (14.0)	1.4	6.3
Subject 3	6.4 (7.6)	8.3 (9.3)	7.4 (9.3)	10.0 (10.4)	13.8 (14.1)	1.7	6.5
Mean	8.2 (9.0)	8.8 (9.5)	7.6 (9.7)	10.4 (11.0)	13.8 (14.0)	1.6	6.3

Conservative White Matter ROI (FA > 0.3)

	Angular Variability			Angular Error		Systematic Error	
	DSI	**DKI**	**DTI**	**DKI**	**DTI**	**DKI**	**DTI**
Subject 1	5.3 (5.7)	4.8 (5.6)	4.4 (5.8)	6.2 (6.6)	10.1 (10.7)	1.4	5.7
Subject 2	5.4 (5.4)	5.8 (5.4)	4.3 (5.6)	6.2 (7.1)	9.4 (10.1)	0.4	5.2
Subject 3	3.7 (4.6)	5.2 (5.7)	4.8 (6.3)	6.3 (6.9)	9.9 (10.7)	1.1	5.0
Mean	4.8 (5.2)	5.3 (5.6)	4.5 (5.9)	6.2 (6.9)	9.8 (10.5)	1.0	5.3

Single Fiber ROI (NFD = 1)

	Angular Variability			Angular Error		Systematic Error	
	DSI	**DKI**	**DTI**	**DKI**	**DTI**	**DKI**	**DTI**
Subject 1	8.3 (8.3)	7.8 (8.2)	6.4 (7.6)	9.0 (8.7)	10.2 (9.7)	1.2	3.8
Subject 2	8.8 (8.2)	9.2 (8.4)	6.0 (6.4)	10.0 (9.9)	10.5 (9.7)	0.9	4.6
Subject 3	6.3 (7.0)	8.0 (8.4)	6.2 (7.4)	9.4 (9.2)	10.9 (10.8)	1.4	4.7
Mean	7.8 (7.8)	8.3 (8.4)	6.2 (7.1)	9.5 (9.3)	10.6 (10.1)	1.2	4.4

Two Crossing Fibers ROI (NFD = 2)

	Angular Variability			Angular Error		Systematic Error	
	DSI	DKI	DTI	DKI	DTI	DKI	DTI
Subject 1	9.2 (10.9)	8.7 (10.3)	8.8 (11.5)	10.7 (11.7)	17.4 (16.2)	2.0	8.6
Subject 2	10.0 (10.9)	10.5 (10.8)	9.3 (11.5)	12.4 (13.7)	17.4 (16.2)	1.9	8.1
Subject 3	6.6 (8.6)	8.6 (10.4)	9.2 (11.6)	10.8 (11.8)	18.2 (16.7)	2.2	9.0
Mean	8.6 (10.1)	9.3 (10.5)	9.1 (11.5)	11.3 (12.4)	17.7 (16.4)	2.1	8.6

Three or More Crossing Fibers (NFD ≥ 3)

	Angular Variability			Angular Error		Systematic Error	
	DSI	DKI	DTI	DKI	DTI	DKI	DTI
Subject 1	9.7 (12.3)	9.0 (11.7)	10.4 (14.1)	12.6 (14.1)	22.4 (18.9)	3.5	12.0
Subject 2	11.3 (12.4)	12.0 (13.1)	11.4 (14.5)	14.9 (16.6)	21.7 (19.4)	2.9	10.3
Subject 3	7.7 (10.0)	10.1 (12.3)	11.6 (14.0)	13.2 (14.3)	24.8 (19.8)	3.0	13.2
Mean	9.6 (11.6)	10.4 (12.4)	11.1 (14.2)	13.5 (15.0)	23.0 (19.4)	3.2	11.8

Note: Values for angular variability and angular error represent the mean (± standard deviation) of the voxel-wise performance measures throughout the ROI. Systematic error is calculated by the difference between the mean angular error and the mean angular varibility over each ROI for the respective reconstructions. All values are given in degrees.

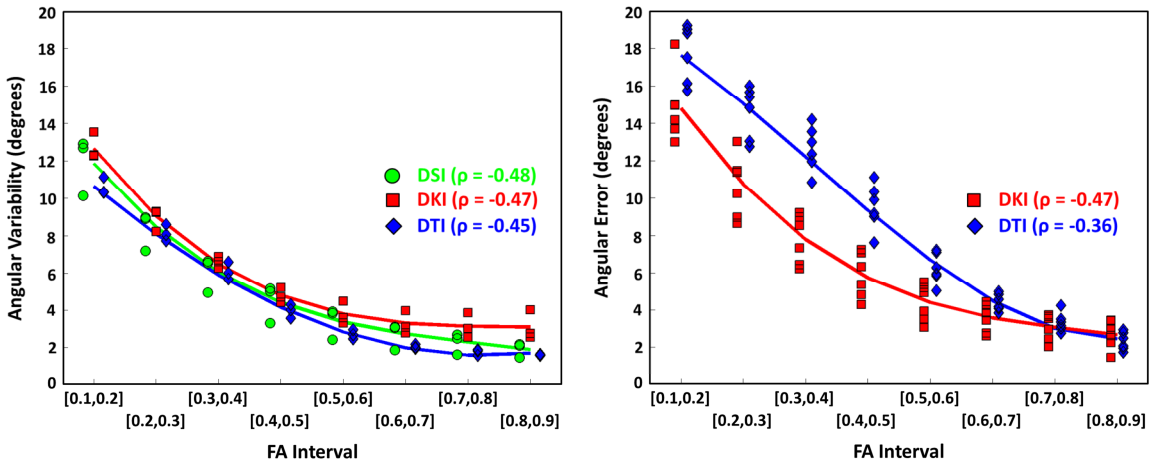

Figure 19. The performance of dODF-derived orientation estimates depends on FA, with angular variability and angular error decreasing with increasing FA. Data points for each group are averaged over the indicated interval and are separated in the horizontal direction within each interval for legibility. The Spearman rank correlation coefficient for the voxel-wise performance measure relative to FA is indicated by ρ.

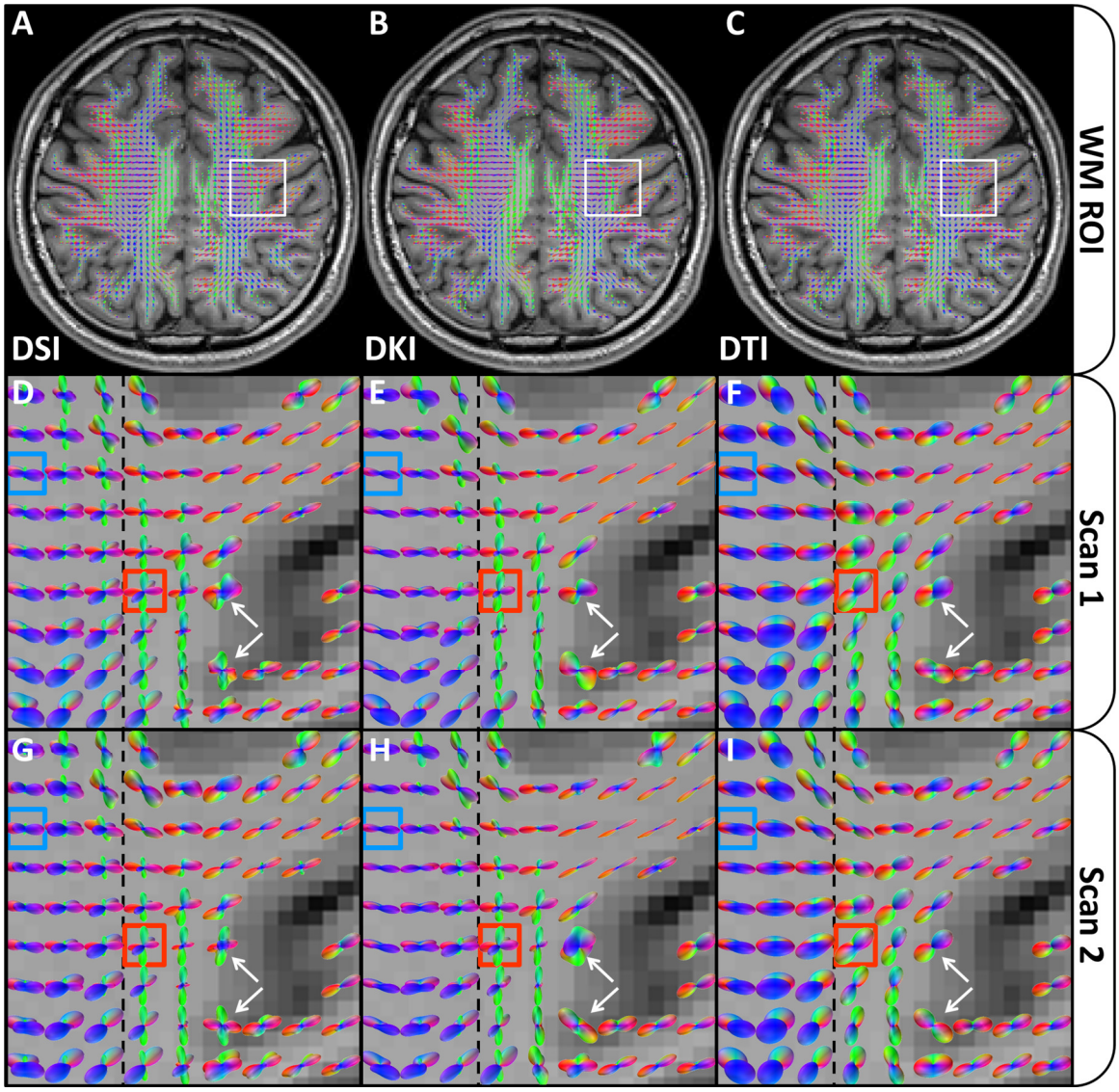

Figure 20. For each reconstruction, dODFs within the inclusive white matter ROI are overlaid on the MPRAGE image for anatomic reference. The dODF reconstructions are qualitatively consistent between repeat scans, but DTI cannot detect crossing fibers (red box); this feature may increase angular error relative to DSI. DSI is more sensitive than DKI at detecting crossing fibers (blue box). The inclusive white matter ROI may include partial volume effects (white arrows), which may increase variability and error in orientation estimates.

To illustrate the group-wise performance of the dODF reconstructions, mean normalized parameter maps are given in Figure 21. All three of the reconstruction techniques demonstrate similar angular variability throughout the white matter, but DTI shows improvements in angular

variability in regions with high FA (for example note the corpus callosum and corticospinal tracts in rows 2 and 3, which show high FA contrast). The DKI angular error estimates are relatively consistent throughout the white matter, whereas the DTI angular error estimates show distinct white matter regions where the angular error deteriorates. In comparing these regions to the normalized FA color maps, it is likely that these regions represent voxels with more complex fiber bundle geometries owing to influences from multiple fiber bundle orientations within a voxel (for example, note the intersecting regions between the corpus callosum and corona radiata which are apparent in rows 1 and 3).

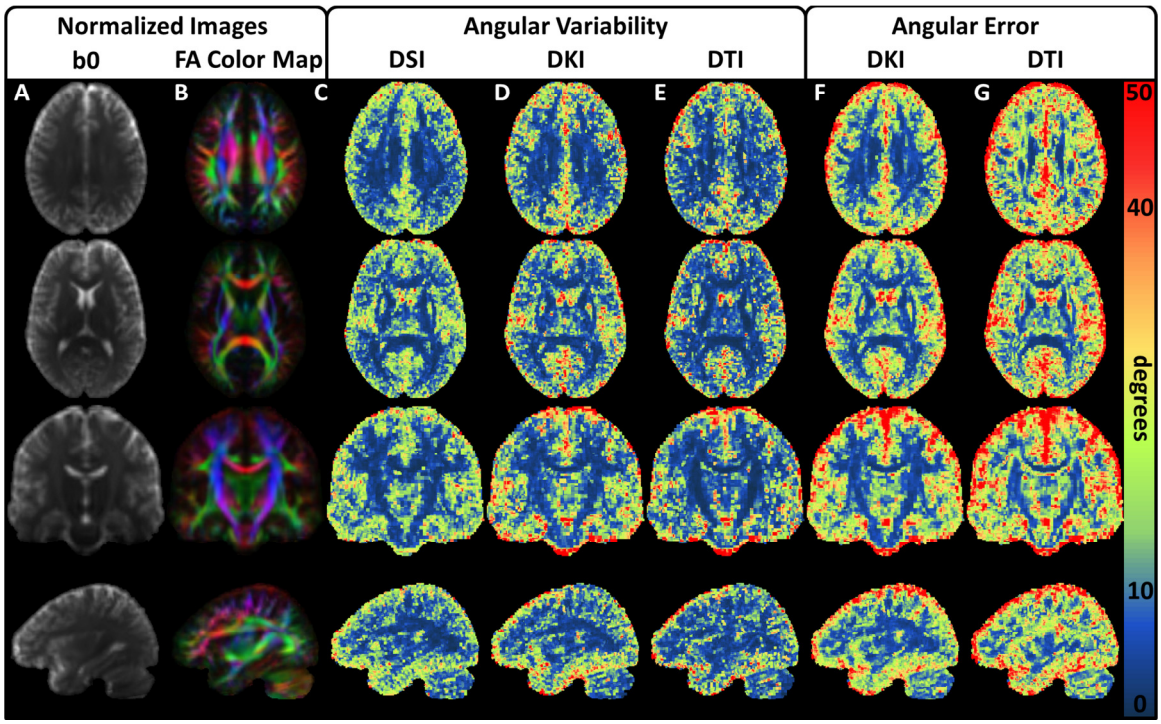

Figure 21. Group mean angular variability and angular error maps illustrate dODF performance. (A-B) Mean of the normalized b0 and FA color map images, respectively, from all DKI acquisitions. These are included for anatomical reference and to help validate the normalization procedure. The rows illustrate representative transverse, coronal, and sagittal orientations. (C-E) Illustrate angular variability for the DSI, DKI, and DTI reconstructions, respectively. All three techniques demonstrate similar angular variability in the white matter regions. (F,G) Illustrate angular error for the DKI and DTI reconstructions, respectively. Angular error measures increase

significantly in regions with low FA, though the angular error for the DKI reconstruction is relatively consistent throughout the white matter. The angular error is higher for the DTI reconstruction in the white matter, particularly in regions where complex fiber bundle geometries may be present.

Exemplary tractography results are given in Figure 22. A cross-sectional view of the fiber tracts was selected to highlight the effects of interactions that occur in regions with complex tissue architecture. This particular slice was chosen as it contains large influences from the corpus callosum, which is mainly oriented along the left-right orientation, and the cortico-spinal tracts (among others), which are mainly oriented along the inferior-superior orientation. This slice also contains effects from the superior longitudinal fasciculus and the cingulum bundle, which are mainly oriented along the anterior-posterior direction. In the tractography panels for DSI and DKI, the corpus callosum can be seen fanning through the corona radiata as it passes from one hemisphere to the next. However, strong influences form the corona radiata obscure these trajectories from the DTI dODFs, and the corpus callosum tracts are either prematurely truncated or swept into the corticospinal tracts. It can also be seen from these images that the DSI dODF approximation is more sensitive at detecting multiple peaks (note the extent of the superior longitudinal fasciculus fibers (white arrow) and the predominance of green lobes in the respective 3D dODF renderings). DTI is not capable of directly resolving crossing fibers, which significantly affects tractography through complex regions such as this. Full brain tractography results are compared with a video provided in the supplemental material for Glenn et al. (108).

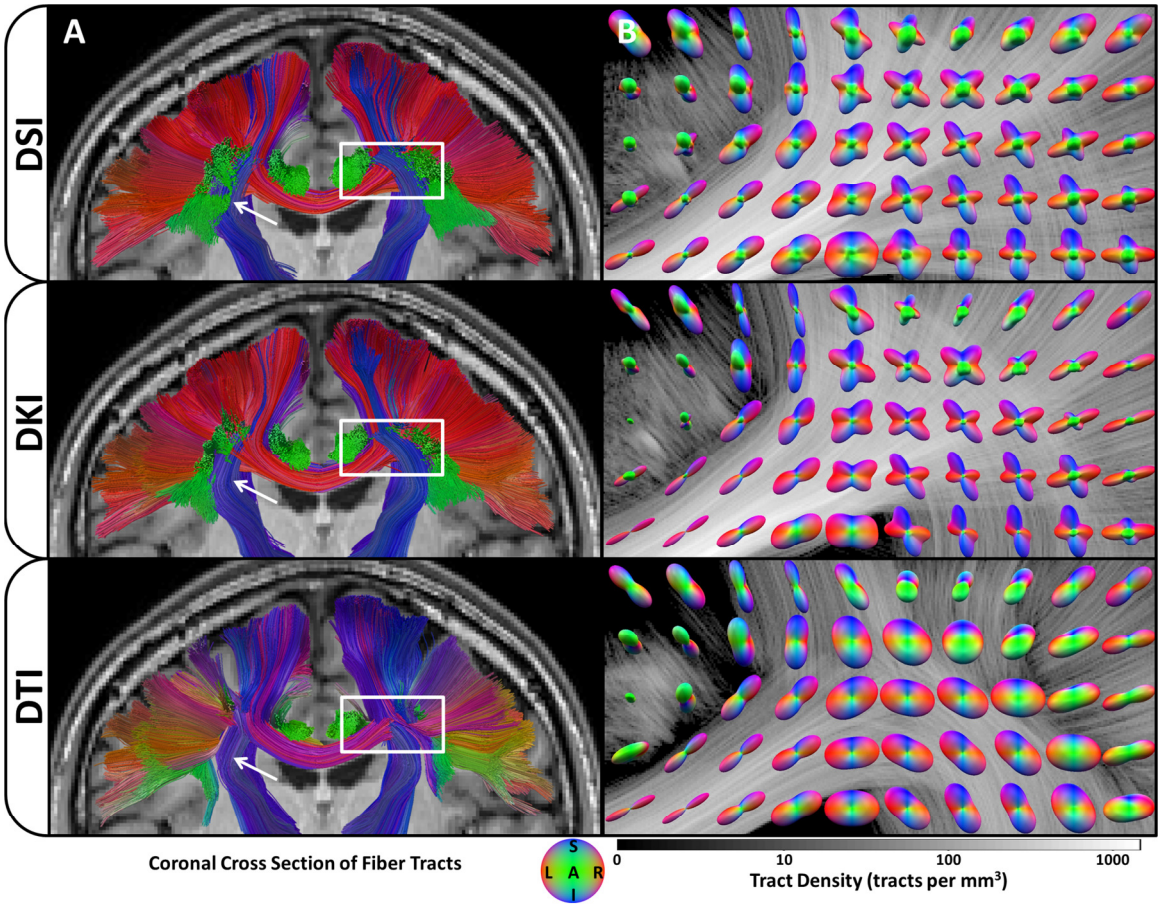

Figure 22. Effects of dODF reconstructions on tractography. Column (A) shows a coronal cross section through the fiber tracts identified with DSI, DKI, and DTI, respectively, overlaid on the corresponding slice from the MPRAGE image for anatomical reference. The color encoding is used to represent the overall displacement of the end points of each tract with one color being applied per tract, where red represents an overall left (L) – right (R) orientation, blue represents an overall inferior (I) – superior (S) orientation, and green represents an overall anterior (A) – posterior orientation. DSI is the most sensitive technique for detecting fibers (White Arrow); however, DSI and DKI are fairly similar in both the color, which illustrates the overall trajectory, and distribution of fibers identified. Column (B) shows selected dODFs colored with the same coloring scheme as fibers in column (A). The region shown in Column (B) is demarcated by the white box in the corresponding images in Column (A). DTI fibers are significantly affected in this region, as the dODFs cannot detect crossing fibers causing fibers to prematurely terminate or meld anatomically distinct tracts. This cross section was chosen to demonstrate interactions that occur between the corpus callosum, corona radiata, superior longitudinal fasciculus, and cingulum bundle, and their effects on dODFs and subsequent tractography.

Discussion

In this chapter, we have employed DSI as a reference standard to assess the angular error in orientation estimates from DKI and DTI and quantified the intra-subject angular variability of white matter fiber bundle orientation estimates from DTI, DKI, and DSI. We have focused primarily on comparing the estimated fiber orientations that the dODFs identify, as these are the inputs needed for constructing dMRI tractography. However, it should be emphasized that these are only approximations for the true fiber orientations, which are not easily verified for in vivo human experiments, even if the dODF is measured exactly.

There have been a significant number of prior studies employing DKI to measure neuropathological changes in a variety of disease states using voxel-based scalar measures (55,56,59,94-103). A primary goal of this study is to assess the potential of DKI for conducting tractography using in vivo human data for strengthening its use on future clinical applications, such as presurgical planning (89,90) and potentially, assessing the prognosis of postsurgical functional deficits (109). By estimating the kurtosis tensor, DKI is more apt to characterize diffusion phenomena within complex neural fiber structures than conventional DTI, which may improve the accuracy of tractography. Therefore DKI may be particularly well suited for clinical applications where tractography and quantitative assessment of tissue microstructure are of interest.

Since the performance of DKI tractography has not been tested against other advanced diffusion techniques for in vivo human data, in the present study, we use DSI as a gold standard tractography technique to assess the accuracy of the DKI-based dODF as well as improvements

gained over conventional DTI. However, quantifying the error in DKI and DTI is complicated as all measurement techniques, including DSI, contain intrinsic, random variability. Therefore, in assessing error in the DKI and DTI orientation estimates, it is crucial to assess the random variability that can be expected between independent, repeated measures. Thus, the angular variability and angular error measures used in this study differ in that angular variability quantifies intrinsic, random variation in each measurement technique, whereas angular error consists of both random variation from independent measures and systematic sources of error incurred by assuming either the DKI or DTI dODF approximations. Since little is known a priori about the probability distributions that govern the angular variations, we use the heuristic definition of systematic error as the difference between the angular error measured relative to DSI and the angular variability measured between repeated acquisitions for each reconstruction. Minimizing systematic error is paramount for tractography as error accumulates along the length of each tract and large sources of error can potentially result in systematically misleading information.

In order to acquire high quality, whole-brain DSI and DKI datasets for evaluation, the total scan time employed in this study was long relative to typical clinical protocols. Since a goal of this study was to evaluate the dODF accuracy, we optimized our protocol for high SNR rather than a short acquisition time. As a result, the acquisition times reported here do not reflect those optimized for clinical scanning, as there are additional strategies to increase acquisition efficiency. For example, there have been a number of successful efforts to decrease the q-space sampling burden of DSI, including decreasing the q-space sampling density by sampling fewer points (70,110), sampling only one-half of q-space by assuming symmetry of the q-space data (111,112), or sampling only a quarter of q-space using compressed sensing (113). The echo train

time (and repetition time) can also be reduced with faster gradients or multi-slice EPI (114-118). In addition, stronger diffusion encoding gradients can be used to reduce the echo time (and repetition time) to improve the SNR while reducing acquisition time (118). Although DSI may show the largest improvement in acquisition time, these considerations are generally applicable to DKI as well. Moreover, there may be a trade-off in the error and variability of angular orientation estimates if SNR is compromised, as may occur with accelerated acquisition schemes (117), or if sparse q-space sampling schemes are employed (111). Nevertheless, DKI may be assumed to have generally shorter acquisition times than DSI due to the assumption that DKI estimates only the second and fourth cumulants of the dPDF, which requires less information than determining the full dPDF (119).

In general, DKI decreases the angular error compared to DTI and the angular variability estimates are comparable for all three reconstructions in all ROIs, differing by at most 2.1 degrees in the single fiber ROI. However, DKI tends to have increased angular variability compared to both DTI and DSI in all ROIs except for the ROI with three or more crossing fiber bundles. Although the precise origin of this is unclear, DKI's increased angular variability could result from a trade-off between estimation error from incomplete q-space sampling distributions and subject motion, which accumulates over the duration of the scan. DTI, for example, requires the shortest acquisition time, which may result in the lowest contributions of subject motion to angular variability. DSI, on the other hand, uses a large number of diffusion encoding vectors to characterize diffusion dynamics, which could have lower angular variability from the dODF reconstruction but an increased likelihood for subject motion. DKI is also known to be sensitive to reconstruction artifacts resulting from Gibbs ringing (120,121) and noise bias (122), although this is also expected to affect DSI.

There are a variety of additional techniques which can be used to resolve the orientations of crossing fiber bundles for tractography. For example, fiber bundle orientations can be estimated from directional diffusional kurtosis estimates provided by DKI without estimating the dODF directly (71) or the white matter fiber bundles may be modeled mathematically and used to estimate a model-dependent, fiber orientation distribution function, for example using fiber ball imaging (64) or constrained spherical deconvolution (83,84). Since neither of these techniques is directly analogous to the dODF, they were not included in the present study. However, the diffusional kurtosis approach has been show to increase fiber detection through the corpus callosum (71), and constrained spherical deconvolution has been shown to be highly sensitive for detecting crossing fibers (77), as well as for increasing detection of crossing fibers at low b-value (85).

A potential limitation of this study design is that by optimizing the SNR of each sequence for the respective reconstructions we have not fully addressed the issue of acquisition times, which is one of the key obstacles for clinical scanning. Indeed, doubling the acquisition time to acquire DKI may be prohibitive in some clinical settings. A useful follow-up study would be to quantitatively investigate the differences in the orientation estimates using protocols with similar acquisition times that are suitable for clinical scanning. By focusing on shorter acquisitions, additional reconstructions could also be included to test model-based fODF measures such as CSD or fiber ball imaging. However, it is important to emphasize that DTI, DKI, and DSI share a common feature in that they are theoretically based on physical properties of water diffusion. In contrast, model-based approaches make explicit assumptions about the relationship between white matter and the dMRI signal in order to characterize more specific features of tissue

microstructure. Although mathematical modeling can increase the resolving power for detecting multiple fiber bundle orientations, definitive validation of modeling assumptions has not yet been achieved in healthy or diseased brains.

To summarize, in this study we acquired a unique dataset with 6 full DSI and DKI acquisitions with a total of 515 and 128 diffusion weighted images, respectively, from 3 healthy volunteers in order to quantify dODF performance measures from DSI, DKI, and DTI for *in vivo* human data. In general, DKI decreases the error of dODF orientation estimates relative to DTI. Moreover, DKI enables the detection of crossing fibers, which has pronounced improvements relative to DTI for tractography throughout regions with complex fiber bundle geometries. With improved tractography results relative to DTI and shorter typical scan times than DSI, DKI-based tractography is potentially more applicable to a variety of clinical applications. However, future studies will be needed to more fully investigate the potential utility of DKI-based tractography.

Conclusion

The higher order information provided by the kurtosis tensor enables DKI to directly resolve crossing fibers and improves the accuracy of DKI relative to DTI for tractography. Both DKI and DTI are capable of mapping the single predominant fiber bundle orientation, but the angular error of DTI deteriorates in regions with complex fiber orientations due to its theoretical limitation under the assumption of Gaussian diffusion. DSI, DKI, and DTI all have comparable angular variability; however, DKI has decreased angular error in the dODF approximation relative to DTI. With a shorter typical scan time than DSI, DKI is potentially more suitable for a variety of clinical applications.

6

Surgical Outcomes Prediction in Epilepsy

Epilepsy is a serious neurological disorder which can be difficult to manage clinically. In this chapter, we will explore the potential of combining quantitative, tensor-derived parameters with along-the-tract white matter tissue characterization for surgical outcomes prediction in patients with refractory temporal lobe epilepsy. This chapter is based on the following peer-reviewed publication:

1. Keller SS[§], **Glenn GR[§],** Weber B, Kreilkamp B, Jensen JH, Helpern JA, Wagner J, Barker GJ, Richardson MP, Bonilha L. Preoperative automated fiber quantification predicts postoperative seizure outcome in temporal lobe epilepsy. *Brain*. [Under Review].

§ Shared first authorship

Abstract

Approximately one in every two patients with pharmacoresistant temporal lobe epilepsy (TLE) will not be rendered completely seizure free after temporal lobe surgery. The reasons for this are unknown and are likely to be multifactorial. Quantitative volumetric Magnetic Resonance

Imaging (MRI) techniques have provided limited insight into the causes of persistent postoperative seizures in patients with TLE. The relationship between postoperative outcome and preoperative pathology of white matter tracts, which constitute crucial components of epileptogenic networks, is unknown. In the present study, we investigated regional tissue characteristics of preoperative temporal lobe white matter tracts known to be important in the generation and propagation of temporal lobe seizures in TLE, using diffusion tensor imaging (DTI) and Automated Fiber Quantification (AFQ). We studied 43 patients with mesial TLE associated with hippocampal sclerosis and 44 healthy controls. Patients underwent preoperative DTI, amygdalohippocampectomy and postoperative assessment using the International League Against Epilepsy (ILAE) seizure outcome scale. From preoperative DTI, the fimbria-fornix (FF), parahippocampal white matter bundle (PWMB) and uncinate fasciculus (UF) were reconstructed using AFQ, and scalar diffusion metrics were calculated along the length of each tract. 51.2% of patients were rendered completely seizure free (ILAE 1) and 48.8% continued to experience postoperative seizure symptoms (ILAE 2-5). Relative to controls, both patient groups exhibited strong and significant diffusion abnormalities along the length of the UF bilaterally, the ipsilateral PWMB, and the ipsilateral FF in regions located adjacent to the anterior and midportion of the medial temporal lobe. However, only patients with persistent postoperative seizures showed evidence of significant pathology of tract sections located in the ipsilateral dorsal fornix and in the contralateral PWMB. Using receiver operating characteristic (ROC) curves, diffusion characteristics of these regions could classify individual patients according to outcome with 84% sensitivity and 89% specificity. Pathological changes in the dorsal fornix were beyond the margins of resection, and contralateral PWMB changes may suggest a bi-temporal disorder in some patients. Furthermore, diffusion characteristics of the ipsilateral UF could classify patients from controls with a sensitivity of 98%; importantly, by co-registering the preoperative AFQ

maps to postoperative lacuna maps, we observed that the extent of UF resection was significantly greater in patients who were rendered seizure free, suggesting that a smaller resection of the UF may represent insufficient disconnection of an anterior temporal epileptogenic network. These results hold promise as imaging prognostic markers of postoperative outcome and may provide mechanistic explanations for why some patients with TLE continue to experience postoperative seizures.

Introduction

Epilepsy is the most common serious neurological disorder, affecting over 50 million people worldwide (123,124). Approximately 30% of all patients with a diagnosis of epilepsy will develop chronic pharmacoresistant epilepsy (125). Temporal lobe epilepsy (TLE) is the most common pharmacoresistant focal epilepsy disorder (126,127) and is potentially remediable by neurosurgical intervention.

In the only randomized controlled trial of surgery for refractory TLE, it was reported that surgical intervention is significantly superior for the attainment of seizure freedom one year after surgery compared to continuing pharmacological treatment (128); at one year, 58% of patients receiving surgery were free from seizures impairing awareness and 38% were free from any seizure related symptom, whereas only 8% were seizure-free in the non-surgical control group. There are contrasting reports regarding the proportion of patients attaining seizure freedom after temporal lobe surgery for refractory seizures, which may range from 35-80% (128-133). The most significant contributions to this variance are likely to be time to postoperative follow up (longer follow up is associated with lower seizure-free rate) and definition of seizure freedom (complete seizure freedom is associated with lower seizure-free rate relative to freedom from

disabling seizures only). The reasons underlying persistent postoperative seizures in patients who are seemingly excellent candidates for temporal lobe surgery are unknown. Although patients with TLE and neuroradiological evidence of hippocampal sclerosis (HS) have improved postsurgical outcomes relative to patients with TLE and no MRI lesion (130,131), between two-thirds and one-half of patients with HS will continue to experience postoperative seizures (131,134). Current suggestions for why these persistent postoperative seizures occur include a combination of insufficient resection of mesial temporal lobe tissue (135,136), mesial temporal lobe pathology existing outside the margins of resection (137-140), contralateral temporal lobe seizure involvement (137,141,142), occult extra-temporal lobe involvement, including temporal-plus epilepsy (143-146), thalamo-mesial temporal network alterations (147,148), and atypical subtypes of TLE that may be particularly resistant to conventional temporal lobe surgery (149-151). The development of predictive biomarkers for the future success of surgical intervention in epilepsy represents an important research endeavour, particularly as a reliable prognostic marker could inform patient clinical management and surgical decision-making.

As non-invasive imaging techniques improve, there is increasing interest in modelling brain connectivity. This endeavour is providing new insights into the structural and functional organisation of the human brain, as well as into how alterations in connectivity underlie neurological disorders. Understanding brain connectivity in epilepsy is particularly important given that even focal seizures may be generated in context of distributed epileptogenic brain networks (152,153). Diffusion tensor imaging (DTI) techniques permit the reconstruction of white matter tract bundles, which form the connections between cortical regions within structural networks. There has been increasing application of tractography techniques to study DTI scalar metric alterations for reconstructed white matter tracts in patients with TLE, with a particular

focus on tracts within and connecting to the temporal lobe (154). However, there is a paucity of data on the relationship between preoperative DTI tractography and postoperative seizure outcome after temporal lobe resection. This may be partly due to the fact that sophisticated DTI acquisitions are not incorporated into routine preoperative evaluation in a clinical setting. However, the application of graph theoretical methods to determine alterations in structural network topology is growing in TLE (152), and there have been recent attempts to correlate preoperative structural connectomes with postoperative seizure outcome in small groups of patients with TLE (155-157). Despite the interest in developing potential prognostic markers of outcome using preoperative connectomes, the underlying biological significance and anatomical specificity of such data are difficult to interpret.

Automated fiber quantification (AFQ) is a DTI tractography technique that permits a comprehensive analysis of tissue characteristics along the length of white matter tract bundles (158). This approach offers a potentially more sensitive measure of neuroanatomical white matter alterations in patients with neurological disorders than whole-tract approaches, as it considers regional intra-tract tissue characteristics. Tissue characteristics may vary considerably along a tract (159), which conventional DTI analyses of whole tract mean diffusion measures are unable to consider. Furthermore, it is likely that at least some pathological alterations in TLE occur in circumscribed regions of tracts and not along entire tracts. Such anatomical specificity could potentially improve the detection of anatomical prognostic markers of treatment outcome in patients with TLE.

In the present study, we applied AFQ to preoperative DTI in patients with TLE who underwent surgical treatment and postoperative follow-up, with a primary goal of identifying

preoperative diffusion markers of postoperative seizure outcome. We focused on three temporal lobe tract bundles that are known to be important in the generation and propagation of temporal lobe seizures and susceptible to pathological alterations in refractory TLE: the fimbria-fornix (FF) (160-162), parahippocampal white matter bundle (PWMB) (163-166) and uncinate fasciculus (UF) (165,167,168). A secondary goal of the present study was to determine whether extent of resection of the temporal lobe tract bundles was associated with seizure outcome. Whilst there are several studies that have addressed whether the general extent of resection is associated with outcome based on analysis of conventional (e.g. T1-weighted) MRI scans (135,148,169-173), there has to date been no assessment of the relationship between seizure outcome and extent of white matter tract resection.

Methods

Participants

We studied 43 patients with unilateral TLE with HS (27 left TLE, 16 right TLE; 23 females, 20 males; mean age 39.7 years, SD 12.6) and 44 neurologically healthy age- and sex-matched controls (28 females, 16 males; mean age 38.0 years, SD 14.0). Each patient had a comprehensive presurgical evaluation at University Hospital Bonn, Germany, that included clinical assessment of seizure semiology, interictal EEG, long-term video EEG monitoring, if clinically necessary additional invasive electrophysiological investigations, diagnostic MRI (T1-weighted, T2-weighted and FLAIR scans), and neuropsychological assessment (174). HS was identified by an expert neuroradiologist with considerable experience of lesion diagnosis in epilepsy, and was defined by hippocampal volume loss and internal structure disruption on T1-weighted scans, and/or hyperintensities on T2-weighted and FLAIR images. There was no evidence of bilateral HS in any patient, all patients had seizures of presumed unilateral temporal

lobe origin, and there was no evidence of a secondary extrahippocampal lesion that may have contributed to seizures. All patients underwent amygdalohippocampectomy (175), as well as routine diagnostic analysis of resected hippocampal specimens by an experienced neuropathologist. HS was histologically confirmed in all resected specimens (176). Postsurgical seizure outcome was assessed using the ILAE outcome classification system (177). All patients had a minimum of one year and an average of two year postoperative follow-up.

Image Acquisition

All study participants underwent MRI at the Life & Brain Center in Bonn on a 3 Tesla scanner (Magnetom Trio, Siemens, Erlangen, Germany). An eight-channel head coil was used for signal reception. T1-weighted MPRAGE images (160 slices, TR = 1300 ms, TI = 650 ms, TE = 3.97 ms, voxel size 1.0 × 1.0 × 1.0 mm, flip angle 10°, acquisition time approx. 7 min) were acquired for all controls and all patients prior to surgery. Postoperative T1-weighted data were acquired for 33 patients. Diffusion-weighted data (diffusion-weighted single shot spin-echo EPI sequence, TR = 12 s, TE= 100 ms, 72 axial slices, voxel size 1.726 x 1.726 x 1.7 mm, no cardiac gating, GRAPPA acceleration factor 2) was acquired for all controls and patients preoperatively. Diffusion gradients were equally distributed along 60 directions (b-value = 1000 s/mm^2). Additionally, six datasets with no diffusion weighting (b-value = 0 s/mm^2) (b0 images) were acquired in an interleaved fashion, with one b0 dataset preceding each block of 10 diffusion-weighted images.

Image analysis

Motion correction was performed on the diffusion-weighted data using SPM8 (Wellcome Trust Center for Neuroimaging, London, UK) using the initial b0 image for each subject as a reference,

with subsequent b0 images being co-registered with a 12-parameter affine transformation. The transformation for each b0 image was applied to the 10 subsequent diffusion-weighted images and the diffusion encoding vectors were corrected for all rotations of the image volume (66). After co-registration, an average b0 dataset was created, and the full DTI dataset was processed using the AFQ image analysis pipeline (https://github.com/jyeatman/AFQ).

AFQ performed a series of automated steps, including additional motion correction for each of the individual diffusion-weighted images and estimation of the diffusion tensor. Brain masks were created within AFQ using FSL's brain extraction tool (178) and tractography was performed within the brain mask using the Euler method with a step size of 1 mm, an angle threshold of 35 degrees, and a minimum tract length of 20 mm (179). Following tractography AFQ performed a non-linear normalization of the average b0 dataset to the International Consortium for Brain Mapping (ICBM) template using SPM. This nonlinear transformation was then used to map standardized white matter regions of interest (ROIs) from the ICBM template to the diffusion images, where AFQ automatically segmented the tractography data into fiber bundles of interest. Once fiber bundles were segmented, AFQ identified the core region of each bundle and calculated along-the-tract diffusion profiles along a fixed number of sections, which were analysed for individual and group-wise comparisons.

Fiber bundles were selected based on their hypothesized roles in TLE, and included the FF, PWMB, and UF. For segmentation of the FF, we implemented an in-house algorithm using AFQ's routine. Each fiber bundle was interpolated along 100 sections and along-the-tract profiles were reconstructed for mean diffusivity (MD) and fractional anisotropy (FA) for both left- and right-sided pathways. For patients with TLE, tract profiles were separated into ipsilateral and

contralateral sides, and for controls, tract profiles for left- and right-side pathways were combined. Tract profiles were excluded in instances where AFQ could not reconstruct the white matter pathways (159).

Statistical analysis of tract profiles

We compared tract profiles between healthy controls, patients rendered completely seizure free (ILAE 1) and patients with persistent postoperative seizure-related symptoms (ILAE 2-6). For statistical analysis, individual tract profiles were averaged over five ROIs consisting of sets of 20 consecutive sections. Comparisons were performed with a two sample t-test and multiple comparisons were corrected for using the false discovery rate (FDR) procedure (180). Effect size was quantified using Cohen's d parameter. The ROIs used are illustrated in Figure 23 along with representative tract profiles from a single patient with TLE. To illustrate the anatomical location of the observed differences, a section-wise t-score plot was reconstructed.

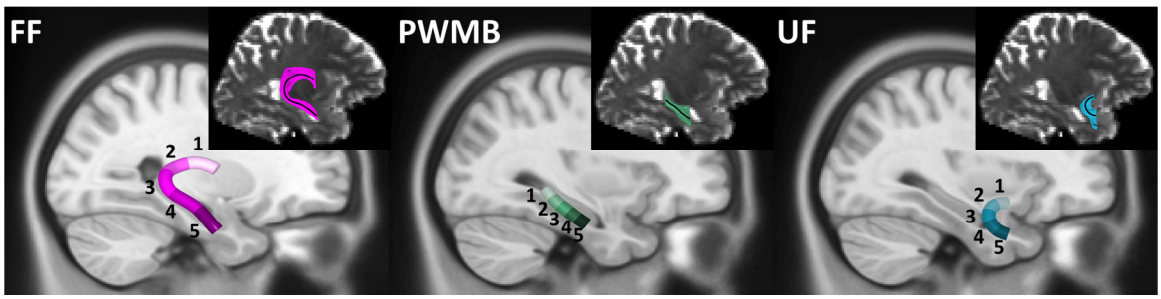

Figure 23. Anatomical location of fiber bundle ROIs used for statistical comparison. The inset for each fiber bundle illustrates representative tracts reconstructed for a single subject, with the solid black line indicating the AFQ-identified tract core used for calculation of the tract profiles. Tract cores for each subject are mapped to the ICBM template and averaged to indicate the group-wise representation of each fiber bundle. For statistical comparison, each fiber bundle is divided into 5 ROIs by averaging every 20 consecutive tract sections. ROI numbers correspond to the ROIs used in Figure 24 and in Table 4.

Development of potential biomarker assays

To test the potential clinical applicability of the preoperative diffusion-weighted data, receiver operating characteristic (ROC) curves for the along-the-tract profiles were calculated. For the ROC curves, ROIs were selected along each pathway based on observed differences in tissue characteristics, and individual tract profiles were averaged over each ROI. Sensitivity and specificity were assessed for group-wise separations between TLE and control groups as well as between patient outcome groups for incrementally decreasing values of the test parameter. The ROIs used to distinguish between patient outcome groups were also pooled to test the combination of multiple classifiers for outcome prediction.

White Matter Bundle Resection Analysis

33 of the 43 patients received postoperative structural imaging. Lacunar maps of the resected tissue volumes were traced on postoperative T1-weighted images as previously described (148), and postoperative images were normalized to the ICBM template using the Clinical Toolbox for SPM 181 (https://www.nitrc.org/projects/clinicaltbx/) with enantiomorphic normalization to account for loss of the resected tissue (182). Individual fiber bundles were then mapped to the ICBM template using the AFQ-identified non-linear deformation, and tract profiles were reconstructed using AFQ's routine over the normalized, binary lacunar maps. Thus, tract profiles were created by calculating the proportion of the resected fiber bundle at a given section overlapping with the resected tissue. The total proportion of an individual fiber bundle resected was then calculated by averaging over all sections. Comparisons between fiber bundle resections patient outcome groups were then made with a two sample t-test, correcting for multiple comparisons using the FDR. Fiber bundle resection maps were created using a two-step procedure. First, individual bundle resection maps were created by intersecting the binary mask

of the reconstructed fiber bundles with the normalized lacunar maps of the resected tissue for each patient. Subsequently the individual bundle resection maps were averaged, taking into account ipsilateral and contralateral distinctions by flipping the ipsilateral side to the left hemisphere. For anatomical reference, fiber bundle distribution maps were calculated for the control group by averaging the binary masks of the left-sided fiber bundles.

Results

Outcome

Of the 43 patients included in this study, 22 (51.2%) patients had an excellent postoperative seizure outcome (ILAE 1) and 21 (48.8%) had a suboptimal outcome (ILAE 2-5). No patient experienced worsening seizures after surgery (ILAE 6). A breakdown of clinical variables according to outcome groups is provided in Table 3. There were no significant differences between outcome groups with respect to patient age, age of onset of epilepsy, duration of epilepsy, seizure frequency, a history of childhood febrile seizures, or preoperative volumes of the hippocampus, or global grey and white matter. There were a greater proportion of males who were rendered seizure free relative to females (p=0.03).

Table 3. Clinical information with respect to outcome

	ILAE 1	ILAE 2+	sig
n	22 (51.2%)	21 (48.8%)	-
outcomes	1 = 22	2 = 5 3 = 7 4 = 8 5 = 1 6 = 0	-
left / right TLE	11/11	16/5	χ^2=3.2, p=0.12
female / male	8/14	15/6	χ^2=5.3, p=0.03
febrile seizures,	15/7	14/7	χ^2=0.01, p=0.59

no/yes			
age	38.8 (11.3)	40.6 (13.9)	F=0.22, p=0.64
onset	16.05 (11.49)	15.6 (10.5)	F=0.02, p=0.89
duration	22.7 (13.9)	25.0 (15.8)	F=0.25, p=0.62
seizure frequency	8.8 (18.7)	4.2 (2.3)	F=1.27, p=0.27
ipsi hipp vol	3329 (1129.7)	3120.1 (499.0)	F=0.96, p=0.41
contra hipp vol	4289.3 (703.1)	4155.7(602.6)	F=0.44, p=0.51
grey matter volume	462203.7 (74066.2)	449096.8 (80295.6)	F=0.31, p=0.58
white matter volume	474268.1 (72806.9)	476185.4 (79811.0)	F=0.01, p=0.94

Note. Outcome, side of TLE, sex, and incidence of febrile seizures are number. Age, age of onset of epilepsy, preoperative duration of epilepsy, preoperative seizure frequency, and volumes are mean (and SD). Hippocampal, grey matter and white matter volumes were calculated using Freesurfer software (164).

AFQ comparisons

Ipsilateral and contralateral tract profiles for ILAE 1 and ILAE 2+ groups relative to controls are shown in Figure 24, including corresponding histograms for average tract profiles over each ROI. MD tract characteristics were generally more revealing than FA characteristics. MD tract profiles were significantly higher in both outcome groups relative to controls along the entire length of the ipsilateral PWMB (Figure 24, left middle) and the UF bilaterally (Figure 24, left bottom). MD was also significantly higher for both outcome groups in the ipsilateral FF in ROIs 4 and 5. Conversely, only ILAE 2+ patients showed evidence of significantly increased MD within ipsilateral fornical ROIs 1-3 (Figure 24, top left). Controls and ILAE 1 patients had roughly equal MD characteristics within these ROIs. Fornical ROIs 4 and 5 were located in the mesial temporal lobe, ROIs 1 and 2 outside the temporal lobe, and ROI 3 in a transitional region between the two (Figure 23). Diffusion parameters of the contralateral FF were not altered in patient outcome groups relative to controls. There were additionally significant MD alterations only in ILAE 2+ patients located in contralateral PWMB ROIs 1-3 (Figure 24, middle left). To

illustrate the location of the observed MD differences, section-wise t-score plots are reconstructed in Figure 25. Areas in red represent significant regional increases in MD in the respective patient group relative to controls. Arrows indicate the areas exclusively altered only in patients with a suboptimal seizure outcome.

No significant alterations in contralateral FA tract characteristics were observed in patient groups relative to controls. Both patient outcome groups had reduced FA of the ipsilateral UF through the length of the tract, but only significantly so in ROIs 4 and 5 (increasingly anterior temporal) for ILAE 2+ patients (Figure 24, bottom right). The increase in MD exclusively in ILAE 2+ patients in the ipsilateral dorsal FF and contralateral PWMB were mirrored by a non-significant reduction in FA in the same regions (Figure 24, top right and middle right, respectively). Effect sizes for FA were generally smaller than the corresponding changes in MD. The results from Figure 24 are tabulated in Table 4.

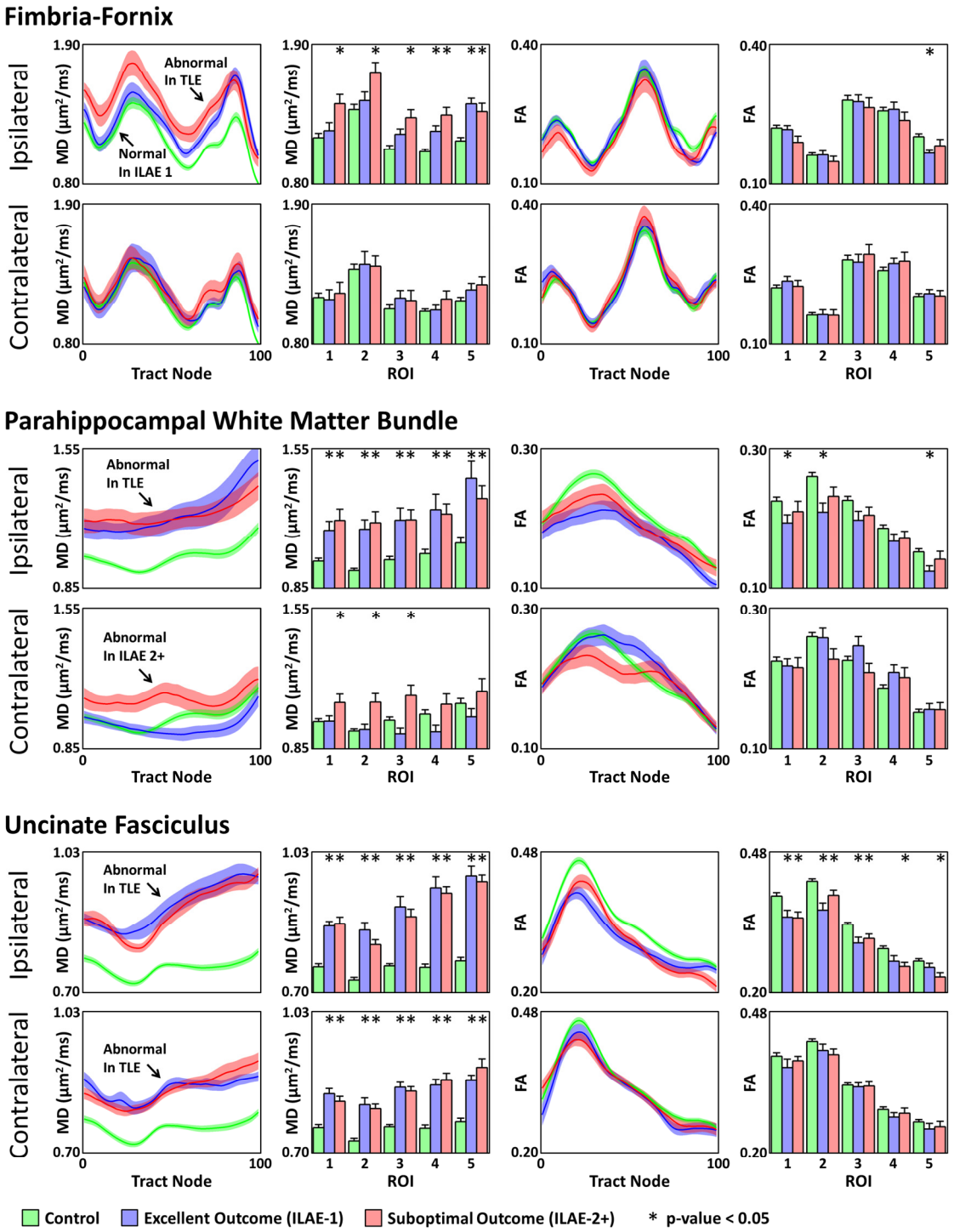

Figure 24. MD and FA tract profiles for mean (± SEM) for ipsilateral and contralateral tracts in the ILAE 1 and ILAE 2+ groups relative to controls. The histograms indicate the average tract

profile over a given ROI. In all cases, increasing tract section corresponds to increasing ROI number and the ROIs correspond to those given in Figure 23. The asterisk (*) indicates p-value < 0.05 compared to controls after correcting for multiple comparisons with FDR. Arrows highlight statistically significantly different regions in the MD tract profiles.

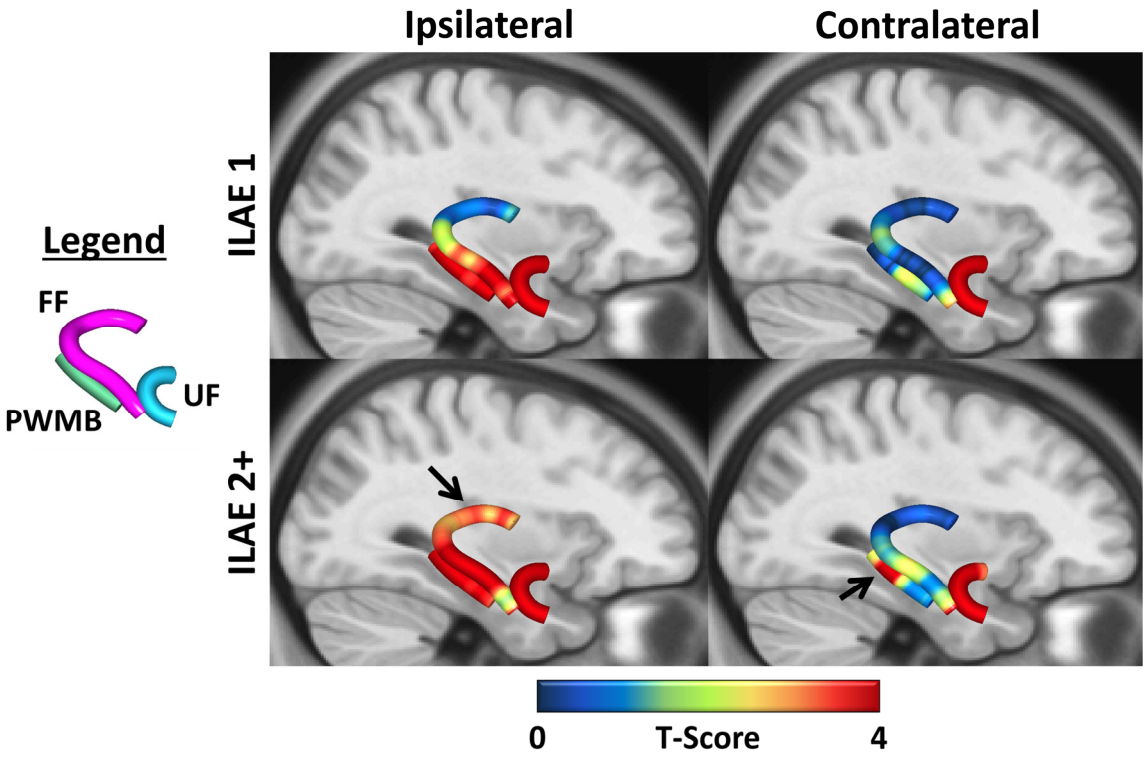

Figure 25. Section-wise t-scores for MD tract profiles. Differences between patient groups and controls are shown projected onto an anatomical template to illustrate the localisation of alterations in Figure 24. Red areas represent significantly increased MD in respective patient groups relative to controls. Arrows indicate regions significantly different only in patients with a suboptimal outcome.

Table 4. Summary Statistics for Tract Profiles

Fornix

	Param	ROI	Control	ILAE-1	ILAE-2+	ILAE-1 vs Control		ILAE-2+ vs Control	
						d	p	d	p
Ipsilateral	**MD (μm^2 / ms)**	1	1.16 (0.30)	1.22 (0.27)	1.43 (0.31)	0.19	0.601	0.89	**0.003**
		2	1.39 (0.34)	1.46 (0.29)	1.67 (0.37)	0.22	0.537	0.83	**0.005**
		3	1.07 (0.25)	1.19 (0.19)	1.32 (0.28)	0.49	0.114	0.97	**0.001**
		4	1.05 (0.15)	1.22 (0.19)	1.34 (0.26)	1.00	**0.001**	1.58	**<0.001**
		5	1.14 (0.22)	1.43 (0.18)	1.37 (0.29)	1.37	**<0.001**	0.98	**0.001**
	FA	1	0.22 (0.05)	0.22 (0.04)	0.19 (0.06)	-0.06	0.893	-0.57	0.065
		2	0.16 (0.04)	0.16 (0.04)	0.15 (0.05)	0.02	0.955	-0.34	0.303
		3	0.28 (0.08)	0.28 (0.06)	0.26 (0.09)	-0.04	0.916	-0.19	0.601
		4	0.26 (0.06)	0.26 (0.07)	0.24 (0.08)	0.05	0.906	-0.32	0.332
		5	0.20 (0.05)	0.17 (0.03)	0.18 (0.06)	-0.74	**0.013**	-0.36	0.285
Contralateral	**MD (μm^2 / ms)**	1	1.16 (0.30)	1.15 (0.34)	1.20 (0.38)	-0.05	0.906	0.11	0.800
		2	1.39 (0.34)	1.42 (0.44)	1.41 (0.35)	0.11	0.800	0.07	0.886
		3	1.07 (0.25)	1.16 (0.26)	1.14 (0.35)	0.34	0.299	0.25	0.462
		4	1.05 (0.15)	1.06 (0.16)	1.15 (0.28)	0.07	0.891	0.53	0.087
		5	1.14 (0.22)	1.22 (0.22)	1.26 (0.28)	0.39	0.239	0.54	0.082
	FA	1	0.22 (0.05)	0.23 (0.05)	0.22 (0.06)	0.28	0.400	0.06	0.891
		2	0.16 (0.04)	0.16 (0.04)	0.16 (0.05)	0.02	0.955	-0.02	0.955
		3	0.28 (0.08)	0.27 (0.07)	0.29 (0.09)	-0.06	0.891	0.14	0.730
		4	0.26 (0.06)	0.27 (0.05)	0.28 (0.08)	0.25	0.455	0.30	0.364
		5	0.20 (0.05)	0.21 (0.04)	0.20 (0.05)	0.12	0.780	0.02	0.955

Parahippocampal White Matter Bundle

	Param	ROI	Control	ILAE-1	ILAE-2+	ILAE-1 vs Control		ILAE-2+ vs Control	
						d	p	d	p
Ipsilateral	**MD (μm^2 / ms)**	1	0.98 (0.13)	1.14 (0.21)	1.19 (0.26)	1.02	**<0.001**	1.25	**<0.001**
		2	0.94 (0.10)	1.14 (0.22)	1.18 (0.25)	1.53	**<0.001**	1.66	**<0.001**
		3	0.99 (0.16)	1.19 (0.29)	1.19 (0.23)	1.04	**<0.001**	1.15	**<0.001**
		4	1.02 (0.20)	1.24 (0.36)	1.22 (0.23)	0.92	**0.001**	0.96	**0.001**
		5	1.07 (0.23)	1.40 (0.40)	1.30 (0.29)	1.20	**<0.001**	0.92	**0.001**
	FA	1	0.22 (0.06)	0.19 (0.05)	0.21 (0.07)	-0.56	**0.046**	-0.26	0.414

		2	0.26 (0.06)	0.21 (0.06)	0.23 (0.06)	-0.89	**0.001**	-0.49	0.089
		3	0.23 (0.05)	0.20 (0.06)	0.20 (0.05)	-0.52	0.069	-0.40	0.193
		4	0.19 (0.05)	0.17 (0.05)	0.17 (0.05)	-0.40	0.183	-0.32	0.299
		5	0.15 (0.04)	0.12 (0.04)	0.14 (0.05)	-0.68	**0.014**	-0.23	0.459
Contralateral	**MD (μm^2 / ms)**	1	0.98 (0.13)	0.99 (0.13)	1.08 (0.19)	0.01	0.955	0.66	**0.019**
		2	0.94 (0.10)	0.95 (0.12)	1.08 (0.19)	0.08	0.854	1.15	**<0.001**
		3	0.99 (0.16)	0.92 (0.13)	1.11 (0.23)	-0.43	0.137	0.72	**0.010**
		4	1.02 (0.20)	0.93 (0.15)	1.07 (0.24)	-0.46	0.114	0.24	0.455
		5	1.07 (0.23)	1.01 (0.19)	1.13 (0.29)	-0.31	0.310	0.25	0.444
	FA	1	0.22 (0.06)	0.22 (0.05)	0.21 (0.07)	-0.13	0.735	-0.16	0.646
		2	0.26 (0.06)	0.26 (0.06)	0.23 (0.07)	-0.03	0.953	-0.55	0.057
		3	0.23 (0.05)	0.25 (0.06)	0.21 (0.06)	0.38	0.205	-0.32	0.299
		4	0.19 (0.05)	0.21 (0.05)	0.20 (0.06)	0.48	0.090	0.30	0.319
		5	0.15 (0.04)	0.16 (0.04)	0.16 (0.05)	0.10	0.800	0.09	0.826

Uncinate Fasiculus

	Param	ROI	Control	ILAE-1	ILAE-2+	ILAE-1 vs Control		ILAE-2+ vs Control	
						d	p	D	p
Ipsilateral	**MD (μm^2 / ms)**	1	0.76 (0.07)	0.86 (0.05)	0.86 (0.07)	1.51	**<0.001**	1.53	**<0.001**
		2	0.73 (0.06)	0.85 (0.09)	0.81 (0.05)	1.82	**<0.001**	1.47	**<0.001**
		3	0.76 (0.05)	0.90 (0.11)	0.88 (0.08)	2.08	**<0.001**	2.05	**<0.001**
		4	0.76 (0.07)	0.95 (0.12)	0.93 (0.07)	2.27	**<0.001**	2.50	**<0.001**
		5	0.77 (0.08)	0.97 (0.11)	0.96 (0.07)		**<0.001**	2.41	**<0.001**
	FA	1	0.39 (0.06)	0.35 (0.06)	0.35 (0.05)	-0.66	**0.016**	-0.71	**0.011**
		2	0.42 (0.05)	0.36 (0.07)	0.39 (0.05)	-1.12	**<0.001**	-0.59	**0.038**
		3	0.33 (0.04)	0.30 (0.05)	0.31 (0.04)	-0.90	**0.001**	-0.73	**0.009**
		4	0.29 (0.05)	0.26 (0.05)	0.25 (0.04)	-0.53	0.064	-0.79	**0.005**
		5	0.26 (0.04)	0.25 (0.04)	0.23 (0.04)	-0.32	0.299	-0.78	**0.005**
Contralateral	**MD (μm^2 / ms)**	1	0.76 (0.07)	0.84 (0.06)	0.82 (0.05)	1.24	**<0.001**	0.96	**0.001**
		2	0.73 (0.06)	0.81 (0.07)	0.80 (0.05)	1.40	**<0.001**	1.34	**<0.001**
		3	0.76 (0.05)	0.85 (0.05)	0.85 (0.04)	1.85	**<0.001**	1.72	**<0.001**
		4	0.76 (0.07)	0.86 (0.05)	0.87 (0.07)	1.52	**<0.001**	1.62	**<0.001**
		5	0.77 (0.08)	0.87 (0.05)	0.90 (0.09)	1.31	**<0.001**	1.57	**<0.001**

FA	1	0.39 (0.06)	0.37 (0.08)	0.38 (0.04)	-0.34	0.275	-0.15	0.668
	2	0.42 (0.05)	0.40 (0.06)	0.39 (0.05)	-0.37	0.239	-0.56	0.059
	3	0.33 (0.04)	0.33 (0.04)	0.33 (0.04)	-0.09	0.815	-0.05	0.901
	4	0.29 (0.05)	0.27 (0.04)	0.28 (0.05)	-0.33	0.290	-0.16	0.648
	5	0.26 (0.04)	0.25 (0.05)	0.25 (0.05)	-0.33	0.293	-0.23	0.479

Note. ROIs correspond to those in Figure , values are mean (and SD), d is Cohen's-d parameter, and p is p-value. P-values are corrected for multiple comparisons with FDR and bold font indicates corrected p-values less than 0.05.

ROC curves and outcome prediction

ROC curves for selected ROIs are shown in Figure 26. The ipsilateral and contralateral UF (Figure 26 A,E) demonstrated excellent separation between patient and control groups with area under the curve (AUC) values of 0.97 and 0.90, respectively. The ipsilateral FF and PWMB (Figure 26 B,F) demonstrated acceptable separation between patient and control groups with AUC values of 0.84 and 0.82, respectively. The contralateral PWMB also demonstrated acceptable separation between patient outcome groups with an AUC value of 0.81 (Figure 26 G), and the ipsilateral FF demonstrated fair separation between outcome groups with an AUC value of 0.71 (Figure 26 C). Sensitivity and specificity were both increased when combining MD data from the ipsilateral FF and contralateral PWMB for the separation of outcome groups (Figure 27).

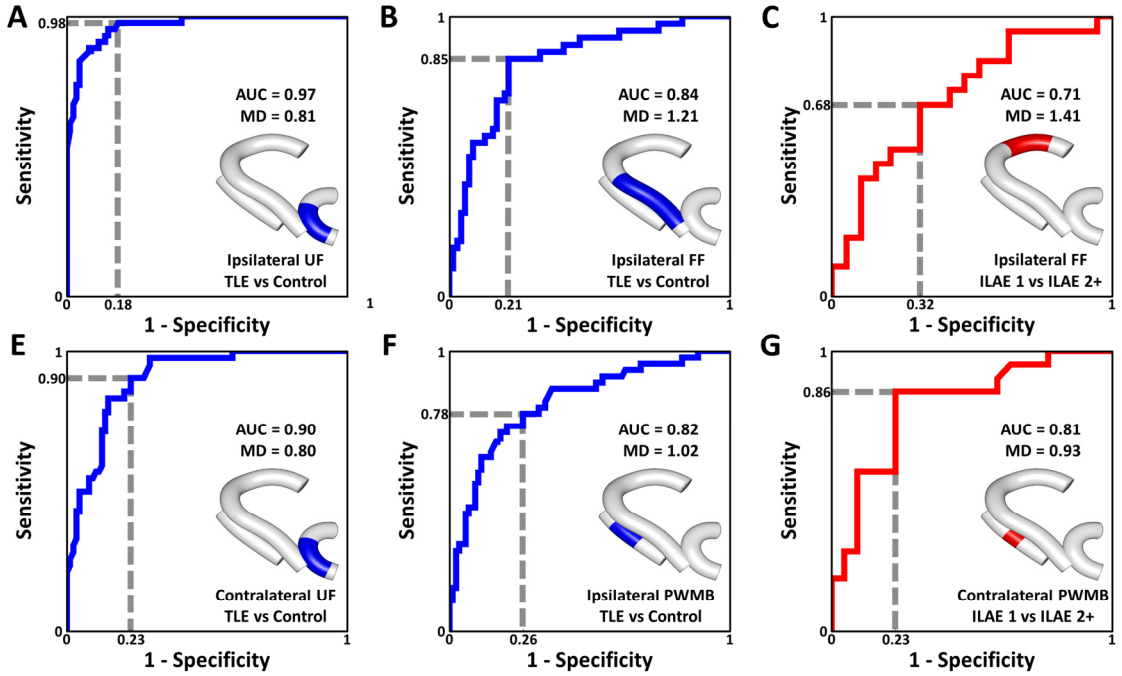

Figure 26. ROC curves. In all cases, blue indicates separation between patient and control groups and red indicates separation between patient outcome groups. AUC is used to assess quality of the ROC curves and the dashed line gives example sensitivity and 1-specificity calculations. The MD value indicates the corresponding MD threshold in units of ($\mu m^2/ms$). The inset for each curve indicates the location of the ROI used to calculate the ROC curve, which was selected based on observed group differences in MD.

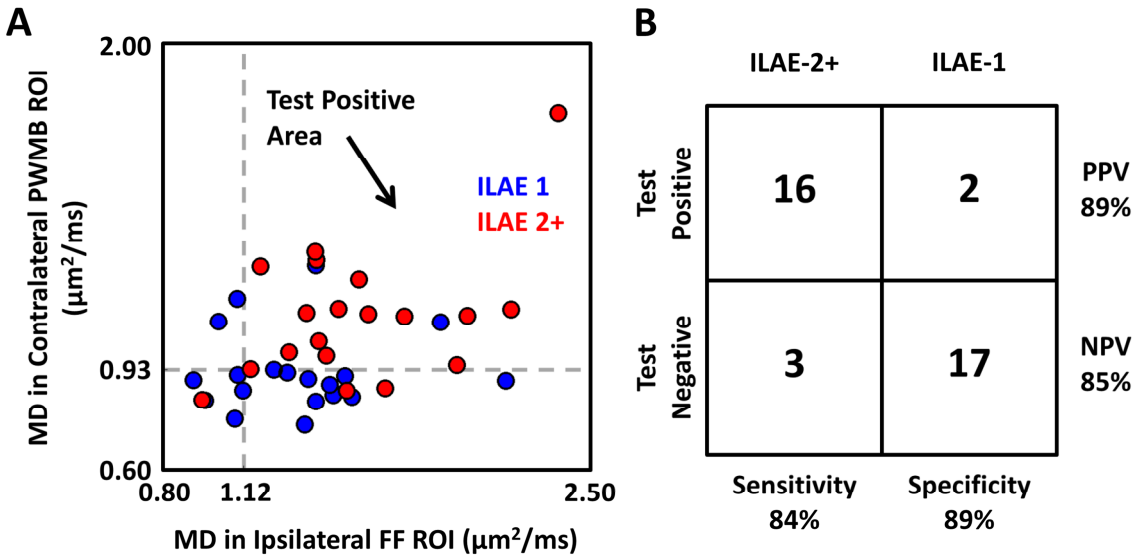

Figure 27. Combining ipsilateral dorsal fornix and contralateral PWMB MD values increases the sensitivity and specificity for separating patient outcome groups. (A) MD values in the ipsilateral dorsal fornix and contralateral PWMB are plotted on the x- and y-axes, respectively, for all patients in the ILAE 1 group (blue) and ILAE 2 group (red) using the ROIs indicated for the respective tracts in Figure 4C/G. A combined test was used to separate groups for patients with MD > 1.12 μm^2/ms in the ipsilateral fornix and MD > 0.93 μm^2/ms in the contralateral PWMB, indicated by the grey dashed lines with positive test values occurring in the upper right-hand quadrant (black arrow). (B) Sensitivity, specificity, positive predictive value (PPV), and negative predictive value (NPV) indicate reasonable test performance, illustrating the potential clinical applicability for surgical outcome prediction.

Extent of tract resection

Of the 33 patients with postoperative structural imaging, 17 (51.5%) patients were rendered seizure free (ILAE 1) while 16 (48.5%) patients experienced persistent postoperative symptoms. Resection maps are shown in Figure 28. Exemplary tractography and resection data are given in Figure 6A, which illustrates the intersections between fiber bundles and resected tissue volume. Section-wise resection maps for the ILAE 1 and ILAE 2+ groups are given in Figure 28 C-D, respectively. These maps indicate a high probability of anterior FF and PWMB resection, and low

probability of posterior FF and PWMB resection, across all patients. However, outcome group ILAE 1 had high probability of UF resection, whereas group ILAE 2+ had a lower probability of UF resection. Representative transverse and coronal image slices of the left sided fiber bundle distributions for the control group are given in Figure 28 E, demonstrating the anatomical location of the reconstructed fiber bundles. In Figure 28 F-G, voxel-wise resection maps for the reconstructed fiber bundles are indicated for ILAE 1 and ILAE 2+ groups. The location of the image slices are indicated by the black bars in Figure 28 B.

For quantitative analysis, the ILAE 1 group had non-significant increases in the extent of resected FF and PWMB relative to the ILAE 2+ group (FF: 20.8 ± 12.6%, 18.3 ± 8.9%; p=0.54; PWMB: 44.8 ± 27.2%, 33.2 ± 16.8%; p=0.23). However, there was a significantly increased proportion of UF resection in the ILAE 1 group relative to the ILAE 2+ group (41.7 ± 20.9%, 19.7 ± 23.1%; p=0.02). For individual UF resections, 1 of 17 patients in the ILAE 1 group had proportions of UF resection less than 0.15 and 9 of 16 patients in the ILAE 2 group had proportions of UF resection less than 0.15 giving sensitivity and specificity of 56% and 94%, respectively, for identifying the ILAE 2 group based on proportion of UF resection.

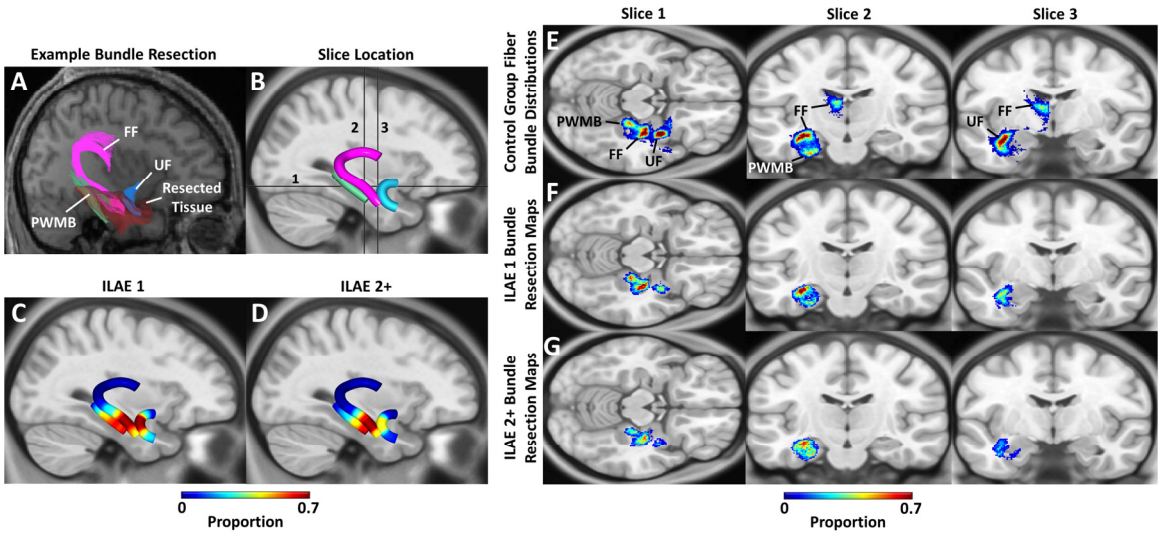

Figure 28. Fiber bundle resection analysis. (A) Representative tractography data and resection volume overlaid on an individual patient's T1-weighted image illustrate the fiber bundles of interest overlapping with the resected tissue volume in circumscribed regions along each tract. (C-D) Section-wise representation of the extent of resected fiber bundles for the ILAE 1 and ILAE 2+ groups, respectively, indicate the region of these tracts typically resected. (E) Representative slices for the fiber bundle distributions of the reconstructed tracts in the control group illustrate the anatomical location of the fiber bundles of interest. (F-G) Fiber bundle resection maps for the ILAE 1 and ILAE 2+ groups, respectively illustrate the proportion of the fiber bundles resected. The location of the representative transverse and coronal slices are given by the black bars in (B).

Discussion

The primary objective of the present study was to determine preoperative imaging correlates of postoperative seizure outcome in patients with refractory TLE using a novel DTI technique sensitive to the regional tissue characteristics of temporal lobe white matter tract bundles. We report that whilst all patients with TLE show evidence of diffusion abnormalities of the FF, PWMB and UF, only patients with persistent postoperative seizures have circumscribed alterations in two principal regions that are not observed in patients with an excellent postoperative outcome: the dorsal segment of the ipsilateral FF and the contralateral PWMB.

Furthermore, we observe that whilst MD of the UF was considerably affected in both patient outcome groups – and could be used to reliably classify patients from controls using ROC curves – the extent of resection of this tract bundle was also significantly related to postoperative outcome. We separate discussion of these findings according to the three tract bundles investigated, before highlighting pertinent methodological issues.

Fimbria-Fornix

DTI studies of patients with TLE frequently reveal diffusion abnormalities of the FF, particularly in patients with HS (160-162). In a novel imaging-histological correlational study, it was reported that preoperative diffusion abnormalities of the FF is significantly related to increased extra-axonal fraction, and reduced cumulative axonal membrane circumference and myelin area of the surgically resected tissue (160), thus indicating that *in-vivo* diffusion alterations in TLE have a histopathological basis. Myelin pathology has also been implicated in FF DTI alterations in animal models of TLE (183). In animal studies, excision of the FF causing denervation of the hippocampus from subcortical (principally thalamic) targets results in hippocampal seizure activity (184), a concomitant loss of hippocampal neurons (185) and increased hippocampal N-methyl-D-aspartate receptor density (186), which may reflect a pathological regenerative process that supports the development of limbic epileptogenicity. There is consequently an accumulation of human and animal data providing support for the hypothesis that the FF has an important role in temporal lobe seizures.

Our data indicate that the FF is equally pathological in mesial temporal lobe regions typically resected in patients who later experience postoperative seizure freedom and those with persistent postoperative seizures. However, only patients who continue to experience persistent

postoperative seizures show clear circumscribed diffusion abnormalities in fornical regions outside the margins of resection, principally in dorsal regions proximal to the thalamus. This is consistent with previous work that indicated that patients with TLE and persistent postoperative seizures had posterior mesial temporal lobe atrophy outside the margins of resection compared to patients who were rendered seizure free (137). Furthermore, it was recently reported that a suboptimal postoperative seizure outcome was related to altered tissue diffusion characteristics of probabilistic hippocampothalamic pathways, which included the posterior fornical route (148). Probabilistic seed-target tractography, like the approach employed by Keller et al. (148), does not offer the anatomical specificity that AFQ can provide. The present study has refined the nature of hippocampothalamic pathology in patients with suboptimal postoperative outcomes. The FF is the principal connector between the posterior mesial temporal lobe and thalamus (187) and mediates resting-state functional connectivity between the hippocampus and thalamus (188). Fornical abnormalities may therefore in part explain previously reported relationships between thalamotemporal alterations and persistent postoperative seizures in refractory TLE (147,148).

Parahippocampal bundle

The parahippocampal gyrus, particularly the anterior entorhinal and perirhinal regions, play an important role in the generation and propagation of temporal lobe seizures (189-192). Parahippocampal diffusion alterations have been reported in patients with TLE using DTI techniques (163-166). In the present study, we report that tissue characteristics of the ipsilateral PMWB are similarly affected in patients with excellent and suboptimal postoperative outcomes, but diffusion alterations of a circumscribed region of the contralateral PMWB was only identified in patients with persistent seizures. This suggests the possibility of a bi-temporal seizure disorder in some patients with persistent postoperative seizures. Other imaging studies

have suggested contralateral mesial temporal alterations in patients with persistent postoperative seizures (137,141,147,148), although parahippocampal involvement was not specified. Detailed electrophysiological investigations of postoperative seizures in patients with TLE and HS suggested that 25% of patients have seizure onset in the contralateral temporal lobe (142). When contralateral PWMB and ipsilateral dorsal fornical MD measures were combined, we were able to classify postoperative outcome groups with an 84% sensitivity and 89% specificity. A bihemispheric mesial temporal-subcortical epileptogenic network may therefore have significance for persistent postoperative seizures in patients with TLE.

Uncinate fasciculus

We did not find any preoperative UF differences between outcome groups; the ipsilateral and contralateral UF were affected equally across groups, and throughout the length of the uncinate. A previous study has reported MD alterations throughout the entire length of the uncinate in patients with TLE (193). Several studies report diffusion alterations of the UF in patients with TLE (165,167,168). The UF plays an important role in seizure propagation from the temporal lobe to the frontal lobe in patients with TLE as evidenced in electrophysiological studies (194,195), and reflected in studies showing interictal hypometabolism in insular-frontal-opercular regions (196-198). We did, however, identify that patients who were rendered seizure free had significantly larger resections of the UF relative to those rendered seizure free. This is a new finding that is compatible with the idea of improved disconnection of anterior epileptogenic networks in patients with TLE and an excellent outcome. It has been suggested that anterior temporal lobe regions are epileptogenic in patients with mesial TLE, and resection of the anterior temporal lobe is associated with an improved outcome (199). However, whether anterior

temporal lobectomy provides consistently improved postoperative seizure outcomes relative to amygdalohippocampectomy is a contentious issue. A review of the literature has indicated that the extent of resection does not necessarily lead to improved postoperative seizure outcome, that patients with significant hippocampal and amygdalaoid remnants may experience excellent postoperative seizure outcomes, and that amygdalohippocampectomy and anterior temporal lobectomy do not differ in rates of seizure freedom (200). In the present study, we have provided important new information indicating that *what* the resection encompasses is more important than the overall extent of resection, with resection of the UF in particular being an important factor.

Methodological issues

There are three methodological issues that warrant discussion. Firstly, although our sample is one of the largest to date that has investigated the relationship between preoperative DTI and postoperative seizure outcome (148,155-157,201), it is small in context of epidemiological studies of outcome, and therefore caution should be exercised when interpreting the relationship between clinical data and outcomes. We do report a significant effect of sex on outcome, with males being more likely to attain complete seizure freedom compared to females, which is consistent with other larger epidemiological studies (202,203). A restricted sample size also affects the generalizability of our results with respect to whether presurgical diffusion abnormalities are sufficient to predict outcome or whether outcomes would be improved by adjusting the surgical margins to include a significant proportion of the UF. However, we have demonstrated the sensitivity of AFQ for detecting individual diffusion abnormalities and the potential relevance of these specific structural alterations, which may represent a significant step forward in the clinical translation of advanced neuroimaging techniques for predicting surgical

outcomes in TLE. Secondly, because of the limited sample size, it was necessary to side flip imaging data to increase outcome group sample size. Therefore, we were unable to investigate whether the side of seizure onset was related to tract characteristics and outcome. Finally, the ultimate goal of this kind of work is to develop prognostic markers that could translate into clinical practice. DTI sequences suitable for sophisticated tractography are currently not considered clinical MRI sequences that should be routinely incorporated into preoperative evaluation of patients with refractory TLE, principally because of demands on acquisition time, and time and expertise required for image post-processing. However, we have showcased the potential predictive clinical utility of determining regional tract alterations ahead of surgery and endorse automated quantitative diffusion approaches ahead of surgery.

Conclusion

The reasons underlying persistent postoperative seizures in patients with refractory TLE are likely to be multifactorial and vary between patients. In the present study, we have identified three important factors that contribute to persistent postoperative seizures: (i) diffusion abnormalities of the ipsilateral dorsal fornix outside the margins of resection, (ii) diffusion abnormalities of the contralateral PWMB, and (iii) insufficient resection of the UF. These results hold promise as imaging prognostic markers of postoperative outcome and may provide mechanistic explanations for why some patients with TLE continue to experience postoperative seizures.

7

Abnormalities Along White Matter Pathways in Epilepsy

Temporal lobe epilepsy (TLE) is a disorder associated with structural white matter changes. In the preceding chapters, we have demonstrated compelling advantages of DKI over DTI for assessment of tissue microstructure and the translational potential for along-the-tract quantitative analyses for surgical outcomes potential in refractory TLE. In this chapter, we will adapt along-the-tract tissue characterization to DKI data and explore structural brain changes TLE. This chapter is based on the following peer-reviewed publication:

1. **Glenn GR**, Jensen JH, Helpern JA, Spampinato MV, Kuzniecky R, Keller SS, Bonilha L. Epilepsy-related cytoarchitectonic abnormalities along white matter pathways. *J. Neurol. Neurosurg. Psychiatry*. [Epub ahead of print].

Abstract

Temporal lobe epilepsy (TLE) is one of the most common forms of epilepsy. Unfortunately, the clinical outcomes of TLE cannot be determined based only on current diagnostic modalities. A better understanding of white matter connectivity changes in TLE may aid the identification of network abnormalities associated with TLE and the phenotypic characterization of the disease. In

this chapter, we implemented a novel approach for characterizing microstructural changes along white matter pathways using diffusional kurtosis imaging (DKI). Along-the-tract measures were compared for 32 subjects with left TLE and 36 age- and gender-matched controls along the left and right fimbria-fornix (FF), parahippocampal white matter bundle (PWMB), arcuate fasciculus (AF), inferior longitudinal fasciculus (ILF), uncinate fasciculus, and cingulum bundle (CB). Limbic pathways were investigated in relation to seizure burden and control with anti-epileptic drugs. By evaluating measures along each tract, it was possible to identify abnormalities localized to specific tract sub-regions. Compared with healthy controls, subjects with TLE demonstrated pathological changes in circumscribed regions of the FF, PWMB, UF, AF and ILF. Several of these abnormalities were detected only by kurtosis-based and not by diffusivity-based measures. Structural white matter changes correlated with seizure burden in the bilateral PWMB and cingulum. DKI improves the characterization of network abnormalities associated with TLE by revealing connectivity abnormalities that are not disclosed by other modalities. Since TLE is a neuronal network disorder, DKI may be well suited to fully assess structural network abnormalities related to epilepsy and thus serve as a tool for phenotypic characterization of epilepsy.

Introduction

Temporal lobe epilepsy (TLE) is the most common form of medically intractable focal epilepsy and is frequently associated with hippocampal sclerosis (HS) (204). Despite that hippocampal pathology is generally considered the primary seizure generator and principal node in a temporal epileptiform network in TLE (205), there is a sizeable literature indicating that structural abnormalities extend beyond the medial temporal lobe. Many studies have reported gray matter atrophy, white matter loss, and gliosis affecting extra-hippocampal and extra-temporal regions

(154,162,206,207). Crucially, the distribution of tissue damage in TLE is not random, but follows an anatomical and functional pattern whereby the most affected regions are those directly or indirectly associated with the medial temporal lobe and the limbic system (208-210). This regular distribution of damage implies that a limited number of common pathophysiological mechanisms are responsible for brain injury in TLE. In particular, gray matter loss may be caused by cellular excitoxicity along the limbic path of seizure spread, or by deafferentation injury from loss of neural connectivity (211).

However, the full extent of microstructural brain damage in TLE is still incompletely understood, and most patients with TLE demonstrate some degree of extra-hippocampal abnormality (212). Importantly, seizure control after pharmacological and surgical intervention can vary significantly among patients with TLE, and there are clearly distinct phenotypes of TLE when it comes to treatment responsiveness. For this reason, it is fundamentally important to accurately assess *in vivo* patterns of brain injury in TLE, with special emphasis to cytoarchitectonic features of tissue damage and their anatomical distribution.

Previous studies have investigated alterations in white matter pathways in TLE using diffusion tensor tractography (161,163,166). However, these studies predominantly utilize whole-tract analyses, which are limited as pathological changes may be concentrated in anatomically specific regions and whole-tract analyses may obstruct the detection of focal pathology. Moreover, diffusion tensor imaging (DTI) is incapable of detecting multiple, intra-voxel fiber bundle orientations in complex neurological tissue, which limits its potential for tractography (32,81). Diffusional kurtosis imaging (DKI) extends conventional DTI by estimating both the diffusion and kurtosis tensors to quantify restricted, non-Gaussian diffusion that occurs in

biological tissues (29,30). Accordingly, DKI has demonstrated improved sensitivity for detecting neuropathology in a variety of conditions including epilepsy (213-216), stroke (59,94,96,97), Alzheimer's disease (55,56,98), and numerous others (75). More recently, the advantages of DKI have been leveraged to provide more comprehensive assessment of diffusion in complex neural environments, including the characterization of diffusion anisotropy beyond the conventional fractional anisotropy (FA) (79) and computation of DKI-based white matter tractography, enabling the resolution of multiple intra-voxel fiber bundles (32,104). These advantages are improved by utilizing DKI in conjunction with automated fiber quantification (AFQ) (158), for characterization of tissue microstructure along white matter pathways, by incorporating a more comprehensive and potentially more sensitive collection of parameters for detecting disease-related pathology than does DTI. Thus, DKI is remarkably synergistic with AFQ, and the combination of the two form a particularly effective imaging method for detecting pathological white matter changes.

In this present study, we applied a novel neuroimaging approach combining the strengths of DKI and AFQ for the non-invasive characterization of pathological white matter changes in TLE. We hypothesize that cytoarchitectural abnormalities follow a crescendo gradient towards the temporal lobe with pathological effects concentrated in particular white matter regions, revealing patterns of neuroarchitectural pathology associated with TLE potentially underlying distinct phenotypical subtypes.

Methods

Subjects

This study was approved by the Institutional Review Board at the Medical University of South Carolina (MUSC). We evaluated data from 32 consecutive subjects with left TLE who were followed at the Comprehensive Epilepsy Center at MUSC. All subjects were diagnosed with left TLE in concordance with the diagnostic criteria proposed by the International League Against Epilepsy (ILAE), including a comprehensive medical history, a full neurological evaluation, and epileptiform discharges on interictal EEG, with the majority of subjects demonstrating neuroradiological evidence of HS (217). The mean (± std) age of all subjects was 44.8 (± 16.7) years, and included 10 males and 22 females. A control group of 36 age and gender matched healthy individuals with no history of neurological problems was also recruited from the local community. Control subjects had a mean (± std) age of 40.4 (± 11.6) years, including 12 males and 24 females. Clinical and demographic information for the subjects with TLE included in this study are further described Table 3. The subjects included in this study are also described in a previous study from our group using voxel-based methods without tractography (22).

Table 5. Demographic and Clinical Information for Subjects with TLE

Patient Number	Gender	Age (yr)	Age of Epilepsy Onset (yr)	Durration (yr)	Seizure Frequency (per 6 Mo)	MRI Results	Interictal EEG
1	F	57	52	5	3	Normal	Left tIEDs
2	F	57	35	22	24	Left HS	Left tIEDs
3	F	63	57	6	1	Normal	Left tIEDs
4	M	46	3	43	12	Left HS	Left tIEDs
5	M	56	30	26	6	Left HS	Left tIEDs
6	F	18	3	15	72	Left HS	Left tIEDs
7	F	37	33	4	6	Left HS	Left tIEDs
8	F	51	50	1	12	Normal	Left tIEDs
9	F	23	17	6	6	Left HS	Left and right tIEDs
10	M	22	10	12	0.5	Left HS	Left tIEDs
11	F	21	20	1	1	Left HS	Left tIEDs
12	M	34	15	19	1	Normal	Left tIEDs
13	F	58	55	3	1	Left HS	Left tIEDs

14	M	20	20	0	0.2	Left HS	Left and right tIEDs
15	F	67	66	1	6	Normal	Left tIEDs
16	F	62	62	0	0.2	Left HS	Left tIEDs
17	F	57	1	56	2	Left HS	Normal
18	F	18	5	13	3	Left HS	Left tIEDs
19	F	37	28	9	2	Left HS	Normal
20	F	20	19	1	1	Left HS	Normal
21	F	57	50	7	6	Left HS	Left and right tIEDs
22	F	45	33	12	2	Left HS	Normal
23	M	43	0	43	3	Left HS	Normal
24	F	76	30	46	6	Left HS	Left tIEDs
25	M	36	17	19	1	Left HS	Normal
26	M	65	59	6	1	Left HS	Normal
27	F	57	2	55	6	Left HS	Left tIEDs
28	M	45	27	18	2	Left HS	Normal
29	F	27	27	0	0.2	Left HS	Normal
30	F	59	42	17	3	Left HS	Left tIEDs
31	F	46	35	11	0.5	Left HS	Left tIEDs
32	M	40	37	3	0.2	Left HS	Normal

Note: HS, hippocampal sclerosis; EEG, electroencephalography; tIED, temporal interictal epileptiform discharges; in cases where left and right tIEDs were noted, left tIEDs were greater than right tIEDs and signs of unilateral left HS were present on MRI.

Our cohort contained subjects with varying disease severity including subjects with recently diagnosed TLE and subjects whose seizures were well controlled with anti-epileptic drugs (AEDs). Thus subjects in this cohort were not all surgical candidates. Subjects well controlled on AEDs were identified by having one or fewer seizures per six months (n = 13), and subjects not well controlled on AEDs were identified by having more than one seizure per six months (n = 19).

Image Acquisition

DKI datasets were acquired with a 3 Tesla Magnetom Verio MRI scanner (Siemens Medical, Erlangen, Germany) using a vendor-supplied, single-shot diffusion-weighted EPI sequence with a twice-refocused spin echo (65) and a 12-channel head coil. To characterize non-Gaussian diffusion, the protocol included 3 diffusion weightings of b = 0, 1000, and 2000 s/mm^2, with 30

isotropically distributed diffusion encoding directions and a total of 10 images with no diffusion weighting (b=0). Other acquisition parameters were: repetition time (TR) = 8500 ms, echo time (TE) = 98 ms, voxel dimensions = 3.0×3.0×3.0 mm^3, matrix size × number of slices = 74×74×40, and a parallel imaging factor = 2 with no partial Fourier encoding. The acquisition time for this protocol was 9 minutes and 12 seconds. Structural imaging was also performed for each participant using a sagittal T1-weighted magnetization-prepared rapid acquisition gradient echo (MPRAGE) image sequence, with TR/TE = 2250/4.18 ms, inversion time = 900 ms, voxel dimensions = 1.0×1.0×1.0 mm^3, and matrix size × number of slices = 256×256×176.

Image Analysis

DKI analysis included the estimation of the diffusion and kurtosis tensors (52) and subsequent DKI-derived tractography (32,104) and was performed using diffusional kurtosis estimator (DKE) software (https://www.nitrc.org/projects/dke/). Quantitative tensor analyses included characterization of mean diffusivity (MD) and FA from the diffusion tensor and corresponding mean kurtosis (MK) (52) and kurtosis fractional anisotropy (KFA) (79). DKI was incorporated into the AFQ image processing pipeline (https://github.com/jyeatman/AFQ) using fully automated in-house scripts written in MATLAB (MathWorks, Natick, MA, USA).

AFQ utilizes diffusion tractography data and performs a series of automated steps to identify and segment specific white matter fiber bundles and isolate the core of each tract (158). Fiber bundles are selected by specifying regions of interest (ROIs) chosen from a white matter template, which are applied to define the extremities of each tract. Once the core of a tract is identified, AFQ interpolates a fixed number of sections along the tract and estimates the diffusion and kurtosis tensors at every section, enabling reconstruction of all tensor-derived metrics. By

using each subject's unique tractography data, this approach can potentially accommodate more inter-subject variability in tract locations than alternative voxel-based methods. Tract profiles were excluded in cases where AFQ did not identify individual tracts (159).

Beyond the conventional AFQ pipeline, we implemented in-house algorithms to automatically segment the fimbria-fornix (FF) white matter fibers, in addition to the standard fiber groups used by AFQ. This was done as hippocampal sclerosis is a common pathological feature of TLE and the FF represents a major conduit of information to and from the hippocampus. Additional white matter pathways were selected based on their hypothesized role in TLE, and include the parahippocampal white matter bundle (PWMB), arcuate fasciculus (AF), inferior longitudinal fasciculus (ILF), cingulum bundle (CB) and uncinate fasciculus (UF). A summary of the image analysis steps for a single subject is given in Figure 29.

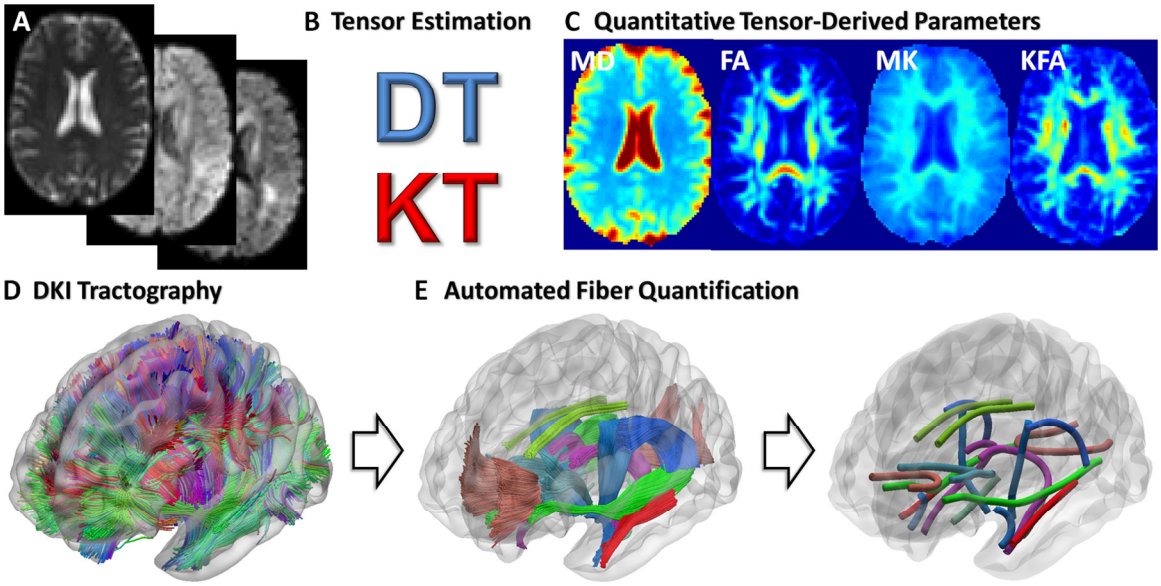

Figure 29. AFQ with DKI. (A) DKI uses multiple diffusion weighting b-values and diffusion encoding directions to characterize non-Gaussian diffusion which occurs in vivo. The images shown include an average b=0 image along with images with diffusion weightings of b = 1000 and b = 2000 s/mm^2 for a single diffusion-encoding direction. (B) Images in the DKI dataset are combined to estimate the diffusion tensor (DT) and kurtosis tensor (KT), which characterize the 3D intra-voxel diffusion dynamics based on physical properties of water diffusion. (C) The diffusion and kurtosis tensors are then analyzed to generate scalar, quantative parameter maps that can be used to characterize tissue microstructure. (D) The diffusion and kurtosis tensors are combined to perform DKI-based tractography, which can improve tractography relative to DTI by enabling the resolution of multiple intra-voxel fiber bundles in complex neural tissue. (E) AFQ performs a series of automated steps to segment fiber groups from standardized white matter ROIs and then isolates each fiber group's tract core for analysis of the diffusion parameters. Each subject generates tract profiles for each diffusion metric along each tract core, which can be compared to investigate individual and group-wise differences.

The effects of seizure burden and seizure control with AEDs were tested in the PWMB and CB, as these limbic pathways are crucial for the progression of disease (161), neuropsychological manifestations of TLE (163), and differentiation of TLE subtypes by treatment response including surgical outcomes (149,218) and pharmacoresistance (219). Seizure burden was defined as equal to $\log_{10}(frequency \times duration)$, with the logarithm being applied to accommodate

subjects with very high seizure frequency, and the effects were assessed using Pearson's product-moment correlation coefficient.

Tractography

DKI tractography was performed using the closed-form analytical expression of the kurtosis orientation distribution function derived by Jensen et al. (32) and the image analysis procedures developed by Glenn et al. (104) using the DKE tractography module (https://www.nitrc.org/projects/dke/). Whole brain masks were calculated within AFQ using FSL's brain extraction tool (178), and DKI-based tractography was performed using the Euler method with an angle cutoff threshold of 35 degrees, a minimum tract length threshold of 20 mm, and 250,000 seed points randomly placed within each subject's brain mask.

Statistical Analysis

Tract profiles were created for each fiber group using AFQ along 100 sections by interpolating the DKI-derived diffusion and kurtosis tensors along each tract and then quantifying the tensor-derived parameters for each section. Each tract was then divided into 5 regions of interest (ROIs), consisting of 20 consecutive sections. The respective along-the-tract diffusion metrics were averaged over each ROI and a two sample t-test was performed to determine the significance of group-wise differences. In all, there were a total of 12 fiber groups × 4 diffusion metrics × 5 regions of interest per fiber group, resulting in 240 total comparisons. Significance levels were corrected for multiple comparisons using the false discovery rate (FDR) procedure (180). To quantify the effect size of the observed changes, the Cohen's d parameter was calculated for each ROI for group-wise differences as well as differences between subjects whose seizures were well-controlled with AEDs and those whose seizures were not well-controlled with AEDs. For

correlations with seizure burden, statistical significance was corrected for multiple comparisons with FDR, and the effects of pharmacoresistance were tested using the well-controlled and not well-controlled groups using a two sample t-test. Cohen's d parameter was used to quantify the effect size. The ROIs used in this study are illustrated in Figure 30.

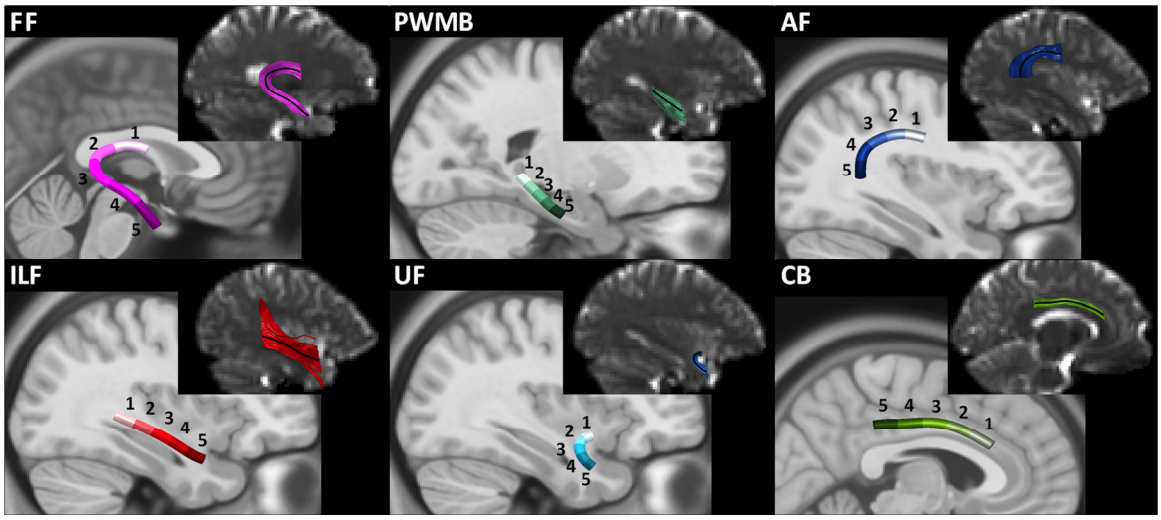

Figure 30. The location of white matter ROIs is defined from the reconstructed fiber tracts. The insert for each fiber group in the upper right-hand corner illustrates white matter tracts identified by AFQ and DKI for a single subject, overlaid on the corresponding b=0 image. The solid black line indicates the core of each tract used in generating the individual tract profiles. Tract cores identified for all subjects in this study are averaged and overlaid on an anatomical MRI template to illustrate the group-wise representation of each fiber group. Each fiber group is divided into 5 ROIs with increasing ROI numbers indicating regionally-specific locations in each tract. The ROIs in this figure correspond to the ROIs used in the tables included in this study.

Results

Group-wise tract profiles for all fiber groups are shown in Figure 31. The tract profiles demonstrate similar along-the-tract variation of the diffusion metrics between subjects and controls and between the ipsilateral and contralateral hemispheres. Importantly, these results demonstrate that epilepsy-related abnormalities can be restricted to specific regions of each tract,

which would be undetected by methods that group all data from one tract into a single value. The results in Figure 31 are tabulated in Table 6.

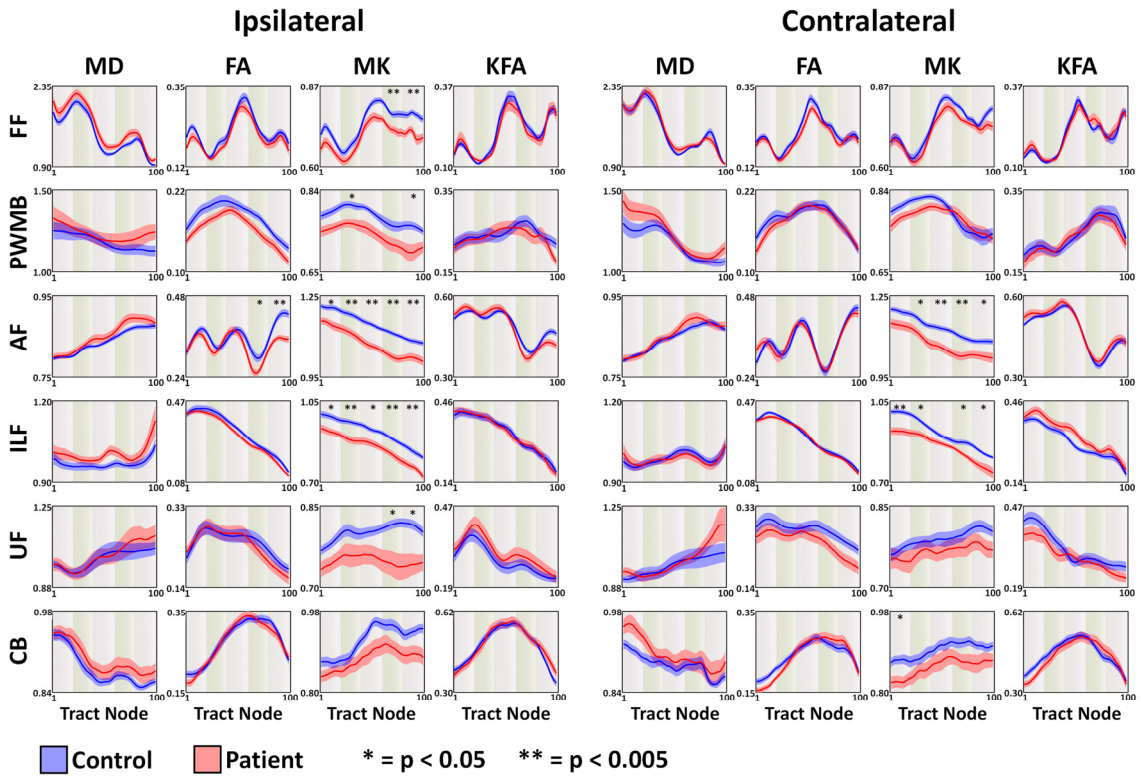

Figure 31. Mean tract profiles (± sem) for ipsilateral and contralateral fiber groups demonstrate regional group-wise differences in diffusion metrics between subjects and controls. Group-wise differences are tested over bins indicated by the green and purple bars and summary statistics for group-wise comparisons are given in the online supplemental material. Comparisons marked with an asterisk (*) have p-values < 0.05, and a double asterisk (**) indicates p-values < 0.005, after correction the significance level for multiple comparisons using FDR. The vertical bins correspond to the ROIs illustrated in Figure 2 with increasing ROI number corresponding to increasing Tract Section number. The MD is in units of $\mu m^2/ms$, while the remaining parameters are dimensionless.

Table 6. Tract Profile Summary Statistics

Fimbria-Fornix

		Left				Right			
Param	**ROI**	**Control**	**Patient**	**d**	**p**	**Control**	**Patient**	**d**	**p**
	1	1.81 (0.34)	1.98 (0.46)	-0.42	0.332	1.99 (0.37)	1.98 (0.52)	0.01	0.976
	2	1.91 (0.34)	2.05 (0.40)	-0.38	0.407	1.97 (0.42)	2.04 (0.45)	-0.17	0.744
MD	3	1.22 (0.25)	1.37 (0.39)	-0.45	0.283	1.24 (0.22)	1.30 (0.34)	-0.24	0.631
	4	1.27 (0.18)	1.40 (0.31)	-0.50	0.212	1.28 (0.17)	1.30 (0.23)	-0.12	0.832
	5	1.15 (0.18)	1.23 (0.25)	-0.36	0.426	1.29 (0.28)	1.22 (0.24)	0.29	0.565
	1	0.20 (0.04)	0.19 (0.05)	0.42	0.338	0.19 (0.04)	0.18 (0.05)	0.12	0.829
	2	0.18 (0.05)	0.16 (0.04)	0.32	0.510	0.17 (0.04)	0.16 (0.04)	0.26	0.589
FA	3	0.28 (0.07)	0.26 (0.07)	0.27	0.594	0.28 (0.06)	0.25 (0.06)	0.46	0.276
	4	0.24 (0.04)	0.22 (0.05)	0.34	0.448	0.24 (0.05)	0.23 (0.05)	0.27	0.593
	5	0.21 (0.04)	0.19 (0.07)	0.25	0.619	0.20 (0.05)	0.20 (0.05)	0.11	0.822
	1	0.71 (0.08)	0.66 (0.09)	0.59	0.116	0.68 (0.08)	0.68 (0.10)	0.07	0.920
	2	0.69 (0.08)	0.65 (0.08)	0.44	0.311	0.68 (0.09)	0.65 (0.09)	0.24	0.630
MK	3	0.82 (0.06)	0.77 (0.09)	0.70	0.055	0.83 (0.07)	0.79 (0.09)	0.40	0.388
	4	**0.80 (0.06)**	**0.74 (0.07)**	**1.00**	**<0.005**	0.81 (0.05)	0.78 (0.06)	0.51	0.194
	5	**0.79 (0.05)**	**0.72 (0.07)**	**1.22**	**<0.005**	0.78 (0.06)	0.75 (0.09)	0.45	0.281
	1	0.15 (0.04)	0.16 (0.09)	-0.16	0.772	0.14 (0.04)	0.15 (0.06)	-0.26	0.603
	2	0.13 (0.04)	0.13 (0.04)	0.09	0.877	0.14 (0.04)	0.14 (0.05)	0.05	0.930
KFA	3	0.30 (0.10)	0.27 (0.11)	0.24	0.622	0.28 (0.08)	0.26 (0.08)	0.18	0.745
	4	0.25 (0.06)	0.23 (0.07)	0.24	0.628	0.23 (0.06)	0.24 (0.08)	-0.16	0.765
	5	0.25 (0.07)	0.24 (0.08)	0.05	0.932	0.23 (0.08)	0.23 (0.08)	-0.09	0.882

Parahippocampal White Matter Bundle

		Left				Right			
Param	**ROI**	**Control**	**Patient**	**d**	**p**	**Control**	**Patient**	**d**	**p**
	1	1.25 (0.29)	1.30 (0.34)	-0.17	0.753	1.26 (0.28)	1.38 (0.32)	-0.40	0.383
	2	1.23 (0.21)	1.24 (0.24)	-0.07	0.922	1.28 (0.20)	1.34 (0.26)	-0.29	0.571
MD	3	1.18 (0.18)	1.20 (0.25)	-0.09	0.872	1.20 (0.16)	1.21 (0.21)	-0.06	0.929
	4	1.14 (0.18)	1.19 (0.29)	-0.23	0.633	1.08 (0.13)	1.10 (0.18)	-0.14	0.790
	5	1.14 (0.19)	1.23 (0.30)	-0.38	0.400	1.06 (0.15)	1.11 (0.19)	-0.27	0.589
	1	0.18 (0.05)	0.16 (0.03)	0.48	0.229	0.17 (0.05)	0.15 (0.04)	0.36	0.432
	2	0.20 (0.05)	0.18 (0.03)	0.45	0.288	0.18 (0.04)	0.18 (0.04)	0.09	0.874
FA	3	0.20 (0.04)	0.18 (0.03)	0.36	0.420	0.20 (0.04)	0.20 (0.04)	-0.02	0.980
	4	0.18 (0.03)	0.16 (0.04)	0.62	0.092	0.19 (0.04)	0.19 (0.04)	0.09	0.880
	5	0.15 (0.03)	0.13 (0.04)	0.48	0.234	0.15 (0.03)	0.16 (0.04)	-0.01	0.980
	1	0.79 (0.06)	0.75 (0.06)	0.66	0.066	0.80 (0.05)	0.77 (0.06)	0.51	0.205
	2	**0.80 (0.05)**	**0.76 (0.06)**	**0.81**	**0.018**	0.82 (0.04)	0.79 (0.05)	0.61	0.108
MK	3	0.79 (0.05)	0.74 (0.08)	0.67	0.064	0.81 (0.04)	0.80 (0.05)	0.31	0.520
	4	0.76 (0.07)	0.72 (0.09)	0.57	0.127	0.76 (0.08)	0.77 (0.08)	-0.20	0.712
	5	**0.75 (0.05)**	**0.70 (0.10)**	**0.71**	**0.045**	0.74 (0.09)	0.74 (0.08)	-0.04	0.947
	1	1.26 (0.28)	1.38 (0.32)	-0.40	0.383	0.21 (0.09)	0.20 (0.09)	0.13	0.811
	2	1.28 (0.20)	1.34 (0.26)	-0.29	0.571	0.20 (0.07)	0.21 (0.08)	-0.04	0.949
KFA	3	1.20 (0.16)	1.21 (0.21)	-0.06	0.929	0.24 (0.08)	0.24 (0.08)	-0.09	0.874
	4	1.08 (0.13)	1.10 (0.18)	-0.14	0.790	0.29 (0.11)	0.28 (0.09)	0.06	0.931
	5	1.06 (0.15)	1.11 (0.19)	-0.27	0.589	0.28 (0.10)	0.26 (0.09)	0.20	0.709

Arcuate Fasciculus

		Left				Right			
Param	**ROI**	**Control**	**Patient**	**d**	**p**	**Control**	**Patient**	**d**	**p**
	1	0.80 (0.02)	0.80 (0.05)	-0.11	0.821	0.80 (0.03)	0.80 (0.05)	0.03	0.969
	2	0.82 (0.03)	0.83 (0.05)	-0.24	0.625	0.83 (0.04)	0.83 (0.05)	-0.11	0.826
MD	3	0.84 (0.03)	0.85 (0.06)	-0.28	0.572	0.85 (0.03)	0.86 (0.06)	-0.17	0.750
	4	0.86 (0.03)	0.89 (0.06)	-0.44	0.284	0.88 (0.04)	0.89 (0.07)	-0.32	0.490
	5	0.88 (0.04)	0.89 (0.06)	-0.34	0.445	0.88 (0.04)	0.88 (0.06)	-0.02	0.979
	1	0.36 (0.05)	0.35 (0.06)	0.17	0.746	0.33 (0.06)	0.33 (0.08)	-0.07	0.923
	2	0.34 (0.06)	0.33 (0.05)	0.16	0.752	0.33 (0.07)	0.34 (0.06)	-0.12	0.811
FA	3	0.37 (0.06)	0.36 (0.07)	0.17	0.751	0.38 (0.06)	0.37 (0.05)	0.14	0.793
	4	**0.31 (0.06)**	**0.28 (0.05)**	**0.76**	**0.026**	0.29 (0.06)	0.28 (0.05)	0.03	0.961
	5	**0.41 (0.06)**	**0.35 (0.04)**	**1.12**	**<0.005**	0.41 (0.06)	0.40 (0.06)	0.15	0.785
	1	**1.20 (0.06)**	**1.15 (0.08)**	**0.83**	**0.016**	1.19 (0.06)	1.14 (0.10)	0.62	0.094
	2	**1.18 (0.06)**	**1.11 (0.08)**	**0.95**	**<0.005**	**1.16 (0.06)**	**1.10 (0.09)**	**0.73**	**0.038**
MK	3	**1.14 (0.05)**	**1.07 (0.08)**	**1.21**	**<0.005**	**1.13 (0.06)**	**1.06 (0.09)**	**0.96**	**<0.005**
	4	**1.11 (0.05)**	**1.03 (0.08)**	**1.36**	**<0.005**	**1.10 (0.06)**	**1.03 (0.09)**	**0.96**	**<0.005**
	5	**1.09 (0.05)**	**1.02 (0.09)**	**0.94**	**<0.005**	**1.08 (0.06)**	**1.03 (0.09)**	**0.75**	**0.031**
	1	0.54 (0.04)	0.55 (0.07)	-0.24	0.625	0.52 (0.04)	0.53 (0.08)	-0.26	0.587
	2	0.53 (0.04)	0.54 (0.07)	-0.23	0.641	0.54 (0.04)	0.56 (0.08)	-0.23	0.638
KFA	3	0.53 (0.05)	0.53 (0.08)	0.02	0.971	0.52 (0.05)	0.52 (0.07)	0.00	0.997
	4	0.42 (0.05)	0.39 (0.07)	0.44	0.284	0.37 (0.06)	0.38 (0.07)	-0.16	0.758
	5	0.45 (0.06)	0.42 (0.07)	0.48	0.236	0.42 (0.06)	0.43 (0.09)	-0.18	0.748

Inferior Longitudinal Fasciculus

		Left				Right			
Param	**ROI**	**Control**	**Patient**	**d**	**p**	**Control**	**Patient**	**d**	**p**
	1	0.97 (0.10)	1.00 (0.12)	-0.31	0.514	0.96 (0.09)	0.97 (0.13)	-0.11	0.821
	2	0.96 (0.09)	0.98 (0.08)	-0.29	0.569	0.97 (0.08)	0.98 (0.09)	-0.05	0.932
MD	3	0.96 (0.06)	1.00 (0.08)	-0.56	0.135	1.00 (0.07)	0.99 (0.09)	0.16	0.756
	4	0.96 (0.06)	0.99 (0.10)	-0.36	0.422	1.00 (0.07)	0.99 (0.10)	0.18	0.745
	5	0.99 (0.09)	1.04 (0.18)	-0.38	0.409	0.99 (0.11)	0.98 (0.12)	0.04	0.949
	1	0.43 (0.10)	0.42 (0.06)	0.14	0.793	0.40 (0.05)	0.39 (0.05)	0.32	0.494
	2	0.41 (0.08)	0.39 (0.06)	0.29	0.562	0.37 (0.05)	0.37 (0.05)	0.15	0.789
FA	3	0.33 (0.07)	0.31 (0.06)	0.42	0.328	0.29 (0.06)	0.30 (0.05)	-0.18	0.749
	4	0.25 (0.06)	0.24 (0.06)	0.26	0.591	0.23 (0.06)	0.22 (0.05)	0.14	0.787
	5	0.18 (0.07)	0.16 (0.05)	0.37	0.409	0.17 (0.06)	0.16 (0.06)	0.16	0.761
	1	**0.98 (0.08)**	**0.92 (0.09)**	**0.79**	**0.021**	**1.00 (0.06)**	**0.92 (0.09)**	**1.09**	**<0.005**
	2	**0.96 (0.06)**	**0.88 (0.09)**	**0.97**	**<0.005**	**0.96 (0.05)**	**0.90 (0.08)**	**0.90**	**0.007**
MK	3	**0.93 (0.06)**	**0.86 (0.09)**	**0.87**	**0.010**	0.90 (0.06)	0.86 (0.06)	0.58	0.116
	4	**0.88 (0.06)**	**0.82 (0.08)**	**0.98**	**<0.005**	**0.87 (0.06)**	**0.82 (0.05)**	**0.81**	**0.018**
	5	**0.83 (0.07)**	**0.76 (0.08)**	**1.00**	**<0.005**	**0.83 (0.05)**	**0.76 (0.11)**	**0.78**	**0.023**
	1	0.41 (0.10)	0.42 (0.08)	-0.07	0.924	0.38 (0.06)	0.41 (0.09)	-0.38	0.405
	2	0.39 (0.08)	0.39 (0.09)	-0.02	0.975	0.34 (0.07)	0.37 (0.09)	-0.34	0.445
KFA	3	0.35 (0.08)	0.34 (0.08)	0.14	0.798	0.28 (0.06)	0.33 (0.09)	-0.66	0.065
	4	0.28 (0.07)	0.29 (0.09)	-0.06	0.925	0.25 (0.05)	0.27 (0.07)	-0.35	0.431
	5	0.22 (0.09)	0.22 (0.09)	0.08	0.907	0.22 (0.08)	0.24 (0.11)	-0.17	0.748

Cingulum Bundle

		Left				Right			
Param	**ROI**	**Control**	**Patient**	**d**	**p**	**Control**	**Patient**	**d**	**p**
	1	0.93 (0.05)	0.94 (0.06)	-0.14	0.797	0.91 (0.05)	0.95 (0.08)	-0.59	0.112
	2	0.89 (0.05)	0.91 (0.08)	-0.30	0.525	0.89 (0.05)	0.91 (0.08)	-0.27	0.589
MD	3	0.86 (0.04)	0.88 (0.07)	-0.30	0.541	0.88 (0.06)	0.90 (0.08)	-0.20	0.679
	4	0.87 (0.04)	0.88 (0.08)	-0.29	0.564	0.89 (0.06)	0.89 (0.10)	-0.06	0.928
	5	0.85 (0.03)	0.87 (0.07)	-0.35	0.429	0.86 (0.04)	0.88 (0.11)	-0.21	0.668
	1	0.20 (0.05)	0.19 (0.05)	0.16	0.770	0.19 (0.04)	0.17 (0.03)	0.65	0.072
	2	0.26 (0.06)	0.26 (0.07)	0.00	0.996	0.23 (0.04)	0.22 (0.05)	0.26	0.595
FA	3	0.31 (0.05)	0.32 (0.07)	-0.13	0.789	0.27 (0.05)	0.27 (0.07)	-0.04	0.951
	4	0.33 (0.05)	0.33 (0.07)	0.07	0.924	0.27 (0.05)	0.28 (0.07)	-0.19	0.714
	5	0.29 (0.05)	0.28 (0.06)	0.14	0.793	0.24 (0.06)	0.25 (0.07)	-0.14	0.801
	1	0.87 (0.06)	0.84 (0.07)	0.37	0.407	**0.87 (0.06)**	**0.82 (0.07)**	**0.70**	**0.050**
	2	0.89 (0.07)	0.86 (0.09)	0.36	0.431	0.88 (0.07)	0.85 (0.09)	0.39	0.383
MK	3	0.94 (0.06)	0.89 (0.11)	0.59	0.112	0.90 (0.07)	0.87 (0.11)	0.37	0.409
	4	0.94 (0.07)	0.90 (0.10)	0.55	0.139	0.91 (0.06)	0.87 (0.09)	0.52	0.184
	5	0.93 (0.06)	0.88 (0.10)	0.61	0.095	0.90 (0.05)	0.87 (0.10)	0.45	0.284
	1	0.41 (0.07)	0.40 (0.09)	0.15	0.771	0.40 (0.07)	0.36 (0.07)	0.53	0.163
	2	0.51 (0.08)	0.50 (0.11)	0.02	0.970	0.47 (0.07)	0.45 (0.11)	0.23	0.622
KFA	3	0.56 (0.07)	0.57 (0.11)	-0.08	0.904	0.52 (0.08)	0.51 (0.11)	0.12	0.832
	4	0.53 (0.06)	0.53 (0.11)	0.00	0.998	0.47 (0.08)	0.49 (0.12)	-0.18	0.749
	5	0.41 (0.06)	0.44 (0.11)	-0.35	0.430	0.40 (0.08)	0.41 (0.12)	-0.11	0.828

Uncinate Fasciculus

		Left				Right			
Param	**ROI**	**Control**	**Patient**	**d**	**p**	**Control**	**Patient**	**d**	**p**
	1	0.96 (0.08)	0.97 (0.14)	-0.02	0.970	0.93 (0.12)	0.94 (0.10)	-0.14	0.806
	2	0.96 (0.16)	0.96 (0.17)	-0.01	0.990	0.95 (0.17)	0.94 (0.10)	0.07	0.919
MD	3	1.03 (0.24)	1.02 (0.19)	0.04	0.945	0.99 (0.22)	0.98 (0.09)	0.07	0.923
	4	1.04 (0.23)	1.07 (0.27)	-0.10	0.875	1.01 (0.26)	1.03 (0.13)	-0.07	0.920
	5	1.05 (0.18)	1.10 (0.26)	-0.24	0.637	1.03 (0.26)	1.13 (0.28)	-0.37	0.432
	1	0.25 (0.09)	0.26 (0.08)	-0.04	0.951	0.29 (0.09)	0.27 (0.09)	0.29	0.578
	2	0.27 (0.08)	0.27 (0.09)	-0.04	0.946	0.28 (0.08)	0.26 (0.07)	0.24	0.633
FA	3	0.26 (0.09)	0.26 (0.09)	-0.04	0.952	0.28 (0.08)	0.26 (0.08)	0.21	0.706
	4	0.25 (0.08)	0.23 (0.08)	0.24	0.635	0.27 (0.08)	0.24 (0.07)	0.43	0.348
	5	0.20 (0.07)	0.18 (0.07)	0.30	0.572	0.24 (0.06)	0.20 (0.08)	0.62	0.119
	1	0.78 (0.05)	0.74 (0.07)	0.62	0.123	0.77 (0.06)	0.75 (0.10)	0.25	0.623
	2	0.80 (0.06)	0.76 (0.10)	0.53	0.222	0.78 (0.06)	0.76 (0.09)	0.26	0.632
MK	3	0.80 (0.05)	0.76 (0.09)	0.65	0.109	0.79 (0.08)	0.77 (0.08)	0.28	0.591
	4	**0.81 (0.05)**	**0.74 (0.12)**	**0.85**	**0.023**	0.80 (0.07)	0.77 (0.09)	0.30	0.568
	5	**0.81 (0.05)**	**0.74 (0.10)**	**0.95**	**0.011**	0.81 (0.06)	0.78 (0.08)	0.48	0.286
	1	0.34 (0.12)	0.36 (0.12)	-0.16	0.784	0.42 (0.13)	0.37 (0.12)	0.40	0.400
	2	0.33 (0.12)	0.36 (0.13)	-0.30	0.583	0.35 (0.12)	0.32 (0.10)	0.33	0.502
KFA	3	0.26 (0.11)	0.29 (0.11)	-0.27	0.601	0.29 (0.10)	0.29 (0.11)	-0.05	0.948
	4	0.26 (0.10)	0.29 (0.13)	-0.26	0.629	0.28 (0.11)	0.27 (0.10)	0.13	0.808
	5	0.23 (0.08)	0.25 (0.12)	-0.19	0.747	0.26 (0.09)	0.23 (0.09)	0.34	0.498

Note: ROI locations correspond to those illustrated in Figure 30. Control and Patient values represent mean (± sandard deviation). d = Cohen's d parameter and p = p-value after correcting for multiple comparisons with FDR. Statistically significant differences are indicated by bold font for $p < 0.05$.

In general, MD is higher in subjects with TLE relative to controls in all ROIs and all fiber groups with the exception of one ipsilateral ROI (ROI 3 in the UF) and eight contralateral ROIs (ROI 1 and 5 in the FF, ROI 1 in the AF, ROI 2 and 3 in the UF, and ROIs 3-5 in the right ILF), although the observed changes were not found to be statistically significant. FA tended to be lower in subjects with TLE relative to controls, with statisitically significant reductions being found in ROIs 4 and 5 of the ipsilateral AF.

MK demonstrated significant reduction in the ipsilateral FF, PWMB, and UF in multiple ROIs. In the ipsilateral FF and UF, this reduction was more pronounced with increasing ROI number (further anteriorly within the temporal lobe). MK showed statistically significant reductions in all ROIs in the bilateral AF and ILF, except for ROI 1 in the contralateral AF and ROI 3 in the contralateral ILF, with the ipsilateral side tending to demonstrate a stronger effect size.

The location and relative significance of the observed differences are illustrated in the section-wise t-score plots in Figure 4. Qualitatively, the abnormal t-scores demonstrated a crescendo effect increasing in significance into the temporal lobe. Similar to the tract profiles, the section-wise t-score plots demonstrated a slight, but general increase in MD and decrease in FA in subjects relative to controls. With MK, the changes can be seen bilaterally, with the effect being the largest within the ipsilateral temporal lobe.

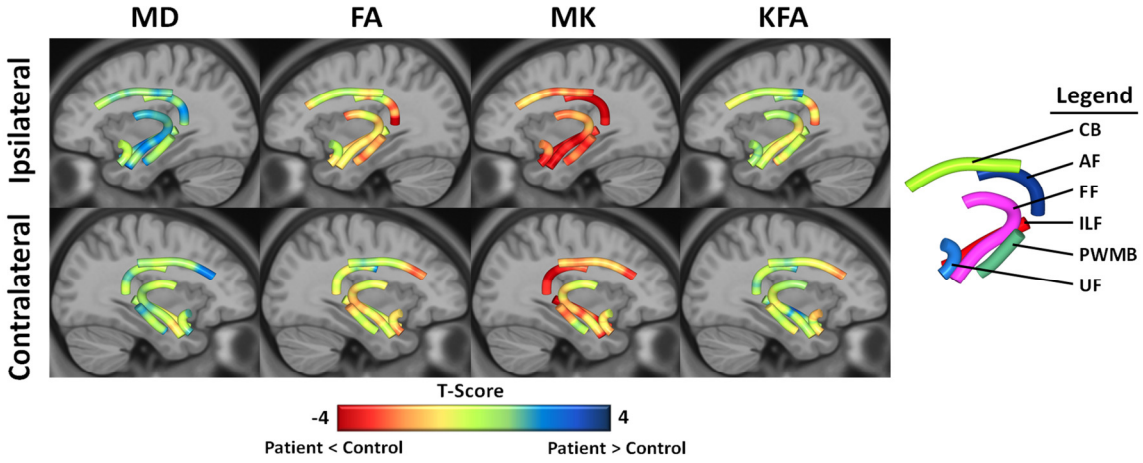

Figure 32. Section-wise t-score plots summarize the observed differences in the tract profiles. Section wise t-scores are calculated from the tract profiles illustrated in Figure 31. These are overlaid on a white matter template at positions indicated by the average of the tract-cores for all participants included in this study. Section-wise t-scores provide a visual representation of where pathological changes occur, with dark red indicating greater group-wise reductions in the subject versus control groups and dark blue indicating greater group-wise increases in the subjects versus control group.

Correlations with seizure burden are illustrated in Table 7. Significant correlations were found in the PWMB and CB with MD demonstrating significant correlations on the ipsilateral hemisphere and MK and KFA demonstrating bilateral limbic effects. In the ipsilateral PWMB, significant correlations were found for MD, MK, and KFA in ROI 3, with the correlations extending further along the tract anteriorly and posteriorly with MD and KFA. In the ipsilateral CB, significant correlations were found in ROI 5 for MD, ROIs 2-5 for MK, and all ROIs for KFA. On the contralateral side, significant correlations with MK were found in ROI 3 of the PWMB and ROIs 2-5 of the CB, and with KFA in ROI 3 and 4 of the PWMB and ROI 5 of the CB.

Table 7. Correlations with Seizure Burden

Param	ROI	Parahippocampal White Matter Bundle				Cingulum Bundle			
		Ipsilateral		Contralateral		Ipsilateral		Contralateral	
		r	p	r	p	r	p	r	p
MD	1	0.272	0.196	0.310	0.150	0.336	0.126	0.099	0.622
	2	**0.442**	**0.038**	0.279	0.197	0.314	0.140	0.187	0.364
	3	**0.602**	**0.007**	0.342	0.129	0.316	0.138	0.176	0.390
	4	**0.532**	**0.017**	0.386	0.083	**0.386**	**0.075**	0.261	0.209
	5	**0.457**	**0.036**	0.277	0.197	**0.446**	**0.037**	0.331	0.132
FA	1	-0.122	0.547	-0.089	0.665	-0.212	0.305	-0.060	0.765
	2	-0.214	0.304	-0.166	0.430	-0.284	0.178	-0.003	0.986
	3	-0.246	0.238	-0.285	0.192	-0.338	0.127	0.024	0.908
	4	-0.202	0.329	-0.130	0.542	**-0.358**	**0.098**	-0.219	0.296
	5	0.138	0.502	-0.190	0.369	-0.303	0.150	-0.390	0.073
MK	1	0.120	0.549	0.174	0.408	0.415	0.054	0.394	0.071
	2	0.325	0.132	0.204	0.339	**0.518**	**0.019**	**0.566**	**0.010**
	3	**0.484**	**0.027**	**0.436**	**0.050**	**0.454**	**0.035**	**0.592**	**0.007**
	4	0.397	0.070	0.396	0.076	**0.456**	**0.035**	**0.477**	**0.029**
	5	0.233	0.262	0.329	0.142	**0.489**	**0.026**	**0.504**	**0.022**
KFA	1	-0.258	0.212	-0.253	0.236	**-0.465**	**0.034**	-0.317	0.140
	2	**-0.459**	**0.036**	-0.336	0.135	**-0.498**	**0.023**	-0.366	0.090
	3	**-0.623**	**0.006**	**-0.465**	**0.035**	**-0.515**	**0.019**	-0.306	0.150
	4	**-0.564**	**0.009**	**-0.452**	**0.039**	**-0.623**	**0.011**	-0.380	0.078
	5	-0.306	0.148	-0.313	0.147	**-0.582**	**0.008**	**-0.525**	**0.018**

Note: Correlations with seizure burden for the PWMB and CB indicate limbic involvement in the progression of cytocarchitectural changes in TLE. ROI numbers correspond to the ROIs depicted in Figure 30. r = Pearson's product moment correlation coefficient and p = p-value after correcting for multiple comparisons with FDR. Statistically significant correlations are indicated by bold font $p < 0.05$.

Comparisons between AED responsive and unresponsive groups are illustrated in Table 8. Uncorrected p-values less than 0.05 were found in comparing subjects well-controlled with AEDs with those poorly controlled for the ipsilateral PWMB in ROI 3 in MD and ROIs 3-4 in KFA and for the ipsilateral CB in ROI 5 in MD and all ROIs with the anisotropy parameters, FA and KFA. Uncorrected p-values less than 0.05 were also found for the contralateral CB in MK in ROI 2 and KFA in ROI 5. While none of these attained statistical significance following FDR correction, they may be indicative of trends that would warrant further investigation with a larger sample size. For example, the not well-controlled group demonstrated a 21% reduction in KFA in ROI 2

of the ipsilateral CB compared to the well-controlled group with a Cohen's d parameter of -1.262, suggesting a potentially large effect.

Table 8. AED Response

Parahippocampal White Matter Bundle

		Left				Right			
Param	**ROI**	**Control**	**Patient**	**d**	**p**	**Control**	**Patient**	**d**	**p**
	1	1.29 (0.24)	1.31 (0.41)	0.04	0.918	1.33 (0.25)	1.41 (0.36)	0.26	0.491
	2	1.19 (0.17)	1.28 (0.27)	0.35	0.343	1.30 (0.18)	1.37 (0.30)	0.26	0.489
MD	3	**1.08 (0.12)**	**1.28 (0.28)**	**0.90**	**0.019**	1.17 (0.16)	1.24 (0.24)	0.35	0.360
	4	1.07 (0.13)	1.27 (0.34)	0.73	0.050	1.08 (0.15)	1.12 (0.20)	0.24	0.529
	5	1.12 (0.19)	1.30 (0.34)	0.66	0.079	1.11 (0.18)	1.10 (0.20)	-0.05	0.898
	1	0.16 (0.03)	0.16 (0.04)	-0.15	0.680	0.16 (0.04)	0.15 (0.04)	-0.23	0.546
	2	0.19 (0.02)	0.18 (0.04)	-0.39	0.292	0.18 (0.04)	0.18 (0.04)	-0.12	0.745
FA	3	0.20 (0.03)	0.18 (0.04)	-0.54	0.147	0.20 (0.04)	0.19 (0.04)	-0.38	0.311
	4	0.17 (0.04)	0.15 (0.04)	-0.54	0.145	0.20 (0.04)	0.18 (0.03)	-0.50	0.194
	5	0.12 (0.04)	0.14 (0.04)	0.34	0.356	0.16 (0.04)	0.15 (0.04)	-0.18	0.641
	1	0.75 (0.04)	0.75 (0.07)	-0.05	0.902	0.77 (0.04)	0.78 (0.08)	0.12	0.752
	2	0.75 (0.06)	0.77 (0.06)	0.19	0.601	0.79 (0.04)	0.80 (0.06)	0.21	0.577
MK	3	0.73 (0.10)	0.76 (0.07)	0.34	0.357	0.78 (0.05)	0.81 (0.05)	0.49	0.196
	4	0.69 (0.09)	0.73 (0.09)	0.45	0.225	0.75 (0.05)	0.79 (0.09)	0.44	0.244
	5	0.67 (0.11)	0.72 (0.08)	0.60	0.104	0.73 (0.06)	0.75 (0.09)	0.25	0.503
	1	0.22 (0.08)	0.23 (0.09)	0.04	0.916	0.21 (0.09)	0.19 (0.10)	-0.23	0.537
	2	0.25 (0.08)	0.23 (0.08)	-0.30	0.421	0.22 (0.07)	0.20 (0.08)	-0.19	0.617
KFA	3	**0.30 (0.08)**	**0.23 (0.09)**	**-0.78**	**0.039**	0.26 (0.07)	0.23 (0.09)	-0.36	0.340
	4	**0.29 (0.09)**	**0.22 (0.10)**	**-0.74**	**0.049**	0.31 (0.09)	0.26 (0.09)	-0.50	0.189
	5	0.24 (0.10)	0.20 (0.08)	-0.53	0.155	0.26 (0.08)	0.26 (0.09)	0.02	0.952

Cingulum Bundle

		Left				Right			
Param	**ROI**	**Control**	**Patient**	**d**	**p**	**Control**	**Patient**	**d**	**p**
	1	0.91 (0.06)	0.96 (0.06)	0.72	0.053	0.94 (0.08)	0.95 (0.08)	0.16	0.669
	2	0.88 (0.07)	0.92 (0.08)	0.65	0.083	0.90 (0.08)	0.92 (0.07)	0.30	0.417
MD	3	0.85 (0.06)	0.89 (0.07)	0.63	0.091	0.89 (0.09)	0.90 (0.07)	0.15	0.690
	4	0.85 (0.06)	0.90 (0.09)	0.67	0.073	0.87 (0.09)	0.90 (0.10)	0.33	0.369
	5	**0.84 (0.05)**	**0.89 (0.08)**	**0.77**	**0.040**	0.84 (0.07)	0.90 (0.13)	0.58	0.118
	1	**0.21 (0.05)**	**0.18 (0.04)**	**-0.79**	**0.036**	0.17 (0.04)	0.16 (0.03)	-0.26	0.474
	2	**0.29 (0.06)**	**0.23 (0.07)**	**-1.03**	**0.007**	0.22 (0.05)	0.22 (0.05)	-0.09	0.807
FA	3	**0.36 (0.06)**	**0.29 (0.06)**	**-1.15**	**0.003**	0.27 (0.07)	0.27 (0.07)	-0.05	0.896
	4	**0.35 (0.05)**	**0.31 (0.07)**	**-0.79**	**0.036**	0.30 (0.09)	0.27 (0.06)	-0.45	0.226
	5	**0.31 (0.06)**	**0.26 (0.06)**	**-0.81**	**0.033**	0.28 (0.08)	0.23 (0.06)	-0.63	0.091
	1	0.83 (0.07)	0.85 (0.06)	0.29	0.428	0.81 (0.08)	0.83 (0.07)	0.24	0.507
MK	2	0.83 (0.09)	0.88 (0.09)	0.51	0.166	0.81 (0.08)	0.87 (0.09)	0.75	0.045
	3	0.86 (0.13)	0.91 (0.10)	0.43	0.246	0.83 (0.10)	0.90 (0.10)	0.69	0.065

	4	0.87 (0.10)	0.92 (0.09)	0.50	0.173	0.84 (0.09)	0.89 (0.10)	0.54	0.148
	5	0.86 (0.12)	0.90 (0.09)	0.44	0.228	0.83 (0.10)	0.89 (0.09)	0.63	0.090
KFA	1	**0.45 (0.08)**	**0.37 (0.08)**	**-1.03**	**0.008**	0.38 (0.06)	0.34 (0.08)	-0.55	0.136
	2	**0.57 (0.09)**	**0.45 (0.10)**	**-1.26**	**0.001**	0.49 (0.10)	0.42 (0.10)	-0.60	0.109
	3	**0.63 (0.10)**	**0.53 (0.09)**	**-1.10**	**0.005**	0.53 (0.12)	0.49 (0.10)	-0.43	0.239
	4	**0.59 (0.09)**	**0.49 (0.10)**	**-1.06**	**0.006**	0.52 (0.13)	0.47 (0.11)	-0.44	0.234
	5	**0.50 (0.11)**	**0.40 (0.09)**	**-0.93**	**0.015**	**0.46 (0.12)**	**0.37 (0.11)**	**-0.78**	**0.039**

Note: Group-wise comparisons between subjects whose seizures are well-controlled with AEDs (n = 13) and subjects whose seizures are not well-controled by AEDs (n = 19) in PWMB and CB pathways. d = Cohen's d parameter and p = p-value (uncorrected). Differences with $p < 0.05$ (uncorrected) are indicated by bold font. These may be regarded as trends, as no differences where significant after correcting for multiple comparisons.

Discussion

In this study, we employed a novel neuroimaging technique that combines DKI and AFQ for the in vivo characterization of cytoarchitectronic abnormalities in TLE along white matter pathways which are physiologically relevant for TLE. In accordance with the previous literature, we detected pathological changes in several extra-hippocampal and extra-temporal white matter tracts in subjects with TLE. Moreover, the important novel findings of this study pertain to the superior sensitivity of DKI-based tractography to identify and localize intra-pathway structural connectivity abnormalities in TLE. These observations complement our initial reports of increased sensitivity of DKI in scalar diffusion voxel-based maps of subjects with epilepsy (213). This is the first study to use DKI-based tractography combined with AFQ, demonstrating how DKI tractography can overcome limitations imposed by fiber crossing and unveil epilepsy related abnormalities. Our data indicate that group-wise reductions in MK are observed in regionally specific areas of the ipsilateral FF, UF, and PWMB, as well as more diffuse bilateral abnormalities in the ILF and AF (Figure 31). We also report significant effects of seizure burden on MD, MK, and KFA of ipsilateral limbic pathways. MK and KFA indicated additional correlations with seizure burden in contralateral pathways (Table 7). The overall salience of these

findings hinges on the technical innovations of these new forms of tractography and the critical need to better define phenotypic characterizations of subjects with epilepsy.

Technical Innovations

This is the first study to combine DKI and AFQ for the fully automated detection of cytoarchitectonic alterations along white matter fiber pathways, which may be a particularly sensitive method for assessing white matter tissue microstructure. With scalar, voxel-based data, it is not always clear which pathways are compromised. For example, an abnormal voxel in an ROI corresponding to the ILF may be related to transverse fibers in the same region. By defining which specific tracts are abnormal, one can develop a more detailed understanding of the distribution of cytoarchitectonic abnormalities. The methodological benefits of these approaches are further enhanced when augmented with along the tract measures, which not only identify the structurally compromised tracts, but additionally have the capability to localize specific abnormalities within the long axis of a tract. Moreover, the tract cores analyzed can preserve a significant amount of inter-subject anatomical tract variability while still enabling group-wise comparisons, which can help avoid normalization errors that complicate conventional voxel-wise techniques. This is further improved by utilizing DKI, which characterizes higher-order diffusion dynamics compared to DTI and can thus describe more complex diffusion profiles. Consequently, DKI enables the detection of crossing white matter fiber bundles for diffusion tractography and provides a more comprehensive collection of quantitative parameters, which may enhance the detection of disease-related abnormalities. Thus, the combination of DKI and AFQ creates an effective tool for characterizing white matter pathways, enabling further insights into patterns of neuroarchitectural pathology that occur in numerous neurological and psychiatric disorders.

Towards a phenotypic microstructural connectivity characterization of TLE

Increasingly, advanced neuroimaging techniques have demonstrated both localized and networked cytoarchitectonic abnormalities in TLE with limbic alterations potentially underlying various clinicopathological features of the disorder, including the pathological mechanisms that lead to medically intractable TLE (161), neuropsychological impairments (163), AED response (55), and surgical outcomes (149,218). In the present study, we recruited a cohort of 32 consecutive subjects diagnosed with left TLE, which was comprised of subjects with various disease severities. DKI in combination with AFQ detected pathological white matter alterations consistent with our understanding of TLE as a network disease having tissue abnormalities concentrated in the temporal lobe of the brain. Moreover, statistical trends were observed in limbic structures between subjects whose seizures were well controled with AEDs and those who had worse AED control (Table 8), which could be an important clinical prognosticator. Interestingly, KFA in the ipsilateral PWMB and CB correlated with seizure burden, and we observed trends for differences in tract characteristics between subjects who had well-controlled seizures and those who did not, despite no detectible group-wise differences in this region with normal controls. A similar trend was seen between subjects who had well-controlled seizures with AEDs and those who did not in FA in the ipsilateral CB. A possible explanation for this is that distinct mechanisms may underlie AED response compared to pharmacoresistance, with AED responders having higher than normal diffusion anisotropy and subjects whose seizures were not well controlled having lower than normal diffusion anisotropy in these limbic structures. This also supports the need for the improved sensitivity in detecting patterns of neuroarchitectural alterations in TLE afforded by DKI. Moreover, DKI detected contralateral changes in MK that were not apparent in analysis of the conventional diffusivity-based parameters of MD and FA.

This study also extends the work of Concha et al. (193), where along-the-tract measures were assessed in the ILF, AF, and UF using a manual segmentation routine with DTI in subjects with medically intractable TLE. In that work, it was argued that the changes in diffusion metrics could reflect astrogliosis and microstructural alterations related to the occurrence of seizures with potential effects of postictal vasogenic edema. In the present study, the reduction in MK reflects a net loss in the complexity of microstructural tissue compartmentalization, which is also consistent with subtle pathological denervation. By including a more comprehensive assessment of along-the-tract diffusion abnormalities, the proposed technique may provide an important step towards a better understanding of the neuroarchitectural alterations that occur in TLE, as well as the development of fully automated imaging biomarkers for the separation of TLE subtypes based on clinically important distinctions.

Limitations

By focusing this study on tract profiles within the AFQ identified tract cores and using only a subset of the possible DKI-derived diffusion metrics, we have substantially restricted the scope of our analysis. This is a potential limitation of this study, as there may be important disease-related differences missed outside of the tract cores. Moreover, the quantitative parameters employed in this study depict physical properties of water diffusion which may be differentially influenced by multiple, distinct factors (81). To address this limitation DKI-based white matter modeling techniques can be applied, which may improve the specificity of the observed changes (54). The subject cohort included in this study was comprised of individuals with left-sided TLE, as left- and right-sided TLE may have intrinsically different pathological effects on temporal lobe structures (220). Thus we were not able to assess the effects of right sided disease. In addition,

this study was comprised of individuals with varying disease severity, including recently diagnosed and chronic TLE as well as individuals whose seizures were well-controlled and not well-controlled with AEDs. Well-controlled and intractable TLE may represent distinct pathological mechanisms; so by including both groups, sensitivity may be lost in characterizing regionally specific distinctions. Nevertheless, combining DKI with AFQ revealed distinct patterns of cytoarchitectronic abnormalities, which highlights the sensitivity as well as the potential applicability of the proposed techique.

Conclusion

There are measurable differences in white matter tissue that are not routinely considered in the clinical assessment of subjects with unilateral TLE. We have described a diffusion MRI-based image analysis technique that, by combining the strengths of DKI and AFQ, can quantify cytoarchitectonic abnormalities in specific, white matter fiber pathways. The proposed technique is shown to detect group-wise pathological changes, with the largest effect sizes lateralizing to the ipsilateral temporal lobe and extending along the tracts from the ipsilateral temporal lobe and including the contralateral side of the brain. Microstructural changes are also found to correlate with seizure burden in specific limbic pathways and trends are found towards detecting differences between subjects with well-controlled and not well-controlled TLE. Combining DKI and AFQ may be a particularly effective neuroimaging technique for detecting microstructural alterations along physiologically relevant white matter pathways that could provide further insights into the variable clinical course of TLE, as well as a wide array of other neuropsychological conditions affecting the structural organization of the human brain.

8

Conclusion

DKI is an effective and versatile dMRI technique for studying the structural organization of the human brain. In this work, the capabilities of DKI have been expanded and the techniques developed have been shown to offer advantages compared to traditional DTI analyses. These advantages are afforded by estimation of the kurtosis tensor which enhances the depiction of in vivo diffusion dynamics, including additional quantitative analyses, such as mean kurtosis and kurtosis fractional anisotropy; the ability to perform kurtosis-based microstructural modeling, which can improve the specificity of dMRI to disease-related changes; and the ability to detect crossing white matter fiber bundles, which improves tractography for studying the structural connectivity of the human brain. Taken together these advantages may be leveraged to provide sensitive markers of pathology in TLE, which could augment the clinical management of patients with TLE and improve patient outcomes through improved diagnostic techniques and a better mechanistic understanding of the disorder. There remains vast potential for growth of DKI,

including better understanding of the origins of kurtosis-based microstructural changes, development of new analytical tools for detecting pathology, and further exploration into the clinical applicability of this technology in disorders of the brain and beyond. This work supplements a vibrant field of research in dMRI and has opened new avenues of exploration and discovery for the continued development of DKI and neuroimaging applications in TLE.

REFERENCES

1. Haneef Z, Stern J, Dewar S, Engel J. Referral pattern for epilepsy surgery after evidence-based recommendations: a retrospective study. *Neurology.* 2010;75:699-704.
2. Lewinsohn M, Phillipi G, Suen P, Spencer D. Are epilepsy surgery guidelines being followed? . *Neurology.* 2010;24:e41-2.
3. Stejskal EO. Use of spin echoes in a pulsed magnetic-field gradient to study restricted diffusion and flow. *J Chem Phys.* 1965;43:3597-603.
4. Stejskal EO, Tanner JE. Spin diffusion measurements: spin echoes in the presence of time-dependent field gradient. *J Chem Phys.* 1965;42:288-92.
5. Bihan DL, Iima M. Diffusion Magnetic Resonance Imaging: What Water Tells Us about Biological Tissues. *PLoS One.* 2015;23:e1002203.
6. Costa J, Fareleira F, Ascencao R, Borges M, Sampaio C, Vaz-Carneiro A. Clinical comparability of the new antiepileptic drugs in refractory partial epilepsy: a systematic review and meta-analysis. *Epilepsia.* 2011;52:1280-91.
7. Kwan P, Brodie MJ. Emerging drugs for epilepsy. *Expert Opin Emerg Drugs* 2007;12:407-22.
8. LaRoche SM, Helmers SL. The new antiepileptic drugs: scientific review. *JAMA.* 2004;291:605-14.
9. Parente A, Villani VMF, Franceschetti S, Giovagnoli AR. Investigating higher-order cognitive functions in temporal lobe epiilepsy: cognitive estimation. *Epilepsy & behavior : E&B.* 2013;29:330-6.
10. Titis AS, Mahoney JM, Testorf ME, Holmes GL, Scott RC. Cognitive impairment in temporal lobe epilepsy: Role of online and offline processing of single cell information. *Hippocampus.* 2014;24:1129-45.
11. Getz K, Hermann B, Seidenberg M, et al. Negative symptoms and psychosocial status in temporal lobe epilepsy. *Epilepsy Res.* 2003;53:240-4.
12. Tellez-Zenteno JF, Dhar R, Wiebe S. Long-term seizure outcomes following epilepsy surgery: a systematic review and meta-analysis. *Brain.* 2005;128:1188-98.
13. Tellez-Zenteno JF, Wiebe S. Long-term seizure and psychosocial outcomes of epilepsy surgery. Curr Treat Options *Neurology.* 2008;10:253-9.
14. Bell GS, Sinha S, Tisi JD, et al. Premature mortality in refractory partial epilepsy: does surgical treatment make a difference? *Journal of neurology, neurosurgery, and psychiatry.* 2010;81:716-8.
15. Sperling MR, Feldman H, Kinman J, Liporace JD, O'Connor MJ. Seizure control and mortality in epilepsy. *Ann Neurol.* 1999;46:45-50.
16. Engel J, Wiebe S, French J, et al. 2003. *Neurology.* Quality Standards Subcommittee of the American Academy of Neurology; American Epilepsy Society; American Association of Neurological Surgeons. Practice parameter: temporal lobe and localized neocortical resections for epilepsy: report of the Quality Standards Subcommittee of the American Academy of Neurology, in association with the American Epilepsy Society and the American Association of Neurological Surgeons.;60:538-47.
17. Lutz MT, Clusmann H, Elger CE, Schramm J, Helmstaedter C. Neuropsychological outcome after selective amygdalohippocampectomy with transsylvian versus transcortical approach: a randomized prospective clinical trial of surgery for temporal lobe epilepsy. *Epilepsia.* 2004;45:809-16.

18. Schramm J, Lehmann TN, Zentner J, et al. Randomized controlled trial of 2.5-cm versus 3.5-cm mesial temporal resection in temporal lobe epilepsy--Part 1: intent-to-treat analysis. *Acta Neurochir (Wien).* 2011;153:209-19.
19. Walczak TS, Radtke RA, McNamara JO, et al. Anterior temporal lobectomy for complex partial seizures: evaluation, results, and long-term follow-up in 100 cases. *Neurology.* 1990;40:413-8.
20. Wiebe S, Blume WT, Girvin JP, Eliasziw M. Effectiveness and Efficiency of Surgery for Temporal Lobe Epilepsy Study Group. A randomized, controlled trial of surgery for temporal-lobe epilepsy. *The New England journal of medicine.* 2001;345:311-8.
21. Wyler AR, Hermann BP, Somes G. Extent of medical temporal resection on outcome from anterior temporal lobectomy: A randomized prospective study. *Neurosurg.* 1995;37:982-91.
22. Bonilha L, Martz GU, Glazier SS, Edwards JC. Subtypes of medial temporal lobe epilepsy: influence on temporal lobectomy outcomes? . *Epilepsia.* 2012;53:1-6.
23. Breedlove J, Nesland T, Vandergrift WA, Betting LE, Bonilha L. Probabilistic ictal EEG sources and temporal lobe epilepsy surgical outcome. *Acta Neurol Scand.* 2014;130:103-10.
24. Heinemann U. Basic mechanisms of partial epilepsies. *Current opinion in neurology.* 2002;17:155-9.
25. MP. R. Large scale brain models of epilepsy: dynamics meets connectomics. *Journal of neurology, neurosurgery, and psychiatry.* 2012;83:1238-48.
26. O'Dell CM, Das A, Wallace G, Ray SK, Banik NL. Understanding the basic mechanisms underlying seizures in mesial temporal lobe epilepsy and possible therapeutic targets: a review. *J nNeurosci Res.* 2012;90:913-24.
27. Spencer SS. Neural networks in human epilepsy: evidence of and implications for treatment. *Epilepsia.* 2002;43:219-27.
28. Cendes F. Neuroimaging predictors of AED resistance in new-onset epilepsies. *Epilepsia.* 2011;52:7-9.
29. Jensen JH, Helpern JA, Ramani A, Lu H, Kaczynski K. Diffusional kurtosis imaging: the quantification of non-Gaussian water diffusion by means of magnetic resonance imaging. *Magn. Reson. Med.* 2005;53:1432-40.
30. Jensen JH, Helpern JA. MRI quantification of non-Gaussian water diffusion by kurtosis analysis. *NMR Biomed.* 2010;23:698-710.
31. Hansen B, Lund TE, Sangill R, Jespersen SN. Experimentally and computationally fast method for estimation of a mean kurtosis. *Magn. Reson. Med.* 2013;69:1754-60.
32. Jensen JH, Helpern JA, Tabesh A. Leading non-Gaussian corrections for diffusion orientation distribution functions. *NMR Biomed.* 2014;27:202-11.
33. Lazar M, Jensen JH, Xuan L, Helpern JA. Estimation of the orientation distribution function from diffusional kurtosis imaging. *Magn. Reson. Med.* 2008;60:774-81.
34. Aganj I, Lenglet C, Sapiro G, Yacoub E, Ugurbil K, Harel N. Reconstruction of the orientation distribution function in single- and multipleshell q-ball imaging within constant solid angle. *Magn. Reson. Med.* 2010;64:554-66.
35. Aganj I, Lenglet C, Yacoub GSE, Ugurbil K, Harel N. Multiple Q-shell ODF reconstruction in q-ball imaging. *Med. Image Comput. Assist. Interv.* 2009;12:423-31.
36. Lazar M. Mapping brain anatomical connectivity using white matter tractography. *NMR biomed.* 2010;23:821-35.
37. Tuch DS. Q-ball imaging. *Magn. Reson. Med.* 2004;52:1358-72.

38. Tuch DS, Reese TG, Wiegell MR, Wedeen VJ. Diffusion MRI of complex neural architecture. *Neuron.* 2003;40:885-95.
39. Wedeen VJ, Hagmann P, Tseng WY, Reese TG, Weisskoff RM. Mapping complex tissue architecture with diffusion spectrum magnetic resonance imaging. *Magn. Reson. Med.* 2005;54:1377-86.
40. Basser PJ, Pierpaoli C. Microstructural and physiological features of tissues elucidated by quantitative-diffusion-tensor MRI. *J. Magn. Reson. B.* 1996;111:209-19.
41. Pierpaoli C, Basser PJ. Toward a quantitative assessment of diffusion anisotropy. *Magn. Reson. Med.* 1996;36:893-906.
42. Alexander AL, Hasan KM, Lazar M, Tsuruda JS, Parker DL. Analysis of partial volume effects in diffusion-tensor MRI. *Magn. Reson. Med.* 2001;45:770-80.
43. Alexander DC, Barker GJ, Arridge SR. Detection and modeling of non-Gaussian apparent diffusion coefficient profiles in human brain data. *Magn. Reson. Med.* 2002;48:331-40.
44. Bhagat YA, Beaulieu C. Diffusion anisotropy in subcortical white matter and cortical gray matter: changes with aging and the role of CSF-suppression. *J. Magn. Reson. Imaging.* 2004;20:216-27.
45. Ma X, Kadah YM, LaConte SM, Hu X. Enhancing measured diffusion anisotropy in gray matter by eliminating CSF contamination with FLAIR. *Magn. Reson. Med.* 2004;51:423-7.
46. Szczepankiewicz F, Lätt J, Wirestam R, et al. Variability in diffusion kurtosis imaging: impact on study design, statistical power and interpretation. *Neuroimage.* 2013;76:145-54.
47. Vos SB, Jones DK, Viergever MA, Leemans A. Partial volume effect as a hidden covariate in DTI analyses. *Neuroimage.* 2011;55(1566-76).
48. Yang AW, Jensen JH, Hu CC, Tabesh A, Falangola MF, Helpern JA. Effect of cerebral spinal fluid suppression for diffusional kurtosis imaging. *J. Magn. Reson. Imaging.* 2013;37:365-71.
49. Zhang H, Schneider T, Wheeler-Kingshott CA, Alexander DC. NODDI: practical in vivo neurite orientation dispersion and density imaging of the human brain. *Neuroimage.* 2012;61:1000-16.
50. Hui ES, Cheung MM, Qi L, Wu EX. Towards better MR characterization of neural tissues using directional diffusion kurtosis analysis. *Neuroimage.* 2008;42:122-34.
51. Poot DH, Dekker AJd, Achten E, Verhoye M, Sijbers J. Optimal experimental design for diffusion kurtosis imaging. *IEEE Trans. Med. Imaging.* 2010;29:819-29.
52. Tabesh A, Jensen JH, Ardekani BA, Helpern JA. Estimation of tensors and tensor-derived measures in diffusional kurtosis imaging. *Magn. Reson. Med.* 2011;65:823-36.
53. Mori S, Wakana S, Nagae-Poetscher LM, Zijl PCv. *MRI atlas of human white matter.* Amsterdam, The Netherlands: Elsevier; 2005.
54. Fieremans E, Jensen JH, Helpern JA. White matter characterization with diffusional kurtosis imaging. *Neuroimage.* 2011;58:177-88.
55. Benitez A, Fieremans E, Jensen JH, et al. White matter tract integrity metrics reflect the vulnerability of late-myelinating tracts in Alzheimer's disease. *Neuroimage Clin.* 2013;9:64-71.
56. Fieremans E, Benitez A, Jensen JH, et al. Novel white matter tract integrity metrics sensitive to Alzheimer disease progression. *Am. J. Neuroradiol.* 2013;34(2105-12).

57. Fieremans E, Jensen JH, Helpern JA, et al. Diffusion distinguishes between axonal loss and demyelination in brain white matter. *Proc. Intl. Soc. Magn. Reson. Med.* 2012;20 (Melbourne, Australia).
58. Lazar M, Miles LM, Babb JS, Donaldson JB. Axonal deficits in young adults with high functioning autism and their impact on processing speed. *Neuroimage Clin.* 2014;4:417-25.
59. Hui ES, Fieremans E, Jensen JH, et al. Stroke assessment with diffusional kurtosis imaging. Stroke. *Stroke.* 2012(43):2968-73.
60. Grossman EJ, Kirov II, Gonen O, et al. N-acetyl-aspartate levels correlate with intra-axonal compartment parameters from diffusion MRI. *Neuroimage.* 2015;118:334-43.
61. Falangola MF, Guilfoyle DN, Tabesh A, et al. Histological correlation of diffusional kurtosis and white matter modeling metrics in cuprizone-induced corpus callosum demyelination. *NMR biomed.* 2014;27(948-57).
62. Jelescu IO, Zurek M, Winters KV, et al. In vivo quantification of demyelination and recovery using compartment-specific diffusion MRI metrics validated by electron microscopy. *Neuroimage.* 2016;[Epub ahead of print].
63. Hui ES, Glenn GR, Helpern JA, Jensen JH. Kurtosis analysis of neural diffusion organization. *Neuroimage.* 2015;106:391-403.
64. Jensen JH, Glenn GR, Helpern JA. Fiber Ball Imaging. *Neuroimage.* 2016;124:824-33.
65. Reese TG, Heid O, Weisskoff RM, Wedeen VJ. Reduction of eddy-current-induced distortion in diffusion MRI using a twice-refocused spin echo. *Magn. Reson. Med.* 2003;49:177-82.
66. Leemans A, Jones DK. The B-matrix must be rotated when correcting for subject motion in DTI data. *Magn. Reson. Med.* 2009;61:1336-49.
67. Wedeen VJ, Wang RP, Schmahmann JD, et al. Diffusion spectrum magnetic resonance imaging (DSI) tractography of crossing fibers. *Neuroimage.* 2008;41:1267-77.
68. Descoteaux M, Angelino E, Fitzgibbons S, Deriche R. Regularized, fast, and robust analytical Q-ball imaging. Magn Reson Med. *Magn. Reson. Med.* 2007;58:497-510.
69. Hess CP, Mukherjee P, Han ET, Xu D, Vigneron DB. Q-ball reconstruction of multimodal fiber orientations using the spherical harmonic basis. *Magn. Reson. Med.* 2006;56:104-17.
70. Kuo LW, Chen JH, Wedeen VJ, Tseng WY. Optimization of diffusion spectrum imaging and q-ball imaging on clinical MRI system. *Neuroimage.* 2008;41:7-18.
71. Henriques RN, Correi MM, Nunes RG, Ferreira HA. Exploring the 3D geometry of the diffusion kurtosis tensor-Impact on the development of robust tractography procedures and novel biomarkers. *Neuroimage.* 2015;111:85-99.
72. Wu EX, Cheung MM. MR diffusion kurtosis imaging for neural tissue characterization. *NMR Biomed.* 20110;23:836-48.
73. Basser PJ, Mattiello J, Bihan DL. Estimation of the effective self-diffusion tensor from the NMR spin echo. *J. Magn. Reson. B.* 1994;103:247-54.
74. Basser PJ, Pajevic S, Pierpaoli C, Duda J, Aldroubi A. In vivo fiber tractography using DT-MRI data. *Magn. Reson. Med.* 2000;44:625-32.
75. Steven AJ, Zhuo J, RMelhem E. Diffusion kurtosis imaging: an emerging technique for evaluating the microstructural environment of the brain. *AJR Am. J. Roentgenol.* 2014;2002:34-42.
76. Falangola MF, Jensen JH, Babb JS, et al. Age-related non-Gaussian diffusion patterns in the prefrontal brain. *J. Magn. Reson. Imaging.* 2008;28:1345-50.

77. Jeurissen B, Leemans A, Tournier JD, Jones DK, Sijbers J. Investigating the prevalence of complex fiber configurations in white matter tissue with diffusion magnetic resonance imaging. *Hum. Brain Mapp.* 2013;34:2747-66.
78. Mori S, Crain BJ, Chacko VP, Zijl PCv. Three-dimensional tracking of axonal projections in the brain by magnetic resonance imaging. *Ann. Neurol.* 1999;45:265-9.
79. Glenn GR, Helpern JA, Tabesh A, Jensen JH. Quantitative assessment of diffusional kurtosis anisotropy. *NMR Biomed.* 2015;28:448-59.
80. Calamante F, Tournier JD, Jackson GD, Connelly A. Track-density imaging (TDI): super-resolution white matter imaging using whole-brain track-density mapping. *Neuroimage.* 2010;53:1233-43.
81. Jones DK, Knosche TR, Turner R. White matter integrity, fiber count, and other fallacies: The do's and don'ts of diffusion MRI. *Neuroimage.* 2013;73(239-54).
82. Tournier JD, Calamante F, Gadian DG, Connelly A. Direct estimation of the fiber orientation density function from diffusion-weighted MRI data using spherical deconvolution. *Neuroimage.* 2004;23:1176-85.
83. Tournier JD, Calamante F, Connelly A. Robust determination of the fibre orientation distribution in diffusion MRI: non-negativity constrained super-resolved spherical deconvolution. *Neuroimage.* 2007;35:1459-72.
84. Tournier JD, Yeh CH, Calamante F, Cho KH, Connelly A, Lin CP. Resolving crossing fibres using constrained spherical deconvolution: validation using diffusion-weighted imaging phantom data. *Neuroimage.* 2008;15:2747-66.
85. Wilkins B, Namgyun L, Niharika G, Law M, Leporé N. Fiber estimation and tractography in diffusion MRI: development of simulated brain images and comparison of multi-fiber analysis methods at clinical b-values. *Neuroimage.* 2015;109:341-56.
86. Yeh FC, Wedeen VJ, Tseng WY. Estimation of fiber orientation and spin density distribution by diffusion deconvolution. *Neuroimage.* 2011;55:1054-62.
87. Veraart J, Poot DH, Hecke WV, et al. More accurate estimation of diffusion tensor parameters using diffusion Kurtosis imaging. *Magn. Reson. Med.* 2011;65:138-45.
88. Jones DK, Horsfield MA, Simmons A. Optimal strategies for measuring diffusion in anisotropic systems by magnetic resonance imaging. *Magn. Reson. Med.* 1999;42:515-25.
89. Mormina E, Longo M, Arrigo A, et al. MRI Tractography of Corticospinal Tract and Arcuate Fasciculus in High-Grade Gliomas Performed by Constrained Spherical Deconvolution: Qualitative and Quantitative Analysis. *AJNR Am. J. Neuroradiol.* 2015;23:821-35.
90. Romano A, D'Andrea G, Minniti G, et al. Pre-surgical planning and MR-tractography utility in brain tumour resection. *Eur. Radiol.* 2009;19:2798-808.
91. Farquharson S, Tournier JD, Calamante F, et al. White matter fiber tractography: why we need to move beyond DTI. *Neurosurg.* 2013;118:1367-77.
92. Tournier JD, Mori S, Leemans A. Diffusion tensor imaging and beyond. *Magn. Reson. Med.* 2011;65:1532-56.
93. Hagmann P, Jonasson L, Maeder P, Thiran JP, Wedeen VJ, Meuli R. Understanding diffusion MR imaging techniques: from scalar diffusion-weighted imaging to diffusion tensor imaging and beyond. *Radiographics.* 2006;26:S205-23.
94. Fung SH, Roccatagliata L, Gonzalez RG, Schaefer PW. MR diffusion imaging in ischemic stroke. *Neuroimagign Clin. N. Am.* 2011;21:345-77.

95. Grinberg F, Ciobanu L, Farrher E, Shah NJ. Diffusion kurtosis imaging and log-normal distribution function imaging enhance the visualisation of lesions in animal stroke models. *NMR Biomed.* 2012;25:1295-304.
96. Jensen JH, Falangola MF, Hu C, et al. Preliminary observations of increased diffusional kurtosis in human brain following recent cerebral infarction. *NMR Biomed.* 2011;24:452-7.
97. Rudrapatna SU, Wieloch T, Beirup K, et al. Can diffusion kurtosis imaging improve the sensitivity and specificity of detecting microstructural alterations in brain tissue chronically after experimental stroke? Comparisons with diffusion tensor imaging and histology. *Neuroimage.* 2014;97(363-73).
98. Falangola MF, Tabesh JHJA, Hu C, et al. Non-Gaussian diffusion MRI assessment of brain microstructure in mild cognitive impairment and Alzheimer's disease. *Magn. Reson. Imaging.* 2013;31:840-6.
99. Gong NJ, Chan CSWCC, Leung LM, Chu YC. Correlations between microstructural alterations and severity of cognitive deficiency in Alzheimer's disease and mild cognitive impairment: a diffusional kurtosis imaging study. *Magn. Reson. Imaging.* 2013;31:688-94.
100. Vanhoutte G, Pereson S, Delgado Y, et al. Diffusion kurtosis imaging to detect amyloidosis in an APP/PS1 mouse model for Alzheimer's disease. *Magn. Reson. Med.* 2013;69:1115-21.
101. Cauter SV, Veraart J, J Sijbers, et al. Gliomas: diffusion kurtosis MR imaging in grading. *Radiology.* 2012;263:492-501.
102. Raab P, Hattingen E, Franz K, Zanella FE, Lanfermann H. Cerebral gliomas: diffusional kurtosis imaging analysis of microstructural differences. *Radiology.* 2010;254:876-81.
103. Rosenkrantz AB, Sigmund EE, Johnson G, et al. Prostate cancer: feasibility and preliminary experience of a diffusional kurtosis model for detection and assessment of aggressiveness of peripheral zone cancer. *Radiology.* 2012;264:126-35.
104. Glenn GR, Helpern JA, Tabesh A, Jensen JH. Optimization of white matter fiber tractography with diffusional kurtosis imaging. *NMR Biomed.* 2015;28:1245-56.
105. Griswold MA, Jakob PM, Heidemann RM, et al. Generalized autocalibrating partially parallel acquisitions (GRAPPA). *Magn. Reson. Med.* 2002;47:1202-10.
106. Walsh DO, Gmitro AF, Marcellin MW. Adaptive reconstruction of phased array MR imagery. *Magn. Reson. Med.* 2000;43:682-90.
107. Yeh FC, Verstynen TD, Wang Y, Fernández-Miranda JC, Tseng WY. Deterministic diffusion fiber tracking improved by quantitative anisotropy. *PLoS One.* 2013;8:e80713.
108. Glenn GR, Kuo LW, Chao YP, Lee CY, Helpern JA, Jensen JH. Mapping the orientation of white matter fiber bundles: A comparative study of diffusion tensor imaging, diffusional kurtosis imaging, and diffusion spectrum imaging. *AJNR Am. J. Neuroradiol.* 2016:[Epub ahead of print].
109. Caverzasi E, Hervey-Jumper SL, Jordan KM, et al. Identifying preoperative language tracts and predicting postoperative functional recovery using HARDI q-ball fiber tractography in patients with gliomas. *J. Neurosurg.* 2015:[Epub ahead of print].
110. Tefera GB, Zhou Y, Juneja V, Narayana PA. Evaluation of fiber tracking from subsampled q-space data in diffusion spectrum imaging. *Magn. Reson. Imaging.* 2013;31:820-6.

111. Kuo LW, Chiang WY, Yeh FC, Wedeen VJ, Tseng WY. Diffusion spectrum MRI using body-centered-cubic and half-sphere sampling schemes. *J. Neurosci. Methods.* 2013;212:143-55.
112. Yeh CH, Cho KH, Lin HC, Wang JJ, Lin CP. Reduced encoding diffusion spectrum imaging implemented with a bi-Gaussian model. *IEEE Trans. Med. Imaging.* 2008;27:1415-24.
113. Menzel MI, Tan ET, Khare K, et al. Accelerated diffusion spectrum imaging in the human brain using compressed sensing. *Magn. Reson. Med.* 2011;66:1226-33.
114. Feinberg DA, Setsompop K. Ultra-fast MRI of the human brain with simultaneous multi-slice imaging. *J. Magn. Reson.* 2013;229:90-100.
115. Larkman DJ, Hajnal JV, Herlihy AH, Coutts GA, Young IR, Ehnholm G. Use of multicoil arrays for separation of signal from multiple slices simultaneously excited. *J. Magn. Reson. Imaging.* 2001;13:313-17.
116. Reese TG, Benner T, Wang R, Feinberg DA, Wedeen VJ. Halving imaging time of whole brain diffusion spectrum imaging and diffusion tractography using simultaneous image refocusing in EPI. *J. Magn. Reson. Imaging.* 2009;29:517-22.
117. Setsompop K, Cohen-Adad J, Gagoski BA, et al. Improving diffusion MRI using simultaneous multi-slice echo planar imaging. *Neuroimage.* 2012;63:569-80.
118. Setsompop K, Kimmlingen R, Eberlein E, et al. Pushing the limits of in vivo diffusion MRI for the Human Connectome Project. *Neuroimage.* 2013;80:220-33.
119. Kiselev VG. The cumulant expansion: an overarching mathematical framework for understanding diffusion NMR. In: Jones DK, ed. *Diffusion MRI: Theory, Methods and Applications*. Oxford: Oxford University Press; 2011:152– 68.
120. Perrone D, Aelterman J, Pižurica A, Jeurissen B, Philips W, Leemans A. The effect of Gibbs ringing artifacts on measures derived from diffusion MRI. *Neuroimage.* 2015;120:441-55.
121. Veraart J, Fieremans E, Jelescu IO, Knoll F, Novikov DS. Gibbs ringing in diffusion MRI. *Magn. Reson. Med.* 2015:[Epub ahead of print].
122. Glenn GR, Tabesh A, Jensen JH. A simple noise correction scheme for diffusional kurtosis imaging. *Magn. Reson. Imaging.* 2015;33:124-33.
123. Ngugi AK, Bottomley C, Kleinschmidt I, Sander JW, Newton CR. Estimation of the burden of active and life-time epilepsy: a meta-analytic approach. *Epilepsia.* 2010;51(5):883-90.
124. Neligan A, Hauser WA, Sander JW. The epidemiology of the epilepsies. *Handbook of clinical neurology.* 2012;107:113-33.
125. Sander JW, Shorvon SD. Epidemiology of the epilepsies. *Journal of neurology, neurosurgery, and psychiatry.* 1996;61(5):433-43.
126. Engel J, Jr. Mesial temporal lobe epilepsy: what have we learned? *The Neuroscientist : a review journal bringing neurobiology, neurology and psychiatry.* 2001;7(4):340-52.
127. Semah F, Picot MC, Adam C, et al. Is the underlying cause of epilepsy a major prognostic factor for recurrence? *Neurology.* 1998;51(5):1256-62.
128. Wiebe S, Blume WT, Girvin JP, Eliasziw M, Effectiveness, Efficiency of Surgery for Temporal Lobe Epilepsy Study G. A randomized, controlled trial of surgery for temporal-lobe epilepsy. *The New England journal of medicine.* 2001;345(5):311-8.
129. de Tisi J, Bell GS, Peacock JL, et al. The long-term outcome of adult epilepsy surgery, patterns of seizure remission, and relapse: a cohort study. *Lancet.* 2011;378(9800):1388-95.

130. McIntosh AM, Kalnins RM, Mitchell LA, Fabinyi GC, Briellmann RS, Berkovic SF. Temporal lobectomy: long-term seizure outcome, late recurrence and risks for seizure recurrence. *Brain.* 2004;127(Pt 9):2018-30.
131. Berkovic SF, McIntosh AM, Kalnins RM, et al. Preoperative MRI predicts outcome of temporal lobectomy: an actuarial analysis. *Neurology.* 1995;45(7):1358-63.
132. Giulioni M, Marucci G, Martinoni M, et al. Seizure outcome in surgically treated drug-resistant mesial temporal lobe epilepsy based on the recent histopathological classifications. *Journal of neurosurgery.* 2013;119(1):37-47.
133. Hemb M, Palmini A, Paglioli E, et al. An 18-year follow-up of seizure outcome after surgery for temporal lobe epilepsy and hippocampal sclerosis. *Journal of neurology, neurosurgery, and psychiatry.* 2013;84(7):800-5.
134. Janszky J, Janszky I, Schulz R, et al. Temporal lobe epilepsy with hippocampal sclerosis: predictors for long-term surgical outcome. *Brain.* 2005;128(Pt 2):395-404.
135. Bonilha L, Kobayashi E, Mattos JP, Honorato DC, Li LM, Cendes F. Value of extent of hippocampal resection in the surgical treatment of temporal lobe epilepsy. *Arquivos de neuro-psiquiatria.* 2004;62(1):15-20.
136. Bonilha L, Keller SS. Quantitative MRI in refractory temporal lobe epilepsy: relationship with surgical outcomes. *Quantitative imaging in medicine and surgery.* 2015;5(2):204-24.
137. Keller SS, Cresswell P, Denby C, et al. Persistent seizures following left temporal lobe surgery are associated with posterior and bilateral structural and functional brain abnormalities. *Epilepsy Res.* 2007;74(2-3):131-9.
138. Prasad A, Pacia SV, Vazquez B, Doyle WK, Devinsky O. Extent of ictal origin in mesial temporal sclerosis patients monitored with subdural intracranial electrodes predicts outcome. *Journal of clinical neurophysiology : official publication of the American Electroencephalographic Society.* 2003;20(4):243-8.
139. Holmes MD, Born DE, Kutsy RL, Wilensky AJ, Ojemann GA, Ojemann LM. Outcome after surgery in patients with refractory temporal lobe epilepsy and normal MRI. *Seizure : the journal of the British Epilepsy Association.* 2000;9(6):407-11.
140. Babb TL, Brown WJ, Pretorius J, Davenport C, Lieb JP, Crandall PH. Temporal lobe volumetric cell densities in temporal lobe epilepsy. *Epilepsia.* 1984;25(6):729-40.
141. Lin JJ, Salamon N, Dutton RA, et al. Three-dimensional preoperative maps of hippocampal atrophy predict surgical outcomes in temporal lobe epilepsy. *Neurology.* 2005;65(7):1094-7.
142. Hennessy MJ, Elwes RD, Binnie CD, Polkey CE. Failed surgery for epilepsy. A study of persistence and recurrence of seizures following temporal resection. *Brain.* 2000;123 Pt 12:2445-66.
143. Ryvlin P, Kahane P. The hidden causes of surgery-resistant temporal lobe epilepsy: extratemporal or temporal plus? *Current opinion in neurology.* 2005;18(2):125-7.
144. Kahane P, Barba C, Rheims S, Job-Chapron AS, Minotti L, Ryvlin P. The concept of temporal 'plus' epilepsy. *Revue neurologique.* 2015;171(3):267-72.
145. Sisodiya SM, Moran N, Free SL, et al. Correlation of widespread preoperative magnetic resonance imaging changes with unsuccessful surgery for hippocampal sclerosis. *Ann Neurol.* 1997;41(4):490-6.
146. Barba C, Rheims S, Minotti L, et al. Temporal plus epilepsy is a major determinant of temporal lobe surgery failures. *Brain.* 2015.

147. Keller SS, Richardson MP, O'Muircheartaigh J, Schoene-Bake JC, Elger C, Weber B. Morphometric MRI alterations and postoperative seizure control in refractory temporal lobe epilepsy. *Human brain mapping.* 2015;36(5):1637-47.
148. Keller SS, Richardson MP, Schoene-Bake JC, et al. Thalamotemporal alteration and postoperative seizures in temporal lobe epilepsy. *Ann Neurol.* 2015;77(5):760-74.
149. Bonilha L, Martz GU, Glazier SS, Edwards JC. Subtypes of medial temporal lobe epilepsy: influence on temporal lobectomy outcomes? *Epilepsia.* 2012;53(1):1-6.
150. Blumcke I, Pauli E, Clusmann H, et al. A new clinico-pathological classification system for mesial temporal sclerosis. *Acta Neuropathol.* 2007;113(3):235-44.
151. Thom M, Liagkouras I, Elliot KJ, et al. Reliability of patterns of hippocampal sclerosis as predictors of postsurgical outcome. *Epilepsia.* 2010;51(9):1801-8.
152. Bernhardt BC, Bonilha L, Gross DW. Network analysis for a network disorder: The emerging role of graph theory in the study of epilepsy. *Epilepsy & behavior : E&B.* 2015;50:162-70.
153. Richardson MP. Large scale brain models of epilepsy: dynamics meets connectomics. *Journal of neurology, neurosurgery, and psychiatry.* 2012;83(12):1238-48.
154. Bernhardt BC, Hong S, Bernasconi A, Bernasconi N. Imaging structural and functional brain networks in temporal lobe epilepsy. *Frontiers in human neuroscience.* 2013;7:624.
155. Bonilha L, Jensen JH, Baker N, et al. The brain connectome as a personalized biomarker of seizure outcomes after temporal lobectomy. *Neurology.* 2015;84(18):1846-53.
156. Bonilha L, Helpern JA, Sainju R, et al. Presurgical connectome and postsurgical seizure control in temporal lobe epilepsy. *Neurology.* 2013;81(19):1704-10.
157. Munsell BC, Wee CY, Keller SS, et al. Evaluation of machine learning algorithms for treatment outcome prediction in patients with epilepsy based on structural connectome data. *Neuroimage.* 2015;118:219-30.
158. Yeatman JD, Dougherty RF, Myall NJ, Wandell BA, Feldman HM. Tract profiles of white matter properties: automating fiber-tract quantification. *PLoS One.* 2012;7(11):e49790.
159. Johnson RT, Yeatman JD, Wandell BA, Buonocore MH, Amaral DG, Nordahl CW. Diffusion properties of major white matter tracts in young, typically developing children. *Neuroimage.* 2013;88C:143-54.
160. Concha L, Livy DJ, Beaulieu C, Wheatley BM, Gross DW. In vivo diffusion tensor imaging and histopathology of the fimbria-fornix in temporal lobe epilepsy. *J Neurosci.* 2010;30(3):996-1002.
161. Concha L, Beaulieu C, Gross DW. Bilateral limbic diffusion abnormalities in unilateral temporal lobe epilepsy. *Ann Neurol.* 2005;57(2):188-96.
162. Concha L, Beaulieu C, Collins DL, Gross DW. White-matter diffusion abnormalities in temporal-lobe epilepsy with and without mesial temporal sclerosis. *Journal of neurology, neurosurgery, and psychiatry.* 2009;80(3):312-9.
163. McDonald CR, Ahmadi ME, Hagler DJ, et al. Diffusion tensor imaging correlates of memory and language impairments in temporal lobe epilepsy. *Neurology.* 2008;71(23):1869-76.
164. Keller SS, Schoene-Bake JC, Gerdes JS, Weber B, Deppe M. Concomitant fractional anisotropy and volumetric abnormalities in temporal lobe epilepsy: cross-sectional evidence for progressive neurologic injury. *PLoS One.* 2012;7(10):e46791.

165. Ahmadi ME, Hagler DJ, Jr., McDonald CR, et al. Side matters: diffusion tensor imaging tractography in left and right temporal lobe epilepsy. *AJNR. American journal of neuroradiology.* 2009;30(9):1740-7.
166. Yogarajah M, Powell HW, Parker GJ, et al. Tractography of the parahippocampal gyrus and material specific memory impairment in unilateral temporal lobe epilepsy. *Neuroimage.* 2008;40(4):1755-64.
167. Diehl B, Busch RM, Duncan JS, Piao Z, Tkach J, Luders HO. Abnormalities in diffusion tensor imaging of the uncinate fasciculus relate to reduced memory in temporal lobe epilepsy. *Epilepsia.* 2008;49(8):1409-18.
168. Lin JJ, Riley JD, Juranek J, Cramer SC. Vulnerability of the frontal-temporal connections in temporal lobe epilepsy. *Epilepsy Res.* 2008;82(2-3):162-70.
169. Salanova V, Andermann F, Rasmussen T, Olivier A, Quesney L. The running down phenomenon in temporal lobe epilepsy. *Brain.* 1996;119 (Pt 3):989-96.
170. Joo EY, Han HJ, Lee EK, et al. Resection extent versus postoperative outcomes of seizure and memory in mesial temporal lobe epilepsy. *Seizure : the journal of the British Epilepsy Association.* 2005;14(8):541-51.
171. Hardy SG, Miller JW, Holmes MD, et al. Factors predicting outcome of surgery for intractable epilepsy with pathologically verified mesial temporal sclerosis. *Epilepsia.* 2003;44(4):565-8.
172. Kanner AM, Kaydanova Y, deToledo-Morrell L, et al. Tailored anterior temporal lobectomy. Relation between extent of resection of mesial structures and postsurgical seizure outcome. *Archives of neurology.* 1995;52(2):173-8.
173. Jack CR, Jr., Sharbrough FW, Marsh WR. Use of MR imaging for quantitative evaluation of resection for temporal lobe epilepsy. *Radiology.* 1988;169(2):463-8.
174. Kral T, Clusmann H, Urbach J, et al. Preoperative evaluation for epilepsy surgery (Bonn Algorithm). *Zentralblatt fur Neurochirurgie.* 2002;63(3):106-10.
175. Bien CG, Raabe AL, Schramm J, Becker A, Urbach H, Elger CE. Trends in presurgical evaluation and surgical treatment of epilepsy at one centre from 1988-2009. *Journal of neurology, neurosurgery, and psychiatry.* 2013;84(1):54-61.
176. Elkommos S, Weber B, Niehusmann P, et al. Hippocampal internal architecture and postoperative seizure outcome in temporal lobe epilepsy due to hippocampal sclerosis. *Seizure : the journal of the British Epilepsy Association.* 2016;In press.
177. Wieser HG, Blume WT, Fish D, et al. ILAE Commission Report. Proposal for a new classification of outcome with respect to epileptic seizures following epilepsy surgery. *Epilepsia.* 2001;42(2):282-6.
178. Smith SM. Fast robust automated brain extraction. *Human brain mapping.* 2002;17(3):143-55.
179. Basser PJ, Pajevic S, Pierpaoli C, Duda J, Aldroubi A. In vivo fiber tractography using DT-MRI data. *Magn Reson Med.* 2000;44(4):625-32.
180. Benjamini Y, Hochberg Y. Controlling the false discovery rate: a practical and powerful approach to multiple testing. *J R Stat Soc Series B.* 1995;57:289-300.
181. Rorden C, Bonilha L, Fridriksson J, Bender B, Karnath HO. Age-specific CT and MRI templates for spatial normalization. *Neuroimage.* 2012;61(4):957-65.
182. Nachev P, Coulthard E, Jager HR, Kennard C, Husain M. Enantiomorphic normalization of focally lesioned brains. *Neuroimage.* 2008;39(3):1215-26.

183. van Eijsden P, Otte WM, van der Hel WS, et al. In vivo diffusion tensor imaging and ex vivo histologic characterization of white matter pathology in a post-status epilepticus model of temporal lobe epilepsy. *Epilepsia.* 2011;52(4):841-5.
184. Buzsaki G, Ponomareff GL, Bayardo F, Ruiz R, Gage FH. Neuronal activity in the subcortically denervated hippocampus: a chronic model for epilepsy. *Neuroscience.* 1989;28(3):527-38.
185. Lahtinen H, Miettinen R, Ylinen A, Halonen T, Riekkinen PJ, Sr. Biochemical and morphological changes in the rat hippocampus following transection of the fimbria-fornix. *Brain research bulletin.* 1993;31(3-4):311-8.
186. Lahtinen H, Korhonen E, Castren E, Miettinen R, Ylinen A, Riekkinen PJ, Sr. Long-term alterations in NMDA-sensitive L-[3H]glutamate binding in the rat hippocampus following fimbria-fornix lesioning. *Experimental neurology.* 1993;121(2):193-9.
187. Aggleton JP, Desimone R, Mishkin M. The origin, course, and termination of the hippocampothalamic projections in the macaque. *The Journal of comparative neurology.* 1986;243(3):409-21.
188. Kehoe EG, Farrell D, Metzler-Baddeley C, et al. Fornix White Matter is Correlated with Resting-State Functional Connectivity of the Thalamus and Hippocampus in Healthy Aging but Not in Mild Cognitive Impairment - A Preliminary Study. *Frontiers in aging neuroscience.* 2015;7:10.
189. Wennberg R, Arruda F, Quesney LF, Olivier A. Preeminence of extrahippocampal structures in the generation of mesial temporal seizures: evidence from human depth electrode recordings. *Epilepsia.* 2002;43(7):716-26.
190. Benini R, Longo D, Biagini G, Avoli M. Perirhinal cortex hyperexcitability in pilocarpine-treated epileptic rats. *Hippocampus.* 2011;21(7):702-13.
191. Bartolomei F, Khalil M, Wendling F, et al. Entorhinal cortex involvement in human mesial temporal lobe epilepsy: an electrophysiologic and volumetric study. *Epilepsia.* 2005;46(5):677-87.
192. Bernasconi N, Bernasconi A, Caramanos Z, Andermann F, Dubeau F, Arnold DL. Morphometric MRI analysis of the parahippocampal region in temporal lobe epilepsy. *Annals of the New York Academy of Sciences.* 2000;911:495-500.
193. Concha L, Kim H, Bernasconi A, Bernhardt BC, Bernasconi N. Spatial patterns of water diffusion along white matter tracts in temporal lobe epilepsy. *Neurology.* 2012;79(5):455-62.
194. Lieb JP, Dasheiff RM, Engel J, Jr. Role of the frontal lobes in the propagation of mesial temporal lobe seizures. *Epilepsia.* 1991;32(6):822-37.
195. Mayanagi Y, Watanabe E, Kaneko Y. Mesial temporal lobe epilepsy: clinical features and seizure mechanism. *Epilepsia.* 1996;37 Suppl 3:57-60.
196. Chassoux F, Semah F, Bouilleret V, et al. Metabolic changes and electro-clinical patterns in mesio-temporal lobe epilepsy: a correlative study. *Brain.* 2004;127(Pt 1):164-74.
197. Engel J, Jr., Henry TR, Risinger MW, et al. Presurgical evaluation for partial epilepsy: relative contributions of chronic depth-electrode recordings versus FDG-PET and scalp-sphenoidal ictal EEG. *Neurology.* 1990;40(11):1670-7.
198. Henry TR, Mazziotta JC, Engel J, Jr. Interictal metabolic anatomy of mesial temporal lobe epilepsy. *Archives of neurology.* 1993;50(6):582-9.
199. Chabardes S, Kahane P, Minotti L, et al. The temporopolar cortex plays a pivotal role in temporal lobe seizures. *Brain.* 2005;128(Pt 8):1818-31.

200. Schramm J. Temporal lobe epilepsy surgery and the quest for optimal extent of resection: a review. *Epilepsia.* 2008;49(8):1296-307.
201. Ji GJ, Zhang Z, Xu Q, et al. Connectome Reorganization Associated With Surgical Outcome in Temporal Lobe Epilepsy. *Medicine.* 2015;94(40):e1737.
202. Burneo JG, Black L, Martin R, et al. Race/ethnicity, sex, and socioeconomic status as predictors of outcome after surgery for temporal lobe epilepsy. *Archives of neurology.* 2006;63(8):1106-10.
203. Aull-Watschinger S, Pataraia E, Czech T, Baumgartner C. Outcome predictors for surgical treatment of temporal lobe epilepsy with hippocampal sclerosis. *Epilepsia.* 2008;49(8):1308-16.
204. Babb TL, Brown WJ. Pathological findings in epilepsy. In: Engel JJ, ed. *Surgical Treatment of the Epilepsies*. New York: Raven; 1987.
205. Haneef Z, Lenartowicz A, Yeh HJ, Levin HS, Engel JJ, JM JMS. Functional connectivity of hippocampal networks in temporal lobe epilepsy. *Epilepsia.* 2014;55:137-45.
206. Gross DW, Concha L, Beaulieu C. Extratemporal white matter abnormalities in mesial temporal lobe epilepsy demonstrated with diffusion tensor imaging. *Epilepsia.* 2006;47:1360-3.
207. Kelle SS, Roberts N. Extratemporal white matter abnormalities in mesial temporal lobe epilepsy demonstrated with diffusion tensor imaging. *Epilepsia.* 2008;49:741-57.
208. Bonilha L, Kobayashi E, Rorden C, Cendes F, Li M. Medial temporal lobe atrophy in patients with refractory temporal lobe epilepsy. *J. Neurol. Neurosurg. Psychiatry* 2003;74:1627-30.
209. Coan AC, Appenzeller S, Bonilha L, Li M, Cendes F. Seizure frequency and lateralization affect progression of atrophy in temporal lobe epilepsy. *Neurology.* 2009;73:834-42.
210. McMillan AB, Hermann BP, Johnson SC, Hansen RR, Seidenberg M, Meyerand ME. Voxel-based morphometry of unilateral temporal lobe epilepsy reveals abnormalities in cerebral white matter. *Neuroimage.* 2004;23:167-74.
211. Bonilha L, Edwards JC, Kinsman SL, et al. Extrahippocampal gray matter loss and hippocampal deafferentation in patients with temporal lobe epilepsy. *Epilepsia.* 2010;51:519-28.
212. Bonilha L, Elm JJ, Edwards JC, et al. How common is brain atrophy in patients with medial temporal lobe epilepsy? *Epilepsia.* 2010;51:1774-9.
213. Bonilha L, Lee CY, Jensen JH, et al. Altered microstructure in temporal lobe epilepsy: a diffusional kurtosis imaging study. *AJNR. American journal of neuroradiology.* 2015;36:719-24.
214. Gao J, Feng ST, Wu B, et al. Microstructural brain abnormalities of children of idiopathic generalized epilepsy with generalized tonic-clonic seizure: a voxel-based diffusional kurtosis imaging study. *J. Magn. Reson. Imaging.* 2015;41:1088-95.
215. Gao Y, Zhang Y, Wong CS, et al. Diffusion abnormalities in temporal lobes of children with temporal lobe epilepsy: a preliminary diffusional kurtosis imaging study and comparison with diffusion tensor imaging. *NMR Biomed.* 2012;25:1369-77.
216. Lee CY, Tabesh A, Benitez A, Helpern JA, Jensen JH, Bonilha L. Microstructural integrity of early- versus late-myelinating white matter tracts in medial temporal lobe epilepsy. *Epilepsia.* 2013;54:1801-9.

217. Blümcke I, Thom M, Aronica E, et al. International consensus classification of hippocampal sclerosis in temporal lobe epilepsy: a Task Force report from the ILAE Commission on Diagnostic Methods. *Epilepsia.* 2013;54:1315-29.
218. Bonilha L, Yasuda CL, Rorden C, et al. Does resection of the medial temporal lobe improve the outcome of temporal lobe epilepsy surgery? . *Epilepsia.* 2007;48:571-8.
219. Bilevicius E, Yasuda CL, Silva MS, Guerreiro CA, Lopes-Cendes I, Cendes F. Antiepileptic drug response in temporal lobe epilepsy: a clinical and MRI morphometry study. *Neurology.* 2010;75:1695-701.
220. Keller SS, Mackay CE, Barrick TR, Wieshmann UC, Howard MA, Roberts N. Voxel-based morphometric comparison of hippocampal and extrahippocampal abnormalities in patients with left and right hippocampal atrophy. *Neuroimage.* 2002;16:23-31.

APPENDIX: PEER-REVIEWED PUBLICATIONS

Related to the Thesis

1. Keller SS[§], **Glenn GR**[§], Weber B, Kreilkamp B, Jensen JH, Helpern JA, Wagner J, Barker GJ, Richardson MP, Bonilha L. Preoperative automated fibre quantification predicts postoperative seizure outcome in temporal lobe epilepsy. Brain. [Under Review].
2. **Glenn GR**, Jensen JH, Helpern JA, Spampinato MV, Kuzniecky R, Keller SS, Bonilha L. Epilepsy-related cytoarchitectonic abnormalities along white matter pathways. J. Neurol. Neurosurg. Psychiatry. [Epub ahead of print].
3. **Glenn GR**, Kuo LW, Chao YP, Lee CY, Helpern JA, Jensen JH. Comparison of diffusion orientation distribution functions obtained with diffusion spectrum imaging, diffusional kurtosis imaging, and diffusion tensor imaging for *in vivo* estimation of white matter fiber bundle orientations. AJNR Am J Neuroradiol. [Epub ahead of print].
4. Jensen JH**, Glenn GR**, Helpern JA. Fiber ball imaging. Neruoimage. 2016;124:824-833.
5. **Glenn GR**, Helpern JA, Tabesh A, Jensen JH. Optimization of white matter fiber tractography with diffusional kurtosis imaging. NMR Biomed. 2015;28:1245-56.
6. **Glenn GR**, Helpern JA, Tabesh A, Jensen JH. Quantitative assessment of diffusional kurtosis anisotropy. NMR Biomed. 2015. 28:448-59.
7. Hui ES, **Glenn GR**, Helpern JA, Jensen JH. Kurtosis analysis of neural diffusion organization. Neuroimage. 2015. 106:391-403.

[§] shared first authorship

Unrelated to the Thesis

1. McKinnon E, Jensen JH, **Glenn GR**, Helpern JA. Dependence on b-value of the direction-averaged diffusion weighted image signal in brain. Magn Reson Imaging. [Under Review].
2. Jensen JH, McKinnon E, **Glenn GR**, Helpern JA. Evaluating Kurtosis-based Diffusion MRI Tissue Models for White Matter with Fiber Ball Imaging. NMR in Biomed. [Under Review].
3. **Glenn GR,** Tabesh A, Jensen JH. A simple retrospective noise correction scheme for diffusional kurtosis imaging. Magn Reson Imaging. 2015. 33:124-33.
4. Geyer LL, **Glenn GR**, De Cecco CN, Van Horn M, Canstein C, Silverman JR, Krazinski AW, Kemper JM, Bucher A, Ebersberger U, Costello P, Bamberg F, Schoepf UJ**.** CT evaluation of small-diameter coronary artery stents: effect of an ittegrated circuit detector with iterative reconstruction. Radiology. 2015;276:706-14.
5. **Glenn GR**, Zhang Y, Krasin M, Hua C, "PIRATE: pediatric imaging response assessment and targeting environment", Proc. SPIE, vol. 7625, 76251S, 2010.
6. Hua C, Merchant TE, Gajjar A, Broniscer A, Zhang Y, Li Y, **Glenn GR**, Kun LE, Ogg RJ. "Brain tumor therapy-induced changes in normal-appearing brainstem measured with longitudinal diffusion tensor imaging," International Journal of Radiation Oncology* Biology*Physics, 82(5):2047-54, 2012.